Automated Model-Based Optimization Design of Subsea Field Layout under Production and Flow Assurance Constraints

by
Hamdi Mnasri

A thesis submitted to the Department of Mechanical Engineering,
Cullen College of Engineering
in partial fulfillment of the requirements for the degree of

DOCTOR OF PHILOSOPHY

in Mechanical Engineering

Chair of Committee: Matthew A. Franchek

Co-Chair of Committee: Karolos Grigoriadis

Committee Member: Gangbing Song

Committee Member: Marzia Cescon

Committee Member: Rose Faghih

University of Houston
May 2021

ACKNOWLEDGMENTS

My sincere appreciation and gratitude are due to all those who have contributed to the achievement of the presented research and have been a great support during this overwhelming journey.

Foremost, my special gratitude is addressed to my dear supervisor Dr. Matthew A. Franchek, for all the support, guidance, and advice he provided me during the preparation of this PhD study. His priceless contribution with his knowledge and encouragement conveyed a spirit of adventure and innovation during this research. Without his continuous assistance and guidance this work would not be possible.

I also would like to express my deepest appreciation to my committee members, Dr. Karolos Grigoriadis, Dr. Gangbing Song, Dr. Marzia Cescon, and Dr. Rose Faghih, for accepting to evaluate the presented dissertation and for reviewing my research work.

Many thanks are also due to my fellow colleagues at the University of Houston for all their support, discussions, and the fun we have had during this amazing period. A special thanks is presented to those who have assisted me in the achievement of the current research, particularly Dr. Taoufik Wassar, Dr. Amine Meziou and Dr. Yingjie Tang, thank you for all the helpful and productive contributions.

Finally, I would like to express my great gratitude for my parents and my family for all the love, support and sacrifices throughout my life that brought me strength and inspiration to complete this work.

ABSTRACT

Subsea explorations are a major contributor to the global energy balance. A lot of research has been put into action to enhance all aspects of this industry despite the complexity faced. Therefore, developing tools with reduced computational time efforts while maintaining high accuracy levels is a crucial engineering and scientific challenge to maintain such position.

Presented in this dissertation is an autonomous model-based simulation and optimization approach intended to be deployed during the pre-Front-End-Engineering-Design (pre-FEED) study phase of a subsea field development project. The proposed methodology is developed so subsea engineers use it as an asset to perform subsea field architecture design optimization. Based on a multi-objective optimization, experts can identify and select solutions satisfying pre-defined financial and technical targets. Additionally, the presented work is aimed to achieve tasks beyond its pre-FEED study utility. Specifically, deep-dive analysis is enabled to deal with real-time production system properties tracking, health monitoring and integrity assessment via model's self-adaptation routines.

By integration of different reduced-order physics-based models, a digital twin for a subsea production system is created. Hence, low-dimensional models have been developed to describe several aspects of a subsea system. A crucial part of the developed platform is illustrated via a multiphase flow reduced order model. A model developed as a steady-state multiphase mechanistic model in series with a dissipative distributed

single-phase transient model, coupled via estimation of equivalent fluid properties. Additionally, flow assurance and structural integrity are serious issues within the subsea industry. A contribution to the presented matter, a data-driven parameter varying corrosion rate prediction model is presented as an amelioration of the existing prediction packages.

Integrating the developed models along with several other reduced-order models within a hybrid optimization process, optimal layout scheme of a subsea field under production and flow assurance constraints can be determined. A digital twin of a subsea production system has been developed to mimic the operating process of a complete subsea production field starting from a newly discovered reservoir and ending at a terminal, thus, used as a virtual simulation environment of a subsea field overall life cycle within all compartment: upstream, mid-stream and downstream.

TABLE OF CONTENTS

LIST OF TABLES

LIST OF FIGURES

NOMENCLATURE

Variable	Description	Unit
a	Fugacity Coefficient	Pa
A	Pipeline cross-section area	m^2
C	API 14E erosion C-factor	------
c_{eq}	Fluid equivalent speed of sound	m/s
C_0	Base cost	USD/m
C_L	No-slip Liquid holdup	------
C_{corr}	Correction cost	USD
C_{misc}	Coating cost	USD
C_p, $C_{p,k}$, $C^i_{p,M}$	Specific heat capacity, specific heat capacity at node k, specific heat capacity of fluid from well w_i to manifold M	J/kg.C
$COST_{M_i}$	Cost of manifold M_i in ith well set	USD
$COST_{Manifolds}$	Cost of all installed manifolds	USD
$COST_{T,ini}$	Initial design overall cost	USD
$COST_T$	Overall cost	USD
$COST_i$	Cost of all installed pipelines in i^{th} well set	USD
$COST_{manifolds}$	Vector of manifolds costs	USD
$COST_{pipelines}$	Cost of all installed pipelines	USD
CR, CR_{act}, CR_{mass}	Corrosion rate, kinetics activation Corrosion rate, Mass transfer corrosion rate	mm/year
CR_{NOR}	NORSOK Corrosion Rate	mm/year
$CR_{Recalibrated}$	Recalibrated DeWaard, Lotz and Dugstad Corrosion Rate	mm/year
CR_m	DeWaard, Lotz and Dugstad Mass Transfer Corrosion Rate	mm/year
CR_{mes}	Measured Corrosion Rate	mm/year
CR_r	DeWaard, Lotz and Dugstad Activation Kinetics Corrosion Rate	mm/year
CR_R^*	Recalibrated Activation Kinetics Corrosion Rate	mm/year
CR_r^{EXP}	Reference Activation Kinetics Corrosion Rate	mm/year
CR_r^{final}	Final Recalibrated Activation Kinetics Corrosion Rate	mm/year
D, ID, OD	Pipeline diameter, pipeline inner diameter, pipeline outer diameter	m
E	Longitudinal weld-joint factor	------
E_L	Liquid holdup	------
E_{ratio}	Erosional ratio	------
f_0	Basic Cost of a Subsea Manifold	USD
f_1	Tree type cost factor	------
f_2	Pressure rating cost factor	------
f_3	Bore size cost factor	------
f_{CO_2}	Carbon Dioxide Fugacity	bar
f_{eq}	Equivalent Darcy friction factor	------
$f(pH)$	NORSOK pH dependent function	------
f_s	Flowline size cost factor	------
f_t	Flowline type cost factor	------
f_{tp}	Two-phase friction factor	------
F_{scale}	Corrosion scale layer correction factor	------
g	Gravitational acceleration (=9.81)	m/s
g_c	Conversion factor (=1)	$kg.m/N/s^2$

h_{tp}	Two-phase heat transfer coefficient	W/(C.m)
h_0	External convection heat transfer coefficient	W/(C.m)
k	Isentropic exponent (k=1.4)	------
K_t	NORSOK Temperature Constant	------
L	Pipeline length	m
lifespan	Pipeline lifespan	year
$\dot{m}, \dot{m}_k, \dot{m}_M^i$	Fluid mass flow rate, fluid mass flow rate at node k, mass flow rate of fluid from well w_i to manifold M	kg/s
m_i	i^{th} well set size	------
n	Total number of wells	------
n_c	Number of well clusters	------
$Nbr_{manifolds}$	Vector of manifolds number	------
Nbr_{slot}	Vector of manifolds slots number	------
P	Allowable internal pressure	Pa
P_{in}, P_{out}	Inlet, outlet pressure	Pa
P_0	Atmospheric pressure	Pa
P_{avg}	Fluid average pressure	Pa
P_{CO_2}	Carbon Dioxide Partial Pressure	bar
P_k	Pressure at the k^{th} node in the graph for shortest path search	Pa
pH	Fluid pH	------
Q	Fluid volumetric flow rate	m^3/s
Q_L	Liquid phase volumetric flow rate	m^3/s
Q_G	Gas phase volumetric flow rate	m^3/s
Q_{in}, Q_{out}	Inlet, outlet volumetric flow rate	m^3/s
S	Pipeline shear stress	bar
S_p	Allowable internal pipeline stress	Pa
T	Temperature	°C
T_M	Temperature at manifold M	°C
T_{scale}	Corrosion scale layer appearance temperature	°C
$T_{in}, T_{out}, T_{ambient}, T_k$	Input, output, ambient temperature, and temperature at node k in the graph for path search	°C
T_{ol}	Manufacturer allowable percent tolerance	%
t	Pipeline wall thickness	m
t_e	Maximum corrosion allowance	m
t_p	Penetration depth	m
t_{th}	Thread or groove depth	m
U, U_k	Overall heat transfer coefficient, overall heat transfer coefficient at node k	$W/(C.m^2)$
WAT	Wax appearance temperature	°C
V_m	Mean Flow Velocity	m/s
V_{SG}	Gas superficial velocity	m/s
V_{SL}	Liquid superficial velocity	m/s
V_{G_0}	Entrained air average superficial velocity in liquid at atmospheric pressure	m/s
V_{L_0}	Average liquid superficial velocity at atmospheric pressure	m/s
$V_{erosion}$	Erosional velocity	m/s
$V_{mixture}$	Mixture velocity	m/s
$x_c, y_c, u_k, v_k, p_k, q_k, z_k^0$	Fitting parameters	------
$x, y, z, x_{W_i}, y_{W_i}, z_{W_i}$	Space coordinates	m
Y	Derating factor	------
μ_G	Gas viscosity	Pa.s

μ_L	Liquid viscosity	Pa.s
μ_{eq}	Fluid equivalent viscosity	Pa.s
ρ_G	Gas density	kg/m3
ρ_L	Liquid density	kg/m3
ρ_{eq}	Fluid equivalent density	kg/m^3
ρ_{NS}	No-slip density	kg/m3
ΔP_{HH}	Hydrostatic pressure differential	Pa
$\Delta P_{T,ini}$	Initial design overall pressure differential	Pa
ΔP_{ss}	Steady-state pressure differential	Pa
ΔP_T	Overall pressure differential	Pa
ΔP_f	Friction pressure differential	Pa
ΔP_i	Pressure differential at ith well set	Pa
α	Optimization weighting factor	------
β_L	Liquid phase bulk modulus	Pa
β_G	Gas phase bulk modulus	Pa
β_{eq}	Fluid equivalent bulk modulus	Pa
θ	Pipeline inclination angle	degree
ε	Pipeline inner surface roughness	m
υ	Poisson's number	------

1 INTRODUCTION: STATE OF THE ART, RESEARCH CHALLENGES AND OPPORTUNITIES

1.1 Subsea Field Development Lifecycle

Since the 1950s, the world energy demand has been rising steadily. Even though a lot of effort and a considerable number of initiatives and inventions in the field of renewable energy resources have reduced their use, fossil fuels such us crude oil, natural gas, and coal make up the majority of the global energy consumption, accounting for almost 84% as shown in Figure 1-1. Hence, the oil and gas production has become one of the major contributors to sustain the stability of the world's energy supply.

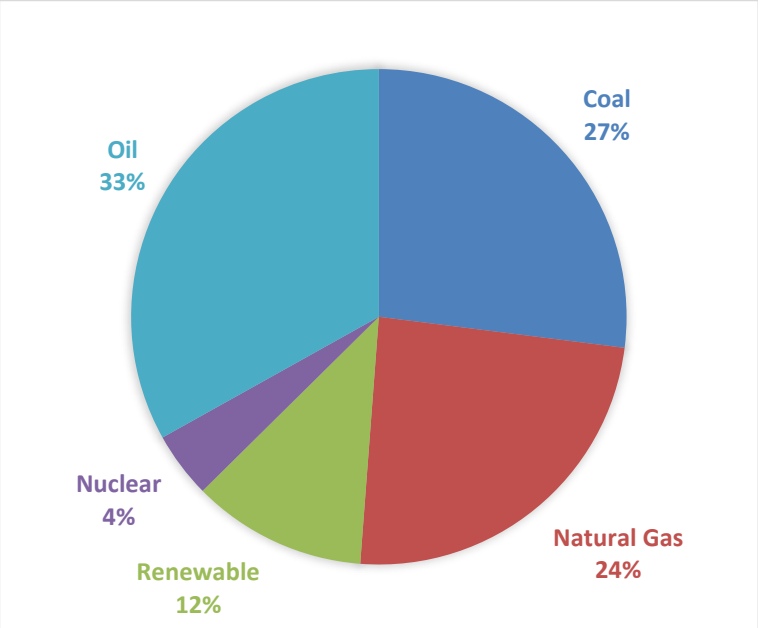

Figure 1-1: Global Primary Energy Consumption By Fuel In 2019 [1]

Among the fossil fuels production industry compartments, offshore oil and gas industry has become to gain position as a global lead provider. Starting in early 1970s, the concept of developing offshore subsea fields has been considered as a focus point for many industry players. Hence, the start of the discipline of subsea engineering describing all type of configurations enabling the connection of a well and associated equipment below the water surface or what has been called “subsea production systems”.

This industry was based in its early stages on subsea completions located in less than 1000 ft below water surface (shallow- water completions). However, in the past 50 years, oil, and gas onshore and shallow-water reserves have been depleted. Therefore, as an alternative, supported with all the advancement, innovations and the new capabilities deployed to be able to remotely control and operate equipment, the subsea systems have advanced in an increasing pace from shallow-water to be developed at water depths of up of 10000 ft (deep-water completions). This advancement has been accompanied with many challenges and problems for the offshore industry naming water depth, weather conditions, ocean currents, critical operating conditions like high pressure and high temperature (HPHT), equipment reliability and integrity as well as subsea wells accessibility and sustainability. Such criticality and complexity make the offshore oil and gas production a highly specialized industry requiring specific engineering aspects.

Due to the mentioned challenges described above, the task of Subsea field development is a long and complicated procedure. Typically, the subsea field development process consists of four major stages as described in Figure 1-2. As

presented the development process starts with the filed survey and ends with the reservoir total recovery and the field abandonment.

Figure 1-2: Subsea Field Development Process

These stages are precisely described as follows: the “Exploration” stage, includes all discovery and exploration activities of potential oil or gas geological reservoirs. Then, the second stage starts, referred to as the “Field Development phase. At this stage, engineers will be working on the concept of possible development plans involving the major key development milestones. Precisely, this phase can be conducted following three sequential studies: Appraisal/ assessment study, Development Planning, or pre-FEED analysis and finally the Development phase or FEED analysis. Once a development plan has been selected and get approval for investment from the operator, the “Execution” stage is led to execute the Engineering, Procurement, Construction, and Installation (EPCI). From that point, the subsea field will enter the stage of “Life of field”.

More details about the specification of each of the subsea field development lifecycle is presented in Figure 1-3.

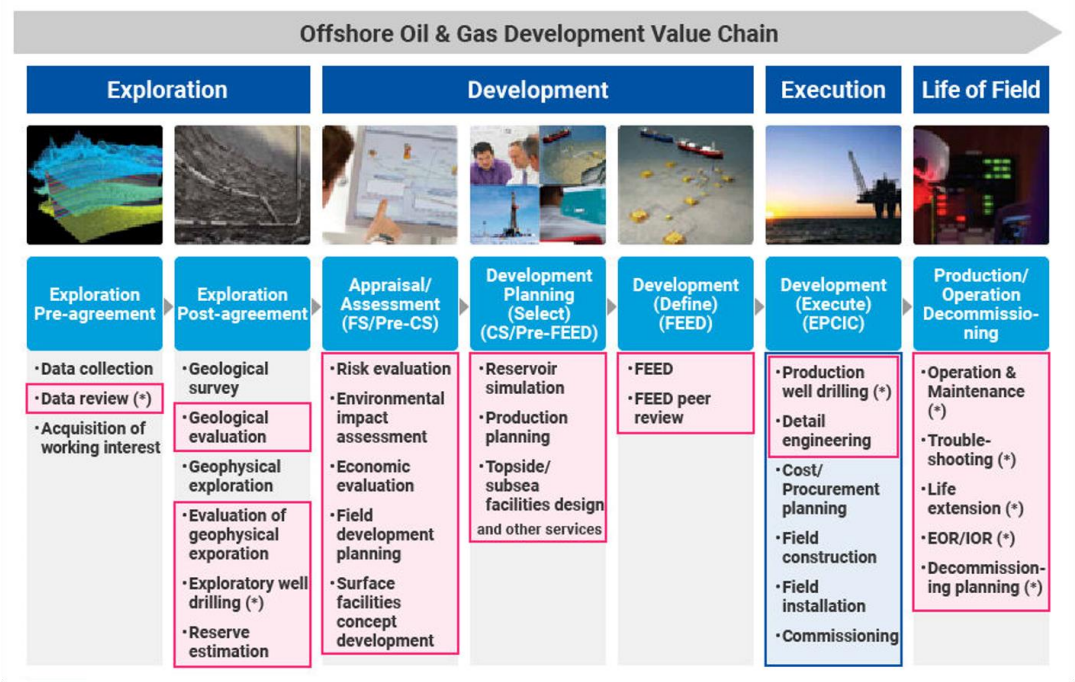

Figure 1-3: Offshore Oil and Gas Development Value Chain [2]

As mentioned above, a broad range of topics is involved on the FEED studies including construction materials, proven health monitoring technologies, environmental conditions such as depth and seabed topology, drilling costs, oil prices, and operation and production requirements. The inclusion of all these factors makes the FEED studies of subsea field architecture optimization a mega-system engineering challenge.

1.2 Subsea Production Systems

A subsea production system is presented as the arrangement scheme different subsea components in order enabling the exploration and the transmission of fossil fuels from

an under-water reservoir to a floating production, storage and offloading (FPSO) facility or directly to an onshore terminal. Mainly, a subsea production system is presented as multi-physics systems carrying non-Newtonian fluids from the seabed to a tieback. Different configurations can define a subsea production system, depending on the nature of the subsea field. Hence, different types of individual subsystems comprise a subsea production system. These subsystems can include wellheads, Christmas tree (X-trees), Pipeline End Manifold (PLEM), Pipeline End Termination (PLET) systems, manifolds, risers, flowlines and jumpers (Figure 1-4).

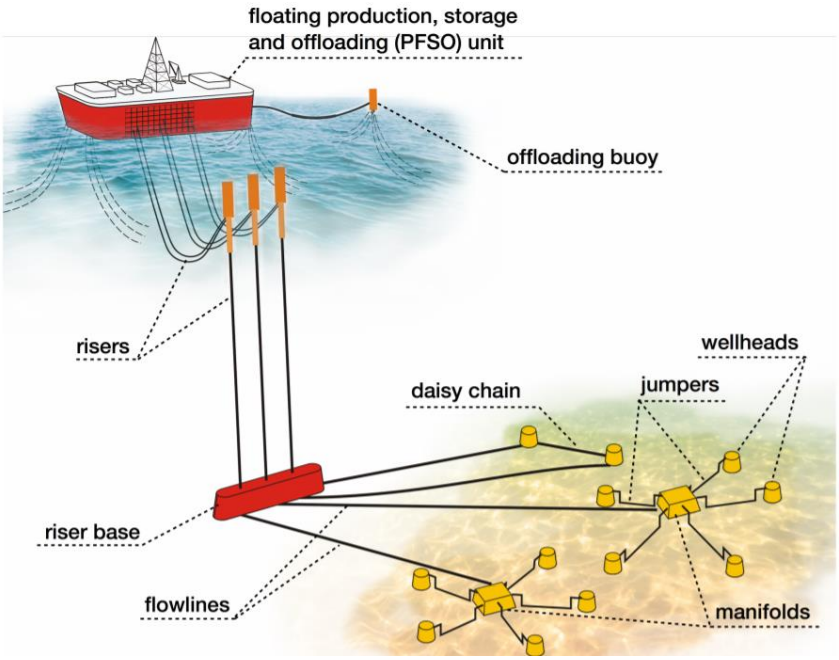

Figure 1-4: Subsea Production System Schematic [3]

Owing to its expected service life spanning decades of production, FEED studies are performed to ensure that the subsea field architecture is optimal for its specific location, depth and production requirements, thus balancing capital expenditures

(CAPEX) and operational expenditures (OPEX) and maximizing net present value (NPV) using the most reliable, safe, and cost-effective solution available at the time.

1.3 Subsea Layout Optimization

1.3.1 State of the Art

The complexities and challenges in the subsea field architecture design process have received a variety of mathematical approaches and solutions. Numerous investigations concerning subsea field architecture optimization have produced solutions that address various aspects of the design. Many of these investigations focused on maximizing the production rate within a subsea production system as well as reducing the installation and facilities cost. Proposed in [4] is a solution based on a mixed integer linear problem model (MILP) to optimize the NPV within a subsea gathering system. The method of solution integrated a set of constraints dealing with the reservoir nonlinear performance, surface pressure and drilling rig resources. Presented in [5] is a mixed integer programming (MIP) model that maximizes the NPV by considering the pressure of each reservoir. In [6], a solution was developed using a multi-period non-convex mixed-integer nonlinear programming (MINLP) model seeking to maximize the NPV for the different stages of the field life cycle.

More detailed solutions have also appeared in the literature with the focus of optimizing connections (pipeline routing layout and sizes) among the subsea components. Precisely, these investigations seek solutions to optimally interconnect the various fixed facilities subject to design requirements. Developed in [7] and [8] are genetic algorithms (GAs) based solutions identifying optimal pipeline sizes for a natural

gas network subject to flow rates, pressure differential and costs requirements. An offshore production field optimization methodology was derived in [9] optimizing the piping routing among the different facilities. This solution included diverse subsea field architecture features such as its hydraulic and technical properties, its economic production flowrates, and its separation process involving existing production facilities. Other similar studies have been proposed in [10-12]. In these investigations, optimal solutions are created that extend existing gas piping networks. The extension was accomplished by introducing solutions that balance the trade-offs among the overall system hydraulic performances, the topological profile of the seabed and the operating and installations costs. Although the focus on the effect of the reservoir performances on the overall subsea field architecture layout, the proposed methodologies have not considered the different issues that can result from the complexity of the fluid behavior within the piping system. Hence, the effect of this complexity on the overall system robustness and integrity have not been taken into consideration. Omitting these issues can result on an underperforming system especially if the system is operating under conditions where structural problems can occur namely corrosion erosion and wax deposit.

A body of knowledge exists in the literature for facilities locations optimization approach. One solution introduced in [13] used the binary approach of 0s and 1s within a linear programming model. The model was used to identify an optimal network connecting the reservoir to the topside terminal through optimal locations of the manifolds and the FPSO units. Another model-based approach was presented in [14] based on the concept of the “clustering manifold”. The motivation for this work was to

develop a method based on partitioning the subsea wells into groups, especially applicable to large subsea fields. The result of this grouping phase produced an efficient optimization process identifying locations of the cluster manifolds and their connections with the wellheads. Another method optimizing the number and location of pipeline end manifolds (PLEMs) and its connections with the cluster manifolds and FPSO was proposed in [15]. This method was successfully applied in [16] to design the subsea layout using 4-slot and 6-slot manifolds. An MILP optimization method to design subsea production networks was provided in [17] accounting for the number of manifolds and platforms, appropriate locations, well assignment and pipeline diameters as well as the reservoir properties. In these presented works, the overall optimization problem has been treated as a 2D problem where no study concerning the effect of the topological profile of the overall field has been evaluated. Since the major component of a subsea system is presented by the hydraulic properties of the flowing fluid, then understanding its pattern represents an essential requirement into having a well-designed system. These properties are directly related to the variation of the topological profile. This is precisely justified by the fact that any variation in pipes elevation can result in a major change in the fluid pattern and behavior. Hence, patterns such as slugging flow can be observed within the system which is remarkably a big issue within the oil and gas industry that is preferably be treated at the design phase of a subsea field development to avoid any catastrophic scenarios during the production stage.

Another major challenge during the development of a subsea field is related directly to nature of the seabed where the different components of a production system are located. In fact, combining topographic constraints and infrastructure optimization is

the problem to solve as it represents a high-fidelity translation of the real situation. Included in [18] are seabed constraints in addition to the pipelines structural properties within an optimization process in order to find the best pipeline routing scheme. This idea was enhanced in [19] for the case of a single pipeline and [20, 21] for a piping network, where solutions to minimize the total length of the piping system were proposed. This was achieved by discretizing the pipeline into several branches of straight lines and curves and by considering more constraints such as presence of obstacles within the field as well as on-bottom stability.

1.3.2 Challenges and Opportunities

Although, many solutions have been presented in order to demonstrate efforts and methodologies deployed for the purpose of a subsea field architecture layout optimization, we can observe that all the proposed solutions do not cover all the aspects that can interfere with this process such us flowing fluid properties and flowing conditions, flow assurance issues as well as field deployment environment characteristics and challenges .

1.3.2.1 Multiphase Flow Hydraulic and Thermal Modeling in Subsea Pipelines

In real case subsea fields, the flowing conditions are not constant and highly sensitive to the changes of the overall system layout and configuration. This is mainly related to the fact that hydraulic and thermal properties are directly correlated with the changes of both pressure and temperature as well as seabed topology and elevation variations.

Hence, a major addition to the overall optimization process is the ability to track the variation of both pressure and temperature at any level of the subsea system. Such a task requires a good and accurate tool to predict both pressure and temperature along complex piping systems configurations and translate that into updating the fluid properties respectively.

Deploying such self-adapting process can give more elaborated insights on the changes of the fluid behavior and properties and flowing patterns. This represents an essential asset especially for structure and operations condition-based monitoring along with flow assurance issues prediction and analysis.

1.3.2.2 Flow Assurance Challenges

Producing subsea reserves has been always accompanied by critical flow assurance challenges. Such analysis is considered as an essential part during the design and operation phases of a subsea production field. Flow assurance issues are related to all the problems interfering with the integrity of any of the subsea system components contributing to disturbing the continuous and economical flow of the hydrocarbons from subsea wells into the hosting facility. This capability can be altered, or degradable due to solid deposits concerns such us plugging due to wax, asphaltene, and gas hydrate plug formation. In addition, equipment and flowline integrity issues are mainly related to the occurrence of corrosion, erosion, chemical incompatibility issues and/or mechanical stresses induced by unexpected fluid slugging or harsh flowing conditions which also fall within the flow assurance umbrella.

Therefore, being able to accurately quantify and assess these phenomena discussed above is a crucial task to predict; mitigate; control or prevent any of the listed issues.

1.3.2.3 Optimization Problem Complexity

Subsea field layout development is based on an optimization problem defined via highly non-linear sub-models. Hence, the convexity of the optimization space is not guaranteed, which make the search for a global solution a hard task to achieve. Some attempts have been developed toward this goal and this has been illustrated by the deployment of genetic algorithm-based solutions. However, solving such problems requires a large computational effort. To avoid such issue and be able to approach the global solution as possible as it can be, a simplified scatter search methodology has been incorporated within the presented work in order to reduce the optimization time without altering the accuracy or the convergence of the overall solution. Such approach offers a lot of potential to deploy the proposed methodology as a modeling environment for tasks that requires fast calculation efforts as well as real-time prediction and monitoring analysis.

1.3.3 Research Objectives

The objectives of the proposed research are focused on the development of reduced-order models deployed for the purpose of simulation, optimization, and design of subsea systems. Precisely, the focus of the presented thesis is the integration of reduced-order multi-physics models to develop an automated model-based environment for the optimization design of subsea field layout under production and flow assurance constraints during the pre-FEED stage of a subsea field development project.

In a subsea field, whether in the upstream, mid-stream or downstream compartment, the fundamental parts constituting any of the subsea equipment are

pipelines. Therefore, it is crucial to develop reliable, accurate and fast tools to describe both hydraulic and thermal dynamic responses in a pipeline. Having such capacity, will also allow more accurate assessment of flow assurance related issues, precisely internal carbon dioxide pipeline corrosion, flow patterns tracking as well as fluid properties variation assessment.

The main objective of the proposed research is to present a reliable, computationally affordable and engineering efficient methodology that can be used by experts during the design phase of subsea fields. This methodology is presented as an improved alternative approach for traditional design and optimization practices in the subsea industry giving the fact of being developed as an automated process that can offer a wide range of results and present an environment that can automatically simulate, test, and analyze different types of design scenarios subject to diverse optimization objectives.

The integrated model-based methodology is developed by coupling different reduced-order, physics-based models. Precisely, several models are deployed, namely, a multiphase flow model coupled with a thermal model to capture the hydraulic and thermal behavior of a steady state multiphase flow within pipelines network. Both hydraulic and thermal models are coupled via a properties adaptive block, assuring an estimation of the hydraulic and thermal properties of the fluid as a function of the operating conditions (temperature and pressure). Different constraints are introduced to cope with flow assurance and environmental challenges. The overall network is designed and optimized by considering erosion, corrosion, and wax appearance acceptable thresholds.

Being a system-based simulation environment, the developed platform offers the possibility to include extra constraints as well as additional modules describing different type of equipment, depending on the studied problem and the user preferences. In addition, such modeling environment can be used as a digital-twin to virtually simulate subsea operation activities allowing a wide range of engineering applications including hydraulic properties tracking, flow assurance issues forecasting and mitigation, integrity management and real-time condition-based monitoring of subsea equipment, production process, etc...

1.4 Thesis Outline

Following is the outline of the presented thesis. In chapter 2, an experimental validation of a low-dimensional two-phase flow transient model is presented. The proposed reduced-order model predictions are compared to the commercial package "OLGA" results for different gas-volume fraction (GVF) levels. Then, the performances of both models are compared to transient experimental data collected at the multiphase flow loop facility at the National University of Singapore (NUS), accessing how accurate the low-dimensional and the OLGA model can capture the two-phase flow dynamic behavior at both low and high GVF levels.

In chapter 3, based on the steady-state results from the multiphase flow modeling approach presented in chapter 2, a newly data-driven model for CO_2 corrosion prediction is introduced. Precisely, a "Parameter Varying" (PV) corrosion rate model is developed by introducing varying model coefficients illustrating the effect of flowing conditions on corrosion rates. Such influence is presented as a nonlinear correlation

between the pH and the flow velocity, which are not derived from physics, instead being the result of a data driven approach based on a system identification methodology. At the end of this chapter, a study case is introduced to highlight the possibility of deploying the proposed data-driven corrosion rate model as the basis for subsea architecture optimization design.

Integrating the described modeling approaches listed above, along with others flow assurances issues assessment tools such us erosion and wax appearance descriptive models has been the basis for the work presented in chapter 4. Precisely, a deep-dive description of the automated model-based approach developed for subsea field layout optimization is presented. A well detailed illustration of the different sub-models coupled to develop the proposed methodology along with the hybrid optimization process is included. Additional sections have been incorporated to highlight the approach used to describe the different other element interfering with the optimization routine, namely the 3-D seabed representation as well as the algorithm used for the piping layout determination (in this case the Dijkstra algorithm). At the end of this chapter, a study case is included to illustrate the potential of using such model-based design optimization methodology for subsea field layout design along with several analysis such us subsea wells clustering scenarios, insulation properties variations and optimization trade-off configuration to emphasize their effect on the overall optimization results.

Finally, in Chapter 5, the main findings and conclusions of the proposed research are summarized. Several outstanding issues are identified and suggestions for future investigations are given.

2 LOW PRESSURE EXPERIMENTAL VALIDATION OF LOW DIMENSIONAL ANALYTICAL MODEL FOR TWO-PHASE TRANSIENT FLOW IN HORIZONTAL PIPELINES

2.1 Introduction

Multiphase flow is the simultaneous flow of two or more phases/components of gas, liquid, and/or solids. This category of flow has a wide range of applications ranging from medical and biological to automotive, aerospace, power generation and oil and gas industries. In this chapter, an experimental evaluation of the transient response of the dynamic model developed by [22] is introduced. The studied model is presented as a two-phase flow model using a steady-state flow model in series with a transient model that are coupled using equivalent fluid properties. An accuracy evaluation of the two widely used steady-state multiphase flow models, namely the Beggs and Brill model [23] and the Petalas and Aziz mechanistic model [24], is introduced along with a comparison of both models against the Stanford Multiphase Flow Database [25]. The experimental evaluation is achieved using air-water two-phase transient flow in horizontal pipelines with data provided using the NUS flow loop for low pressure experiments. Both the Low-D model [22] and OLGA simulations [26] are evaluated and compared to the NUS laboratory data. The accuracy and sensitivity of the Low-D model is investigated by varying the number of modes in the model. The consequences of small amount of entrained air on the pipeline dynamic response are studied confirming entrained air within the 0% GVF case. Finally, the consistency of the Low-D and OLGA models are assessed for different GVF levels.

2.2 Multiphase Flow Modeling: State of the Art

Multiphase flow models fall in the categories of empirical and mechanistic models. Empirical models for gas-liquid flow, such as the work of Beggs and Brill [23], and Hagedorn and Brown [27], are based on correlations established using data gathered from experimental test facilities. Those models offer a simulation tool capable of predicting the multiphase flow regime based the superficial velocities of the gas and liquid. The accuracy of empirical models may be limited to the range of dataset considered. The second category includes analytical/mechanistic models, derived from the fundamental laws of fluid mechanics coupled with data driven correlations. The impact of this class of models is its applicability to different pipeline geometries and fluid properties beyond the tested conditions. Taitel and Dukler [28] determined such a mechanistic model using stability criteria of the different gas-liquid flow patterns for both horizontal and vertical pipelines. This work was then extended by Barnea [29], Xiao, Shoham, and Brill [30], Ansari [31] and Petalas and Aziz [24] offering greater depth of model accuracy and applicability.

The development of transient multiphase flow models began within the nuclear industry [32, 33]. Multiple commercial transient multiphase flow packages followed these developments adding specificity for oil and gas applications such as OLGA [26] and LedaFlow [34]. Despite the level of accuracy, they offer, the previous multiphase flow models present some limitations. Especially by since such an industry is moving toward deploying advanced data acquisition systems offering more accessibility and controllability of their production systems. Hence, the need for accurate real time monitoring and prediction tools rises significantly. In this context, the authors in [22]

derived a Low-Dimensional (Low-D) reduced order model for transient multiphase flow in pipelines. The present work is a one-dimensional transient two-phase gas–liquid flow, combining the steady-state mechanistic model presented by Petalas and Aziz [24] in series with the single phase distributed lumped parameter model in [22] through the derivation of equivalent fluid properties. Precisely, the mechanistic model presented by Petalas and Aziz [24] captures the steady-state pressure drop and liquid holdup estimation for all pipe inclinations and flowing patterns. This information is combined with different gas-volume fraction values to develop equivalent fluid properties to be used as parameters for the transient portion of the model (transmission line modal model) developed in [22]. Such modular approach is able to offer a computationally efficient and accurate solution to estimate the dynamics of multiphase flow in pipelines, reducing the computational burden of prediction seen in other multiphase flow models, thereby enabling real-time ability to estimate of pressure and flow rate along a pipeline.

To evaluate both analytical and numerical multiphase flow models, experimental data can be used to quantify the range of model applicability and accuracy. Multiple flow loops have pioneered the experimental investigations of multiphase flow systems within controlled environments. These flow loops have specific test section lengths, diameters, inclinations, and operating pressures to identify fluid characteristics. The SINTEF loop [35] is a large scale Multiphase Flow Loop with approximately 1,000 m of total pipelines length and 40 m vertical elevation. It can accommodate pressures up to 90 bar, gas flow velocities of 12 m/s and liquid flow velocities of 3.5 m/s through 4, 8 and 12-inch pipelines. This flow loop served as an input to the development of the OLGA simulation package. Other flow loops emerged at multiple universities and

research institutes including the Southwest Research Institute (SwRI) flow loop [36], the TUFFP1 loop at Tulsa University [37], the CRAN loop at Cranfield University [38], the WASP loop at Imperial College London [39] and the Colorado School of Mines flow loop [40]. Another emerging flow loop was developed at the National University of Singapore (NUS). It is presented as the only one in the world offering three different flow loops (diameter 2", 4" and 6") integrated into one test facility. Research efforts realized at this facility supports a broad range of investigations related to modeling and sensor calibrations for infield applications. Specifically, the NUS multiphase flow facility offers the capability to generate complex flow regimes within oil, water, and gas mixtures by controlling the flow rates of the different phases flowing into the flow loops. Hence, various flow conditions and flow regimes can be investigated [41].

2.3 Reduced-Order Dynamic Transient Multiphase Flow Model

Presented is a review of the low dimensional multiphase flow model provided in [22]. The parameters and modularity of the model are detailed as a primer. The steady-state and transient two-phase flow models are individually presented along with the integration process.

2.3.1 Low-Dimensional Transient Multiphase Flow Model

The multiphase Low-Dimensional transient pipeline flow model in [22] is created using an in-series model. First, the steady-state mechanistic model from [24] is implemented. Next, equivalent fluid properties are derived using parameters derived from the steady-state model. Finally, a dissipative distributed-parameter model is

created using the equivalent fluid parameters to capture the flow transients. The details of the low dimensional model development follow.

A liquid holdup-weighted parallel combination of the gas and liquid bulk moduli (β_G and β_L, respectively) is used to estimate the equivalent bulk modulus β_{eq} in (2-1). The equivalent density ρ_{eq} of the two-phase fluid is calculated as a holdup-weighted series combination of the gas and liquid densities (ρ_G and ρ_L) presented in (2-2)

$$\frac{1}{\beta_{eq}} = \frac{E_L}{\beta_L} + \frac{1 - E_L}{\beta_G} \tag{2-1}$$

and

$$\rho_{eq} = E_L \rho_L + (1 - E_L)\rho_G. \tag{2-2}$$

With these equivalent parameters, an equivalent fluid speed of sound c_{eq} is calculated as

$$c_{eq} = \sqrt{\frac{\beta_{eq}}{\rho_{eq}}}. \tag{2-2}$$

An equivalent Darcy friction factor f_{eq} is also calculated in (2-3) to match the steady-state frictional pressure gradient given by the mechanistic model. The Darcy friction factor calculation is based on the pipe geometry properties (diameter *D* and cross-section area *A*), the equivalent fluid density and the steady state flow properties (total flow rate *Q* and pressure drop ΔP_{ss}), given by

$$f_{eq} = \frac{2DA^2\Delta P_{ss}}{\rho_{eq}Q^2}. \tag{2-3}$$

Once calculated, the equivalent fluid properties are used to determine the equivalent dynamic viscosity μ_{eq} with the knowledge of flow type (laminar or turbulent). In the case of laminar flow, the equivalent dynamic viscosity is given as

$$\mu_{eq} = \frac{1}{64}\rho_{eq} V_m D f_{eq}. \tag{2-4}$$

For turbulent flow conditions, the equivalent viscosity is given by

$$\mu_{eq} = \frac{1}{2.51}\rho_{eq} V_m D \sqrt{f_{eq}} \left[10^{-\frac{1}{2\sqrt{f_{eq}}}} - \frac{\varepsilon}{3.7D}\right], \tag{2-5}$$

where V_m is the gas and liquid mean velocity and ε is the pipe roughness.

The derivation of the dissipative distributed-parameter model used in this study is detailed in [22] and is experimentally validated in [42, 43]. The dissipative distributed-parameter model viscous losses in the presence of turbulent flow is captured using a lumped turbulent friction resistance term as described in [22].

For laminar flow with a Mach number less than unity with a high length to diameter ratio and a low normalized density variation, the Navier-Stokes equations, and the equation of state for the pipeline matrix model are

$$\begin{bmatrix} P_{out} \\ Q_{in} \end{bmatrix} = \begin{bmatrix} \frac{1}{cosh(\Gamma)} & -\frac{Z_c \sinh(\Gamma)}{\cosh(\Gamma)} \\ \frac{\sinh(\Gamma)}{Z_c \cosh(\Gamma)} & \frac{1}{\cosh(\Gamma)} \end{bmatrix} \begin{bmatrix} P_{in} \\ Q_{out} \end{bmatrix}, \tag{2-6}$$

where Γ is the propagation operator and Zc is the characteristic impedance. The added lumped turbulent frictional resistance is included as

$$R_{Tur} = \frac{f_{eq}\rho_{eq} LQ}{2DA^2} - R_{Lam}, \tag{2-7}$$

where R_{Lam} is the steady state frictional resistance of the pipeline assuming laminar flow. The final matrix representation of the pipeline dynamics is

$$\begin{bmatrix} P_{in} \\ Q_{out} \end{bmatrix} = \begin{bmatrix} \dfrac{Z_c}{Z_c cosh(\Gamma) + R_{Tur}\sinh(\Gamma)} & \dfrac{Z_c^2\sinh(\Gamma) + R_{Tur}Z_c\cosh(\Gamma)}{Z_c cosh(\Gamma) + R_{Tur}\sinh(\Gamma)} \\ \dfrac{-\sinh(\Gamma)}{Z_c cosh(\Gamma) + R_{Tur}\sinh(\Gamma)} & \dfrac{Z_c}{Z_c cosh(\Gamma) + R_{Tur}\sinh(\Gamma)} \end{bmatrix} \begin{bmatrix} P_{out} \\ Q_{in} \end{bmatrix}. \quad (2\text{-}8)$$

Substituting the lumped turbulent resistance R_{Tur} by zero results in recovering the dissipative transmission line model in (2-6). The pipeline dynamic model in (2-8) has been compared to the work of Johnston in [44] and shows agreement.

The hyperbolic transfer functions in (2-8) are replaced with a modal approximation of the fluid line dynamics as defined in [45], and later in [46]. The resulting transfer functions TF_{jk} in (2-8) become a finite sum of second order rational transfer functions, given as

$$TF_{(jk)} = \sum_{i=1}^{n} \frac{a_{i(jk)}s + b_{i(jk)}}{s^2 + 2\xi_{ni(jk)}\omega_{ni(jk)}s + \omega_{ni(jk)}^2}, \quad (2\text{-}9)$$

where *n* represents the number of system modes and '*s*' is the Laplace operator. The parameters $\omega_{ni(jk)}$ and $\xi_{ni(jk)}$ are the natural frequency and the damping ratio of the i^{th} mode, respectively. The modeling approach presented by the three steps detailed above can be summarized by the following diagram.

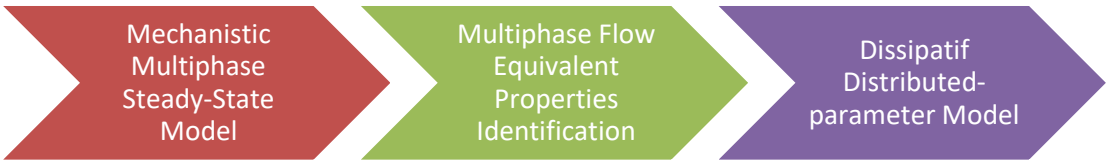

Figure 2-1: Multiphase Flow Reduced-Order Model Structure

2.3.2 Steady-State Multiphase Flow Models Comparison

The Low-Dimensional model in [22] is given as a coupling between two distinct models: a steady-state model and a dissipative distributed parameter transient model. Because of this modularity, the individual subdomain models can be evaluated. For the steady-state mechanistic model, a comparison of the Beggs and Brill model [23] and the mechanistic multiphase flow model introduced by Petalas and Aziz [24] are performed. Both models are then compared to experimental data presented in the Stanford Multiphase Flow Database [25] and the steady-state module provided in the OLGA Multiphase Flow Simulator [26]. The outcomes from this investigation will be used to select the steady-state multiphase flow model for this study.

The empirical correlation presented by Beggs and Brill [23] in and the mechanistic model proposed by Petalas and Aziz [24] are compared to the results from the steady state OLGA multiphase flow model [26] and the Stanford Multiphase Flow database [25].

The Stanford multiphase flow experimental database contains 5,659 data points. This is the result of measurements performed from in-lab and from infield oil and gas tests. The datapoints were collected from 15 sources where a wide range of fluid properties and geometric characteristics are tested. In addition, the dataset offers a variety of inclinations and flow directions (from vertical downward to vertical upward). These variables are used as inputs to the steady state mechanistic model to estimate the liquid holdup and pressure drop within a pre-defined pipeline. A summary of the distributions of the different attributes presented in the Stanford Multiphase Flow database is shown in Figure 2-2.

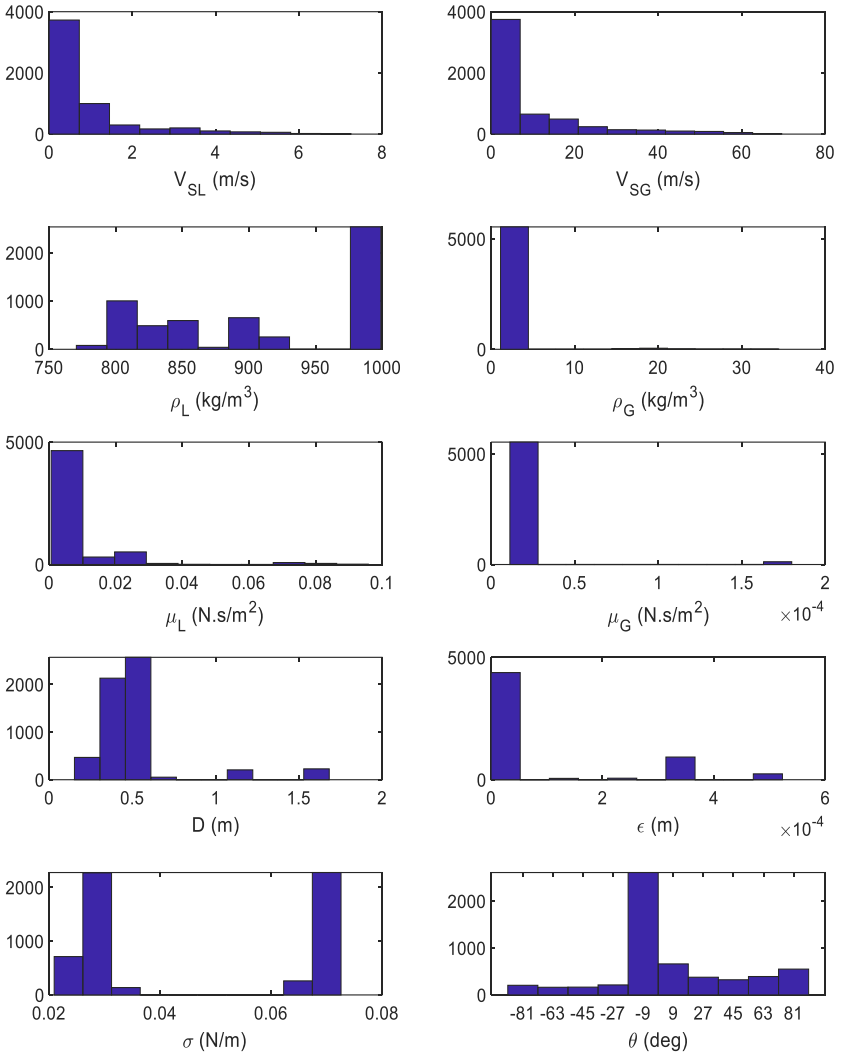

Figure 2-2: Stanford Multiphase Flow Database Variables Distributions

Several flowing conditions are identified within the Stanford Multiphase Flow database offering a variety of flow regimes. Specifically, the flow patterns presented include bubbly, plug, stratified, froth, slug, annular mist, and dispersed bubbly flow. Therefore, to compare the previously listed steady-state multiphase models (Beggs and Brill, Petalas and Aziz, and OLGA), an evaluation of the accuracy of each model on

calculating the liquid holdup and pressure drop for each flow regime is evaluated. The results of the comparison are shown in Table 2-1.

Table 2-1: R^2 for the Steady-State Multiphase Flow Models vs Stanford Dataset

Flow Regime	Pressure Drop Gradient			Liquid Holdup		
	Beggs & Brill	Petalas & Aziz	OLGA	Beggs & Brill	Petalas & Aziz	OLGA
Bubble	0.775	0.856	0	0.870	0.932	0.887
Plug	0.699	0.718	0	0.823	0.898	0.825
Stratified	0.656	0.920	0	0.766	0.847	0.781
Froth	0.766	0.899	0.323	0.560	0.947	0.857
Slug	0.610	0.857	0	0.793	0.921	0.892
Annular Mist	0.774	0.904	0.002	0.701	0.897	0.841
Dispersed Bubble	0.935	0.861	0.512	0.890	0.922	0.812

From Table 2-1, it is observed that the Petalas and Aziz Multiphase Flow model provides a more accurate prediction for different flow regimes and thus selected for this study.

2.4 Dynamic Multiphase Flow Model Evaluation

Presented in this section is an evaluation of the transient flow response predicted from the dissipative distributed parameter transient with independent predictions. Namely, a comparison of the dissipative distributed parameter transient simulation with transient experimental data and with the OLGA Multiphase Flow Simulator is performed. The experimental data used in this section is provided by the NUS Multiphase Flow Loop. Results are analyzed based on variation on the GVF level as well as the amount of entrained air present within the pipeline.

2.4.1 NUS Experimental Facility

The experimental data used for validation in this work have been collected at the Multiphase Flow Loop facility built in mechanical engineering department at the NUS.

The presented flow loop facility enables three phase flow analysis. Introducing an oil-water-air flow, this facility can be the hub for different studies regarding pipelines, separators, flow meters, pumps, etc. More details about the schematic of the used facility are presented in Figure 2-3.

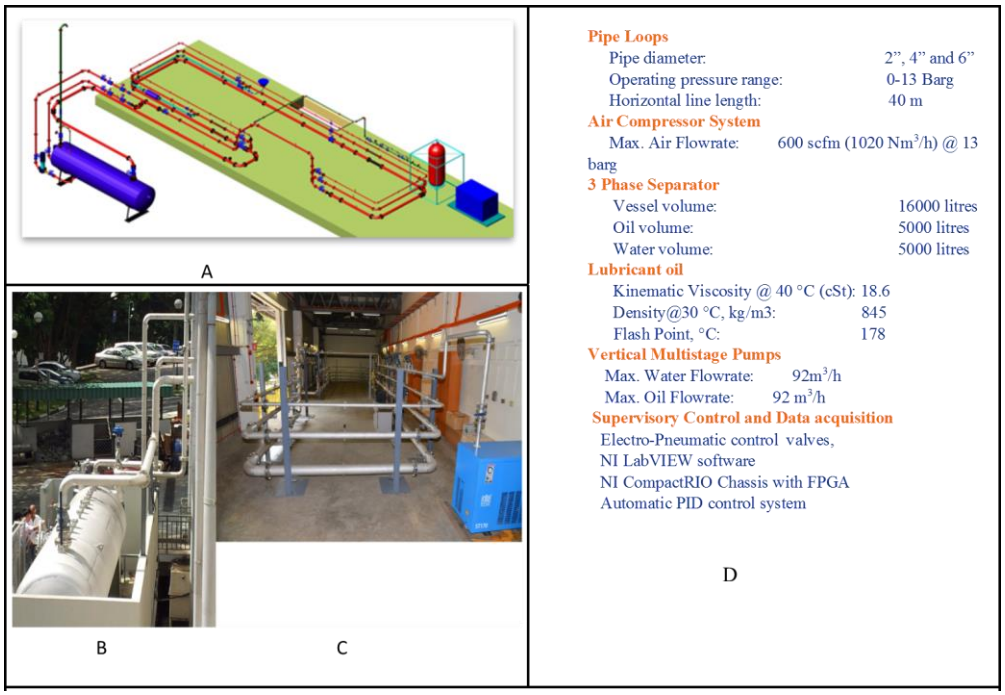

Figure 2-3: Schematic Views and Pictures of the Experimental Setup: A) Full 3D View, B) Separator Tank, C) Pipe Flow Loops, D) Specifications [47]

To perform multiphase flow studies, indoor measured flow rates of air, water and oil phases are mixed at a pressure rate that can go up to 13 barg. The flow loop has been built using interchanged seamless stainless-steel sections with 3 m length.

To be able to automatically control all variables within the flow loop facility, a compact RIO main chassis is used supplied by National Instruments. As described in [47] the control unit "consists of a real-time processor, a reconfigurable Field Programmable Gate Array (FPGA) and the IO modules" integrated within a supervisory

control and data acquisition (SCADA) software developed within the LabVIEW environment.

To be able to achieve a broader range of flowing conditions, dried air, where humidity has been removed, has been supplied through a parallel circuit containing "two compressors connected in parallel to a receiver tank" [47]. For flow rates measurement two flow meters types are used: for low flow rates (0 to 17Nm^3/h) a differential pressure flow meter is used, although, for high flow rate (0 to 1115 m^3/h) a vortex gas flow meter with uncertainty of 1% is employed.

As mentioned above, the three phases flows are controlled using the control software implemented as a PID algorithm within the LabVIEW software. All the measurements sensors used to control and measure the different properties of the flowing phases (pressure, temperature and density) along the flow loop are presented in Figure 2-4.

Within the flow loop, airflow is calculated using ideal gas equation providing the inlet pressure 2inP1 (Figure 2-4). Inlet measurements of air pressure and temperature are also collected (T1 and P1-air respectively) as well as in pipe properties (2inP7 and 2inT6). In the other hand, water is circulating from the three phase separator tank toward the flow loop via a control valve CV3 (Figure 2-4). Water flow rate and water density are measured using a Coriolis flow meter with "an uncertainty of ±0.3% of the indicated value" [47]. Both phases are then mixed within a mixing section where phases exchange is prevented using check valves.

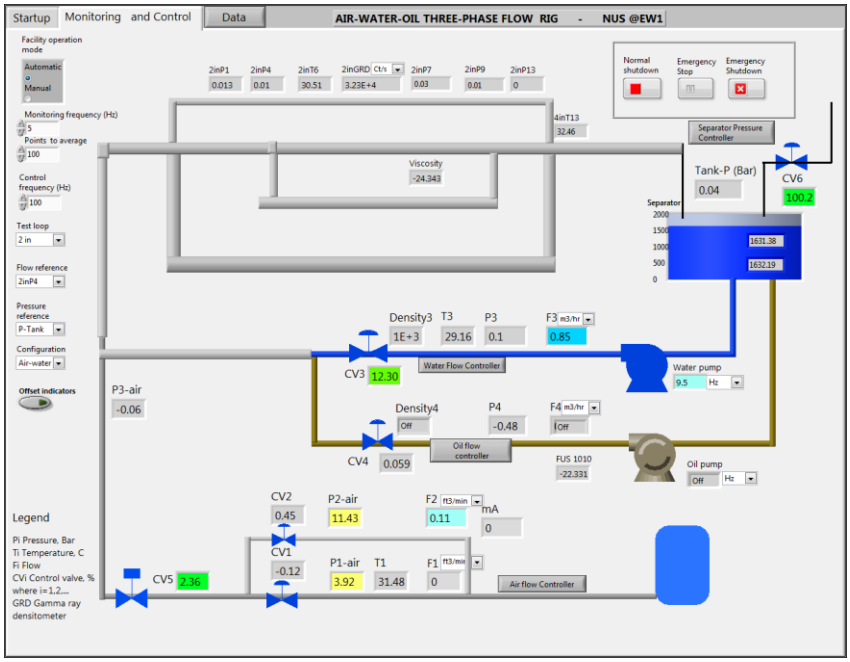

Figure 2-4: Experimental Setup Control Panel [47]

As detailed in [47] "the test section consisted of a 40 m long loop in a rectangular shape". To assess the effect of both pressure and temperature, sensors have been placed at different locations along the flow loop as illustrated in Figure 2-4 and Figure 2-5.

The NUS flow loop facility is consisted of a rectangular flow loop connected to a three-phase separator tank. This latter tank is used to separate phases in order to release the air phase to the atmosphere through valve CV6 as shown in Figure 2-4, while the liquid phase is redirected toward the flow loop again.

Although being a three-phase flow loop facility, all the experimental studies shown in this work are mainly concerning air-water mixtures in horizontal pipelines.

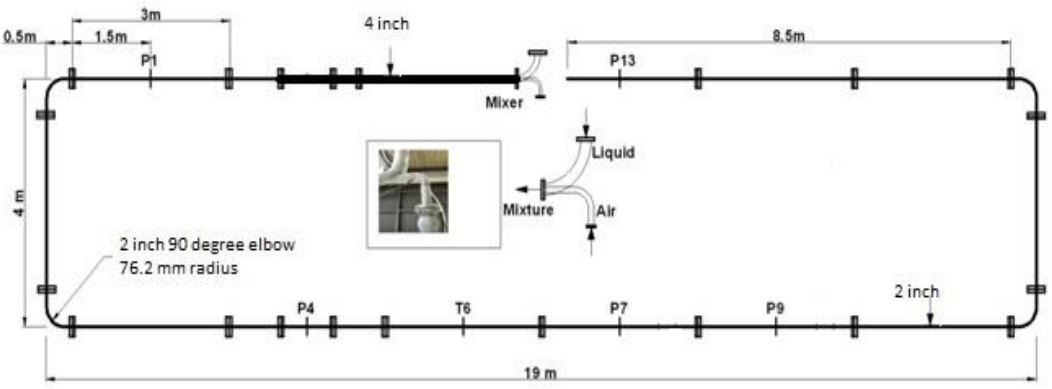

Figure 2-5: Top View Schematic of the Physical Configuration of the 2-inch Test Loop, Mixing Section and Instrumentation [47]

2.4.2 Dynamic Multiphase Flow Model Evaluation

To minimize sensor noise, a filtering process is implemented. All measured variables were filtered using the weighted average smoothing approach giving by the following tricube function

$$w_i = \left[1 - \left(\frac{abs(i)}{(npts-1)/2}\right)^3\right]^3, \tag{2-10}$$

where i and w_i are respectively, the position and the weight associated to the current data point within the sample window of size $npts$. The resulting filtered signal is given by

$$y_i = \frac{\sum_{k=-(npts-1)/2}^{(npts-1)/2} w_{i+k} y_{i+k}}{\sum_{k=-(npts-1)/2}^{(npts-1)/2} w_{i+k}}. \tag{2-11}$$

An example of the smoothing procedure for the case of 10% GVF is presented in Figure 2-6.

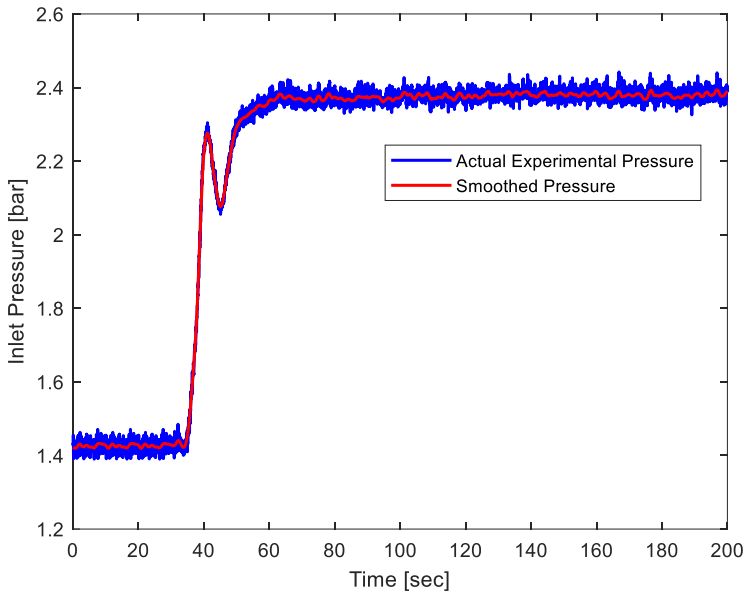

Figure 2-6: Smoothing Procedure Results, 10% GVF Case

2.4.2.1 Effect of the Number of Modes on the Low-D Model Accuracy

The authors in [22] investigated the effect of the number of modes based on the estimation given by (2-9) through a sensitivity analysis. The focus of this section is on validating the distributed dissipative low dimensional model predictions with the experimental results for different model orders denoted as *n*.

As shown in Figure 2-7, a higher number of modes results in a better estimation of the transient inlet pressure. However, the higher number of modes requires greater computation demand albeit significantly less than that associated with a CFD investigation. Thus, a trade off exists between the number of model modes and prediction fidelity as suggested in [22].

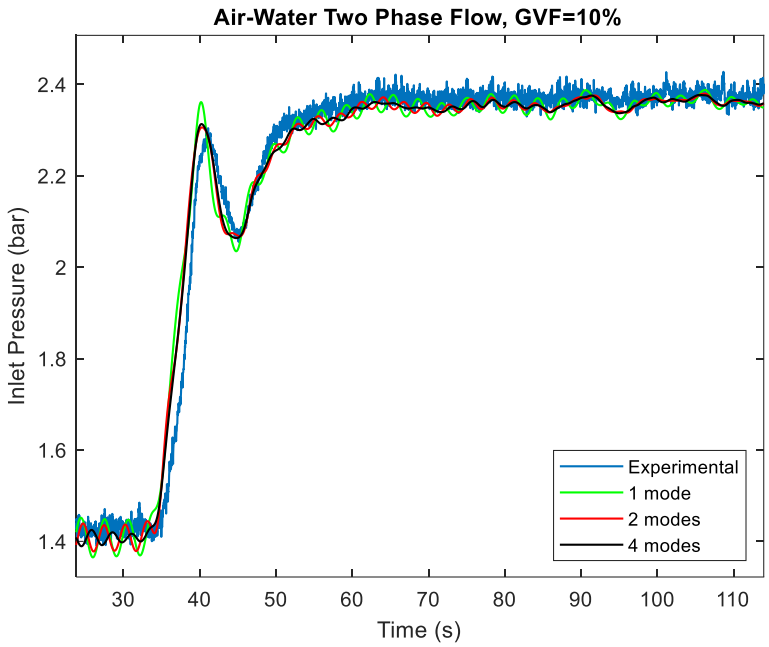

Figure 2-7: NUS Experimental Results vs. Low-D Model Predictions as Function of the Truncation Order n, 10% GVF Case

Shown in Figure 2-8 are the computation time and the Mean Absolute Percent Error (MAPE) as a function of the number of modes considered in the Low-D model.

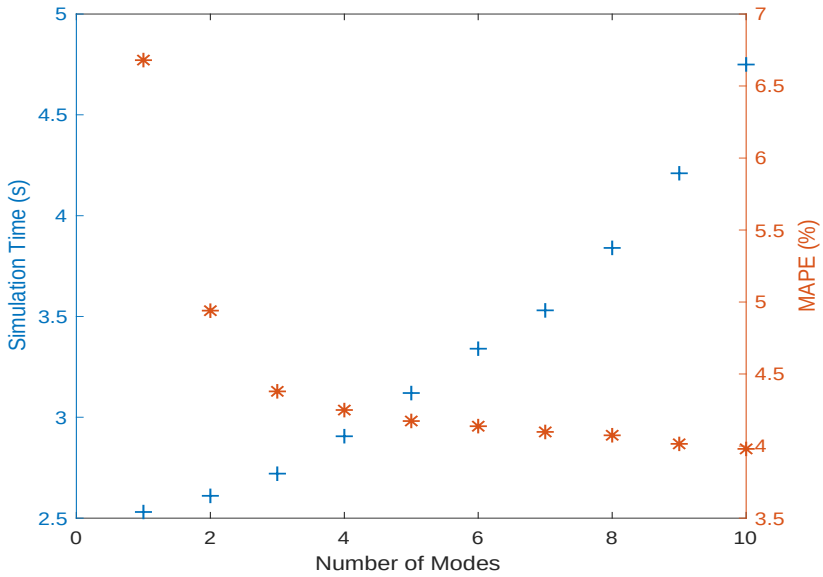

Figure 2-8: Simulation Time vs. MAPE

The expression used to evaluate the Mean Absolute Percent Error (MAPE) for a vector **X** with *N* values X_i is given as

$$MAPE = \frac{1}{N}\sum_{i=1}^{N}\left|\frac{X_i^{actual} - X_i^{estimated}}{X_i^{actual}}\right|, \tag{2-12}$$

where X_i^{actual} is the actual value and $X_i^{estimated}$ is the estimated value.

As the number of modes is increased, the MAPE diminishes as a function of the number of modes while the computation time slightly increases. This tendency is inverted when considering a higher number of modes where the computational time increases dramatically without a significant improvement in the model predictions. Hence, selecting the appropriate number of modes is important depending on the desired model application and available computing power. For the remainder of the paper, and based on the tradeoff analysis present in Figure 2-8, 4-modes will be used to approximate the transfer functions in (2-9).

2.4.2.2 Effect of Entrained Air on the Pipeline Dynamic Response

The transient single-phase flow in pipelines has been extensively studied in the literature [46, 48]. However, the effect of small amounts of entrained air on the pipeline dynamic response has not been established. Air pockets form inside the pipeline due to bubble entrainment through the action of pump suction or can be released as the pressure of the liquid decreases along the pipeline. Under standard conditions, water can contain up to 2% of entrained air per volume unit [49]. Depending on the application, the effect of entrained air can be either beneficial or detrimental. The presence of air in pipeline systems can result in numerous problems including loss of carrying capacity, disruption of the flow, reduced pump and turbine efficiency or create cavitation problems under

low-pressure conditions causing significant damage to the pipeline structure. The speed of waves propagation is also reduced substantially with the presence of air in the pipeline and the damping can be increased allowing a shorter length of the fortified zone required for the High Integrity Pressure Protection System (HIPPS).

In this section, the National University of Singapore Multiphase Flow Loop, the Low-D two-phase flow model [22], and the OLGA multiphase flow simulator [26] are used to investigate the effect of the entrained air on the pipeline dynamic response. Three cases are investigated using the water pump to vary the flow in the loop by stepping the liquid superficial velocity from 0.1 m/s to a pre-specified value while keeping the air compressors constant. The summary of the three cases is listed in Table 2-2.

Table 2-2: Liquid Superficial Velocity Variation

Case Number	Initial Liquid Superficial Velocity (m/s)	Steady-State Liquid Superficial Velocity (m/s)
1	0.1	2
2	0.1	3
3	0.1	4

The measured inlet pressure and the those predicted by the Low-D model and the OLGA simulations are given in Figure 2-9 – Figure 2-11. Both models show agreement of the steady-state predictions of the inlet pressure due to a step increase in the water flow with the experimental data. However, the Low-D model and the OLGA simulations are characterized by higher frequencies of oscillation associated with higher overshoot.

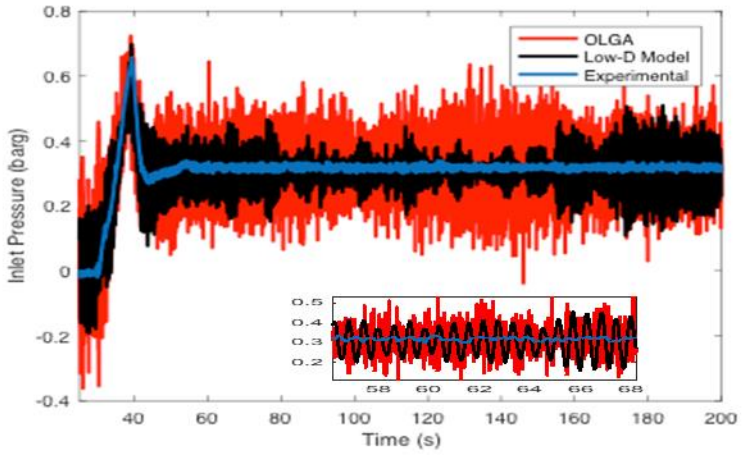

Figure 2-9: Experimental vs. Simulations (Liquid/Case 1)

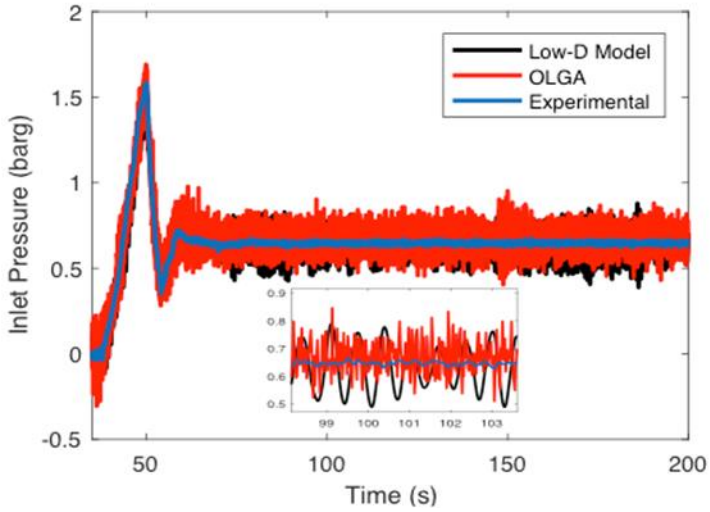

Figure 2-10: Experimental vs. Simulations (Liquid/Case 2)

Note that the amplitude of oscillation decreases from Case 1 to Cases 2 and 3. This can be explained by a higher turbulent flow energy loss due to the increase of the liquid flow rate. Also, similarly to Case 1, both the Low-D model and the OLGA simulations predicted higher frequency oscillation and overshoot. Upon further investigation of Cases 1-3, the air velocity sensors are recording low flow rates,

suggesting the presence of entrapped air in the system. The presence of entrained air in the pipeline results in a significant increase in the fluid compressibility.

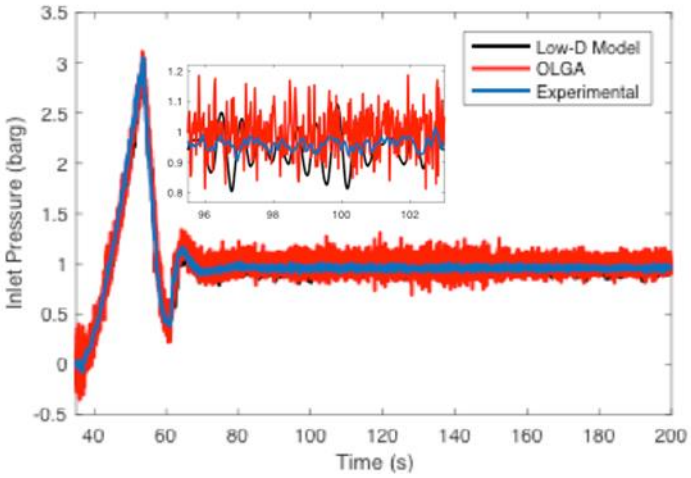

Figure 2-11: Experimental vs. Simulations (Liquid/Case 3)

The entrained air is modeled by altering the fluid equivalent bulk modulus. Two models are presented in the literature to account for the effect of the entrained air on the fluid bulk modulus. In [48] it was proposed that

$$\beta_{eq} = \beta_L \frac{1 + r_v}{1 + \left(\frac{P_0}{P_{avg}}\right)^{\frac{1}{k}} r_v \frac{\beta_L}{kP}}, \qquad r_v \equiv \frac{V_{G_0}}{V_{L_0}}, \tag{2-13}$$

where β_L is the liquid bulk modulus without entrained air, V_{G0} is the entrained air average superficial velocity in the liquid at atmospheric pressure, V_{L0} is the average liquid velocity at atmospheric pressure, P_0 is the atmospheric pressure, P_{avg} is the fluid average pressure, and k is the isentropic exponent (normally, k=1.4).

In [22], the equivalent bulk modulus of a two-phase flow mixture was characterized as a function of the GVF level. The same equation can be adopted to account for the effect of entrained air (very low GVF) on the equivalent bulk modulus.

The pipeline compliance also affects the fluid compressibility [48] as

$$\beta' = \beta \frac{1}{1 + \frac{\beta}{\beta_P}\gamma}, \tag{2-14}$$

where β_P is the bulk modulus of the pipeline and γ is given by

$$\begin{aligned} \gamma &= \frac{2\left(\frac{OD}{ID}\right)^2 (1+\upsilon) + 3(1-2\upsilon)}{\left(\frac{OD}{ID}\right)^2 - 1}, \quad if \ \frac{t}{OD} > 0.1 \quad (thick\ walls) \\ \gamma &= \frac{ID}{t}, \qquad\qquad\qquad if \ \frac{t}{OD} < 0.1 \quad (thin\ walls), \end{aligned} \tag{2-15}$$

where OD is the outer pipe diameter, ID is the inner pipe diameter, υ is the Poisson's number (0.3 for steel) and t is the pipe wall thickness. Shown in Figure 2-12 is the water equivalent bulk modulus as a function of the GVF level (up to 2%) using Model 1 evaluated based on (2-14) and Model 2 (equivalent bulk modulus present in (2-1)).

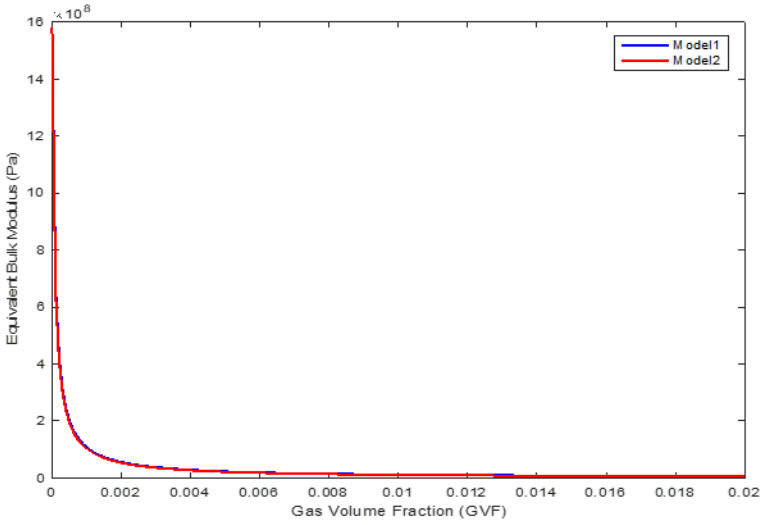

Figure 2-12: Equivalent Fluid Bulk Modulus

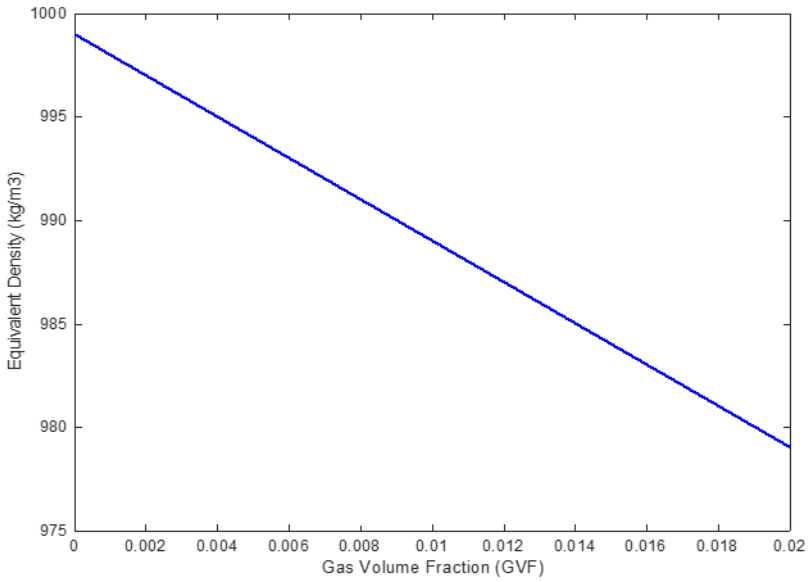

Figure 2-13: Equivalent Fluid Density

The agreement between the two models in estimating the effect of entrained air on the water bulk modulus is noticed. Both models predict a decrease in the bulk modulus as the first air bubbles are introduced which results in an important increase of the fluid compressibility. The entrained air will also affect the fluid equivalent density as shown in [22]. Shown in Figure 2-13 is the equivalent density as function of the GVF level.

The experimental average air and water superficial velocities measured in the flow loop are used to calculate the GVF. The updated equivalent fluid parameters are used as model inputs for the Low-D model for Cases 1-3 (Table 2-3).

Table 2-3: Equivalent Fluid Properties

Case No.	**GVF**	**Equivalent Bulk Modulus (Pa)**	**Equivalent Density (kg/m^3)**
1	0.015	7.12e6	983.55
2	0.016	6.85e6	982.94
3	0.014	7.57e6	984.48

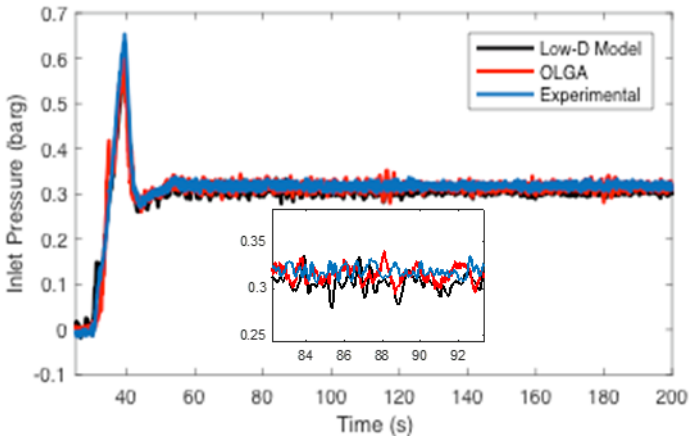

Figure 2-14: Experimental vs. Simulations (Liquid with Entrained Air/Case 1)

In the OLGA simulator, an air feed corresponding to the average air velocity is introduced at the pipeline inlet to account for the entrained air. Figure 2-14-Figure 2-16 are comparisons between the experimental data and model estimations assuming the presence of entrained air. The introduction of entrained air in the system results in lower natural frequencies and higher damping ratios. This translates to time domain predictions better matching of the oscillation frequency and the overshoot when compared to the experimental dataset.

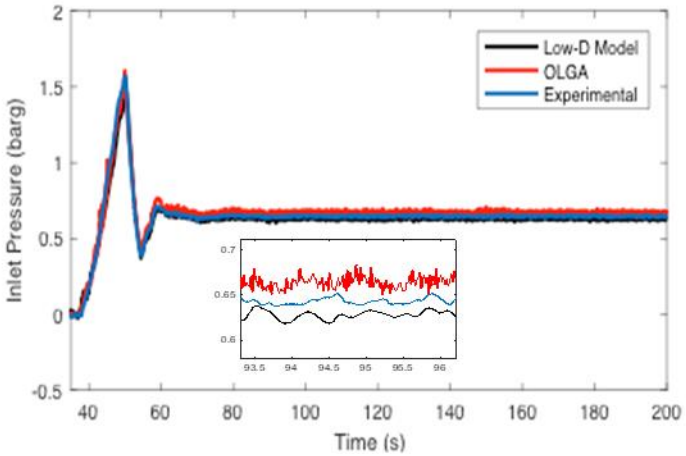

Figure 2-15: Experimental vs. Simulations (Liquid with Entrained Air/Case 2)

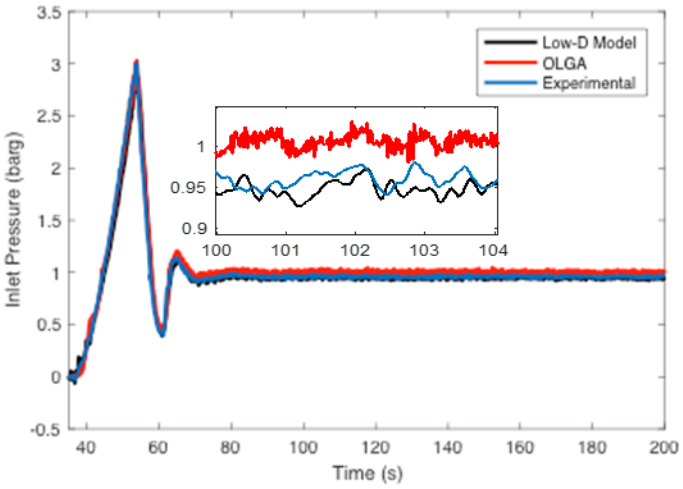

Figure 2-16: Experimental vs. Simulations (Liquid with Entrained Air/Case 3)

2.4.2.3 Effect of GVF on the Pipeline Dynamic Response

The water pump and the air compressors control the superficial velocities achieving GVF levels between 10% and 90%. The measured liquid and air inlet superficial velocities at actual conditions and the outlet pressure are used as inputs for the Low-D model. In the other hand, OLGA simulations require the inputs to be present at standard conditions.

Shown in Figure 2-17–Figure 2-25 are the measured and predicted inlet pressures for the cases of a GVF range from 10% to 90%. Comparing the 10% GVF case (Figure 2-17) to the low GVF dataset (GVF close to 0%) (Figure 2-14-Figure 2-16), the inlet transient pressure response is characterized by a smaller transient overshoot caused by higher viscous damping and a decrease in the fluid speed of sound. This feature was captured by the Low-D model and the OLGA simulation. Both OLGA and Low-D model predictions demonstrated agreement with the experimental dataset within a MAPE of 5%. There are noticeable differences in terms of the overshoot transients

and the settling time. These differences are attributed to the calculated damping ratio as supported in [22].

To evaluate and compare the overall prediction accuracy of the models, the MAPE with respect to the experimental dataset is provided for GVF levels varying from 10% to 90% (Table 2-4). Note that only the pressure transients are considered for accuracy assessment.

Table 2-4: Low-D Model and OLGA MAPE Comparison

GVF (%)	**MAPE (%)**	
	Low-D Model	**OLGA**
10	1.96	2.82
20	3.43	4.25
30	2.91	3.41
40	2.60	3.01
50	3.32	3.82
60	2.12	1.60
70	1.87	1.91
80	1.72	1.79
90	1.63	1.65

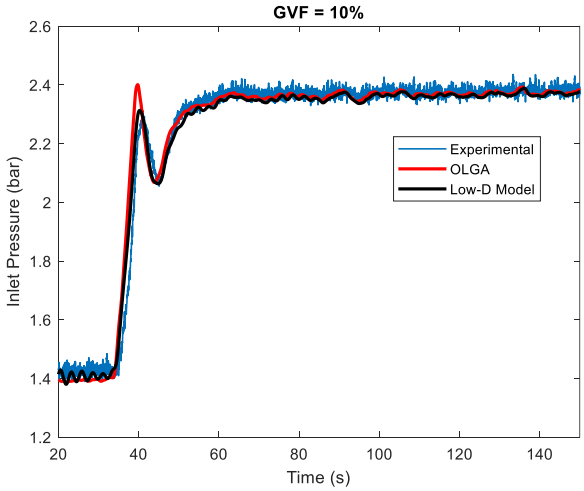

Figure 2-17: Pipeline Dynamic Response Evaluation (10% GVF, Slug Flow)

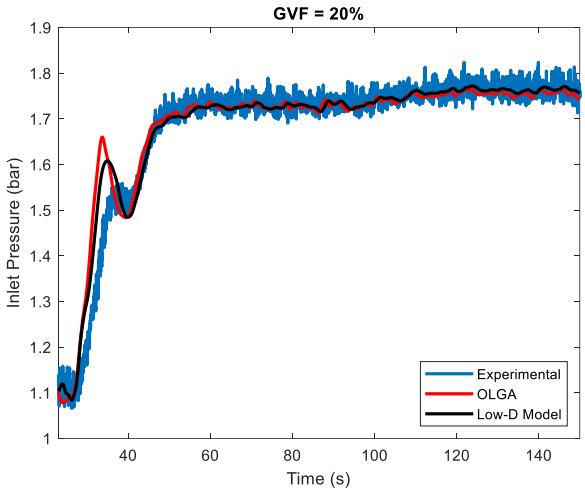

Figure 2-18: Pipeline Dynamic Response Evaluation (20% GVF, Slug Flow)

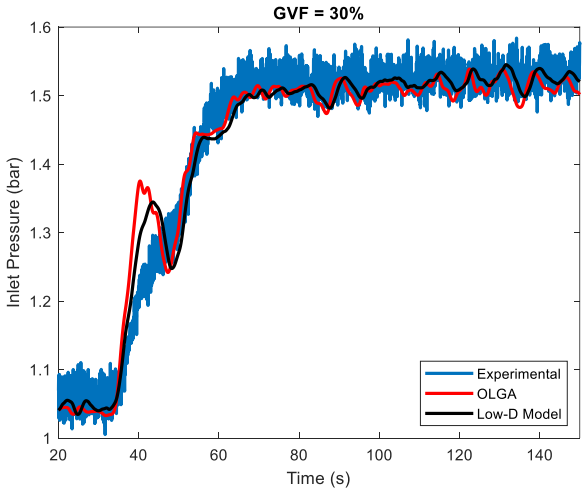

Figure 2-19:Pipeline Dynamic Response Evaluation (30% GVF, Slug Flow)

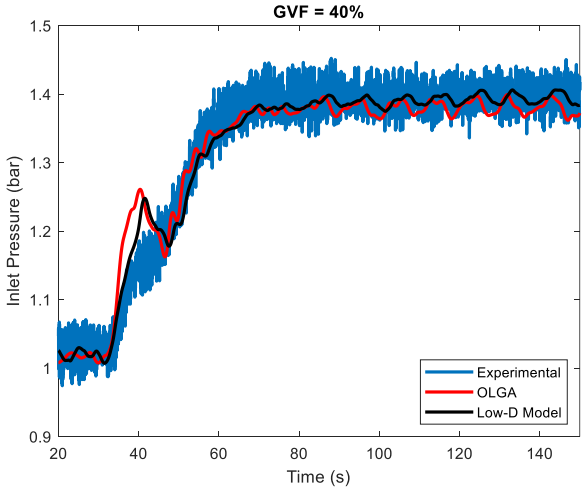

Figure 2-20:Pipeline Dynamic Response Evaluation (40% GVF, Slug Flow)

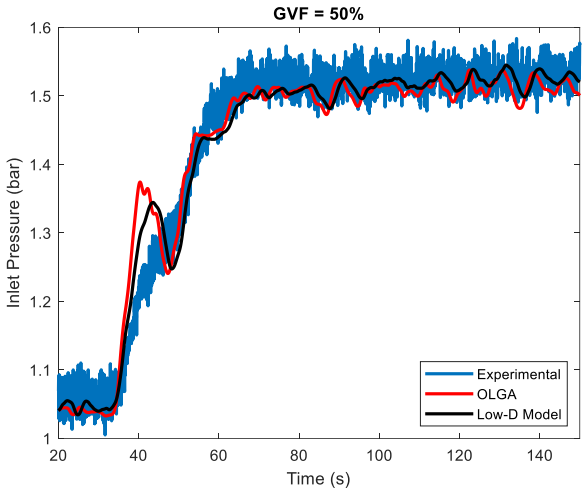

Figure 2-21:Pipeline Dynamic Response Evaluation (50% GVF, Slug Flow)

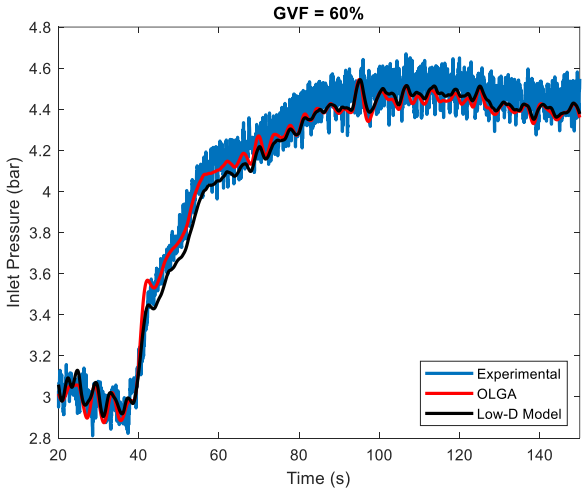

Figure 2-22:Pipeline Dynamic Response Evaluation (60% GVF, Slug Flow)

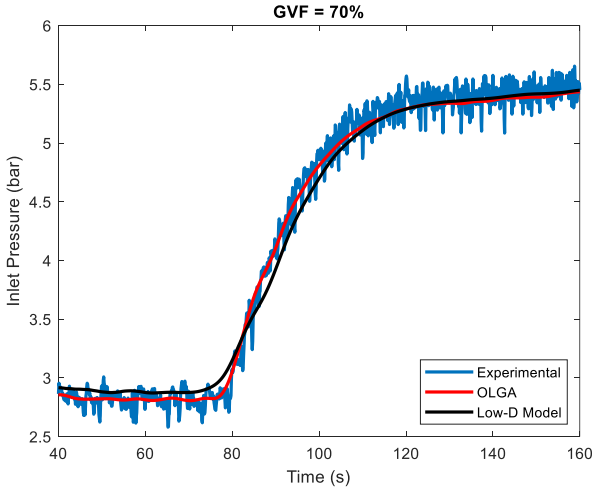

Figure 2-23:Pipeline Dynamic Response Evaluation (70% GVF, Froth Flow)

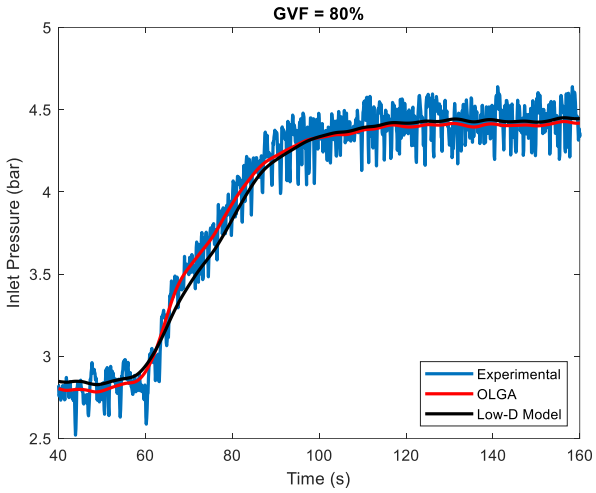

Figure 2-24:Pipeline Dynamic Response Evaluation (80% GVF, Froth Flow)

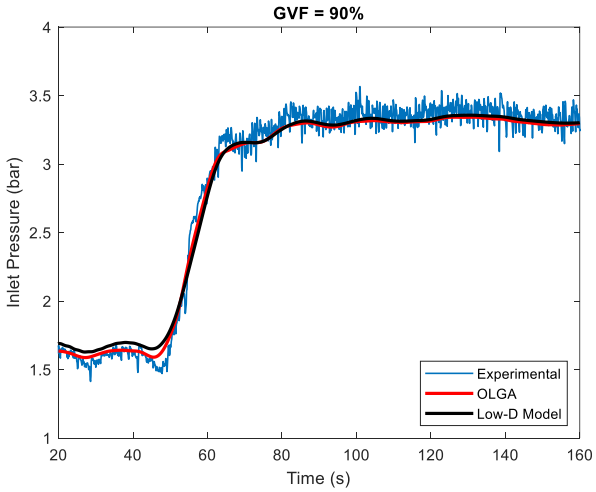

Figure 2-25:Pipeline Dynamic Response Evaluation (90% GVF, Froth Flow)

2.4.2.4 Discussion

As a higher GVF level is imposed inside the pipeline, the time-averaged pressure drop varies due to the transition between different two-phase flow patterns, the interaction between phases and the friction losses effect. This phenomenon was equally captured by the Low-D and the OLGA models. Increasing the GVF results also in an overdamped system for the presented dataset. It has been noticed that the Low-D model gives for most of the experimental validation cases a better estimation of the system's

overshoot when compared to the OLGA simulation. The accuracy of the OLGA simulator improves considerably for the higher-pressure dataset while the Low-D model is characterized by a relatively constant performance. This may be explained by the fact that the closure relationships used in the OLGA model are mostly calibrated using oil and gas high-pressure field data.

Certain assumptions were applied in the presented study. The data presented and discussed in this paper are characterized by low-pressure levels (less than 6 bar) due to the equipment limitations and safety consideration of the NUS Multiphase Flow Loop (maximum pressure rated at 13 barg) whereas the pressure can exceed 500 bars for the case of high-pressure oil and gas production. Similarly, all the tests were performed at temperatures near standard conditions while multiphase flow production fluids can undergo considerable temperature variations especially in the subsea environment. The results were also limited to air-water mixtures. To capture the effect of the pressure, temperature and fluids properties variations on the pipeline dynamic response, the fluid properties are updated for each pressure and temperature condition using a (pressure/volume/temperature) PVT file. The use of physics-based relationships in both the Low-D and OLGA models will also ensure a reduced sensitivity to the operating conditions when compared to purely empirical models since these relationships are not correlated to a specific dataset and analysis can be achieved when investigating different operating ranges. Hence, the conclusions drawn from the comparison between the experimental data and the mathematical models should remain valid at different pressure and temperature conditions or fluids. To validate this assumption, the discussed models should be compared not only to experimental test results but also to field data.

In Figure 2-18, for the case of 20 % GVF, significant slugging is observed in the test section, indicated by the sudden increase of the water flow rate and inlet pressure. This phenomenon is created by the accumulation of water at the bend upstream of the test section before being suddenly pushed by the air pressure. Hydrodynamic slugging is caused by the gas phase flowing at high velocities rate over a slow-moving liquid phase. This results in waves that form on the liquid surface that grow to bridge the entire cross-section of the pipe. Compared to terrain slugging, hydrodynamic slugging is characterized by higher frequency and lower amplitude pressure oscillations. While the terrain slugging is present in the simulated pressure by both models, the hydrodynamic behavior of slug flow is not captured as the Low-D and OLGA models only capture the area-averaged pressure seen by the pipeline. The OLGA Slug Tracking module, an additional extension for the OLGA multiphase flow model, can be enabled to track the hydrodynamic slugging behavior.

As shown in Figure 2-26, a slug flow unit can be defined as a succession of a slug film (stratified or annular flow) and a slug body (dispersed bubble flow).

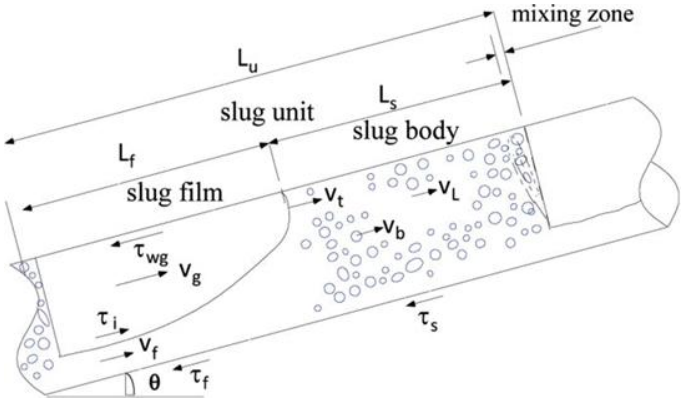

Figure 2-26: Slug Flow Unit Schematic [50]

Like OLGA, a hydrodynamic slug-tracking module can be incorporated to the Low-D model as a future study, especially when extending the present work to cover inclined multiphase flows as well. This module will consider the slug flow structure and its effect on the pipeline's dynamic response. First, the length of the slug film L_f, length of the slug buddy L_s, the liquid holdup distribution and the slug unit frequency are estimated. This will enable the derivation of a relationship between the slug flow structure parameters and the pipeline and fluids physical properties. The resulting slug flow structure estimations are then used as scheduling parameters to switch between a stratified flow model (slug film) and a dispersed-bubble flow model (slug body). This procedure enables the estimation of the pressure fluctuation due to the succession of slug units. The additional slug transient module can be easily disabled if only the average pressure is of interest.

To validate the proposed slug-tracking model, additional transient data will be collected at the NUS flow loop to evaluate the model accuracy in predicting the slug flow structure parameters and the pipeline dynamic response for two-phase slug flows and/or inclined pipeline configuration.

2.5 Conclusion

The transient behavior of air-water two-phase flow mixtures in horizontal pipelines was studied through experimental data and mathematical models. The experimental data was collected from the National University of Singapore Multiphase Flow Loop, a facility that offers a modular structure enabling the study the different GVF levels and flow regimes encountered in the oil and gas production.

The comparison between the experimental data with low pressure and the Low-D model predictions permitted to quantify the effect of the number of modes on the Low-D model accuracy and the simulation time. As expected, increasing the model order (number of modes) results in an improved accuracy but will require a longer computation time. A tradeoff between accuracy and simulation time is therefore suggested by the modeling environment depending on the required accuracy and available computational power. The analysis of the single-phase flow experimental dataset established the existence of entrained or entrapped air in the system due to the action of the water pump. It has been shown that the presence of entrained air in the pipeline results in a significantly lower speed of sound of the fluid leading to a considerable increase in the pipeline damping and a decrease in the natural frequency.

The Low-D model pressure predictions and the OLGA simulations were compared to the measured transient pressure for different GVF levels. Both models showed a good agreement with the experimental data with a Mean Absolute Percent error lower to 5%. While the Low-D model is characterized with a relatively constant performance for different pressure conditions, the OLGA model accuracy improved for higher-pressure conditions. Considering this level of accuracy and taking into account the difference between the OLGA multiphase flow model and the Low-D model in term of computational requirements, the proposed Low-D model can be deployed to achieve real-time tasks varying from production monitoring, prediction of pressure and flow rate along pipelines, instantaneous flow pattern tracking as well as coupling with flow assurance models for pipelines integrity management analysis.

As future step, field data will be collected, aiming at evaluating the effect of the fluid properties, pressure, and temperature variations on the model's accuracy. A slug-tracking module is also suggested for the Low-D model to simulate the hydrodynamic slugging conditions.

3 DATA-DRIVEN MODELING OF CARBON DIOXIDE (CO_2) CORROSION FOR PIPELINES INTEGRITY MANAGEMENT APPLICATION

3.1 Introduction

A major concern in the oil and gas industry is the ability to design an environmentally safe and a reliable production system carrying organic fluids. The carbon dioxide (CO_2) corrosion associated with oil and gas production systems is a major factor limiting both reliability and service life. Consider the design of a subsea architecture comprised of transmission lines, manifolds, trees, jumpers, compressors, and multiphase pumps. Accurately quantifying the CO_2 corrosion rate provides a reliable estimation that can be used during the design phase to specify material and dimension selections while enabling real-time subsea architecture health monitoring. Regulatory requirements in standards such as ASME's Managing System Integrity of Gas Pipelines [51] include corrosion estimates when specifying the pipe/jumper wall sizes, which in turn directly impact the production system CAPEX. Since CO_2 gas is ubiquitous during the oil and gas extraction process, there is a need to mathematically quantify its interaction with the transmission line and other subsystems.

Carbon dioxide corrosion is a complex multi-physics process that is dependent on the multiphase flow regime and patterns (separate flow, mixed flow, continuous and dispersed flow). Each flow regime has a unique surface wetting mechanism that strongly affects the corrosion process in the absence of protective scaling. Multiphase flow can lead fluctuating mass transfer rates (particularly in slug flow), which in turn, affects the corrosion rate.

Presented herein is a mathematical model predicting the CO_2 corrosion rate. This chapter begins with a review of the CO_2 corrosion models investigated to develop the proposed model. Then, a parameter-varying (PV) model quantifying the CO_2 corrosion rate is developed by modifying the corrosion rate model provided in [52] to have parameter varying coefficients. Validation of the proposed model and a discussion are also given in this section. The chapter concludes with summary of the model and conclusions.

3.2 CO_2 Corrosion Rate Modeling Review

Internal corrosion of oil and gas pipelines made from carbon steel is a complex process involving a variety of corrosive species that interact and evolve following different physical-chemical mechanisms. The electrochemical CO_2 corrosion process of carbon steel involves chemical equilibriums relating an anodic dissolution of the CO_2 along with its carbonate derivatives, and a cathodic evolution of hydrogen [53]. Many studies and experiments have been conducted to analyze the process of CO_2 corrosion [54-56]. This allowed the researchers to investigate the effect of a variety of parameters on the corrosion process. Based on this work, certain parameters have been categorized as the major factors impacting the electrochemical exchange occurring during the CO_2 corrosion process. Namely these variables have been identified as: temperature, pH, flow velocity and the partial pressure of CO_2.

Fundamental investigations focusing on corrosion rate predictive models for mild steel in the presence of CO_2 aqueous environment have been conducted since the 1970s. Numerous mathematical representations describing this process have been developed

providing a knowledgebase of models. These models can be categorized into three major groups: Empirical models that are independent from the physical and electrochemical background underlying this process, Hybrid models that are partially related to the theoretical fundamentals of the process, and Mechanistic models that seek to properly describe the electrochemical exchange describing the CO_2 corrosion in oil and gas systems [53].

The distinction among these categories is based on the strategy used to identify the model. Mathematical models based on the physics/chemistry governing the CO_2 corrosion process are mechanistic models. This class of corrosion rate models eliminates the need for interpolation since each model is an explicit function of fluid/metal properties. There is modularity that enables model evolution as new discoveries in CO_2 corrosion arise. The second category, empirical models, involves mathematical functions that best approximate the causalities among experimental data, independent of process physics. Hybrid models are a combination of the previous two categories fusing both mechanistic and empirical models into one model. A summary of models associated with each category is presented herein.

3.2.1 CO_2 Corrosion Rate Mechanistic Models

The class of mechanistic CO_2 corrosion rate models is built upon the electrochemical reactions present during the CO_2 process. Subsequent investigations produced more complete electrochemical models that better capture the reactions behind this phenomenon. These models were based on the method of determining the corrosion rate from the anodic current by starting from the exchange current density

determination and the charge transfer rate calculation. One such model was proposed by [54]. This model considered the electrochemical aspects of the carbon dioxide corrosion process in aqueous environment based on the charge transfer rate calculations and is based on the direct carbonic acid reduction mechanism used by [55]. To predict the CO_2 corrosion rate, charge transfer calculations and mass transfer limitations with respect to glass cell experiments were employed within a flow cell experiments enabled model calibration. The authors extended the model to conditions where higher temperature and pH values are present. This illuminated the theoretical shortcomings of the model due to the omissions of several additional processes that interact with the corrosion process such as scale formation.

Authors in [57] also developed an electrochemical model of carbon dioxide corrosion process for pipeline applications. This model focused on the physical and chemical reactions interacting during this process. Several parameters introduced into the model were determined from a rotating cylinder glass cell experiment and the straight pipe flow experiment. The results were successfully compared to the results given by experiments conducted by [54].

The electrochemical corrosion models in [54] and [57] have been widely used in industry offering a simple physical-chemical approach to quantify the corrosion process. The uncertainty associated with these models is due to the description of the transport phenomenon of species moving from bulk solution to the metal surface. However, the assumed independency between these species gave unreliable prediction of results especially when extending the results to species adsorption and protective film formation on the metal surface.

To reduce corrosion rate estimation uncertainty, additional models have been proposed that capture the electrochemical fundamentals of the carbon dioxide corroding process of mild steel in aqueous solutions. These models were developed to improve the corrosion rate estimation by incorporating the chemical reactions of different species present during this process. Since the carbon dioxide corrosion process on the metal surface involves several reactions, species are produced at the steel surface while others are depleted. This creates concentration gradients of diffusion of these species between the surface and the solution.

Authors in [58] proposed a new mathematical model based on the solution of Nernst-Planck equation. This model included the mass conservation of species during their transport processes in the boundary diffusion layer. It accounts for the concentrations of the different species traveling between the bulk solution and the metal surface. This proposition was improved by [59] who presented a model using the correlation of the eddy diffusivity defined in [60] and incorporating the convective mass transfer and the Tafel equation to calculate the charge transfer rate. Authors in [61] as well as in [56] expanded the work by ameliorating the charge transfer rate calculation by using the Tafel equation. This inclusion described the transfer kinetics while replacing the exchange current densities in the bulk solution by surface concentrations.

Mechanistic CO_2 corrosion models could be sufficient for corrosion rate estimation and have demonstrated utility by depicting a more detailed description of the processes involved in corrosion of steel in CO_2 environments. These models have a proven utility in the fundamental investigations of corrosion mechanisms and a window

into more complex systems involving new processes (H_2S corrosion, pitting corrosion, etc.).

3.2.2 CO_2 Corrosion Rate Empirical Models

The class of empirical models is less dependent on the electrochemical underpinnings of the corrosion process. The main expressions that comprise these models are usually chosen iteratively and used to extrapolate the results for a wider range of experimental database with limited results. An attempt to include additional experimental results could alter the model structure significantly; hence, correction factors are used. One well known empirical model for CO_2 corrosion rate prediction is the NORSOK model [62] given by (3-1). It has been widely used as a free open standard model for corrosion estimation. This standard is based on the semi-empirical corrosion model developed by [52] that was used the same experimental database as the model of [55]. The NORSOK model is founded on a basic temperature dependent function multiplied by several correction factors describing the effect of the partial pressure of carbon dioxide, the pH, the flow velocity, the steel composition and essentially the protective scale formation. The NORSOK corrosion rate is then expressed as

$$CR_{NOR} = K_t f_{CO_2}^{0.62} \left(\frac{S}{19}\right)^{0.146+0.0324\, log_{10}(f_{CO_2})} f(pH), \tag{3-1}$$

where K_t is the NORSOK temperature constant, S is the shear stress, f_{CO_2} is the fugacity of CO_2 and $f(pH)$ is a pH dependent function.

3.2.3 CO_2 Corrosion Rate Hybrid Models

The class of hybrid CO_2 corrosion rate models is dependent on both the electrochemical corrosion fundamentals and experimental data. These models are mainly employed when the knowledgebase of CO_2 corrosion is insufficient. While these models retain a structure founded upon a theoretical basis, some of model parameters are identified using data analytic techniques. As is the case for empirical models, adding additional model regressors requires complete model recalibration or additional correction factors. One of the pioneering hybrid corrosion models was developed by [63]. This model estimates the corrosion rate based on the CO_2 partial pressure and the temperature under the assumption that the iron dissolution is governed by the Bockris, Drazic and Despic (BDD) mechanism [64]. The corrosion rate is obtained as a function of the temperature and the partial pressure of carbon dioxide, namely

$$log_{10}(CR) = 7.96 - \frac{2320}{T} - 5.5 \times 10^{-3} \times T + 0.67 \times log_{10}(P_{CO_2}), \tag{3-2}$$

where T is the fluid temperature and P_{CO_2} is the CO_2 partial pressure.

Modifications to (3-2) have been proposed that led to the introduction of correction factors accounting for the different phenomenon interfering with the carbon dioxide corrosion process [52, 55, 65]. The CO_2 corrosion model presented by [55] is given

$$log_{10}(CR) = 5.8 - \frac{1710}{T} + 0.67 \times log_{10}(f_{CO_2}), \tag{3-3}$$

where f_{CO_2} is the fugacity of the carbon dioxide, calculated as a function of the fugacity coefficient of carbon dioxide a when considering the case of a non-ideal gas

$$f_{CO_2} = a \times P_{CO_2}. \tag{3-4}$$

This model was recalibrated using correction factors that describe the different interactions among the carbon dioxide corrosion process. Specifically, a correction factor including the impact of the protective film of $FeCO_3$ on the corrosion rate was introduced. This additional parameter was added depending on the range of operating temperature by giving an estimation of temperature when this protective film starts to form, expressed as

$$T_{Scale} = \frac{2400}{6.7 + 0.67 \times log_{10}(f_{CO_2})}. \tag{3-5}$$

At this temperature, the corrosion rate reaches its peak values and then starts to decrease because of the formation of a protective layer on the surface of the metal. The resulting corrosion rate by a scale factor F_{scale} is

$$\log_{10}(\mathrm{F_{Scale}}) = \begin{cases} 2400 \times \left(\frac{1}{\mathrm{T}} - \frac{1}{\mathrm{T_{Scale}}}\right) & , \mathrm{T} > \mathrm{T_{Scale}} \\ 0 & , \mathrm{T} \leq \mathrm{T_{Scale}} \end{cases}. \tag{3-6}$$

These modifications broadened the extension of the results with respect to the effect of the scale formation on the metal surface. The effects of high pH formation water and wetting factor makes this model as one of the most important standards used for CO_2 corrosion modelling and prediction in industry.

Another improvement, made to the basic model in [55], was presented by [52] to capture the effect of the flow velocity in the absence of protective scales formation. This proposed model was introduced as a parallel resistance model given as

$$\frac{1}{CR} = \frac{1}{CR_r} + \frac{1}{CR_m}, \tag{3-7}$$

$$log_{10}(CR_r) = 4.93 - \frac{1119}{T} + 0.58 \times log_{10}(f_{CO_2}), \tag{3-8}$$

and

$$CR_m = 2.45 \times \frac{V_m^{0.8}}{d^{0.2}} \times f_{CO_2}. \tag{3-9}$$

CR_r is the representative of the contribution of the activation reaction kinetics and CR_m is the contribution from the mass transfer kinetics due to the flow velocity. This new model proposed by [52] was an improvement to the standard model in [55], especially, when adding the effect of the flow velocity. However, it remains a hybrid model where the constants are calibrated using limited field data.

Choosing the appropriate model for corrosion rates estimation will depend on the available variables to perform corrosion prediction of an oil and gas system. A summary of the different models described and the required inputs for each model is presented in Table 3-1.

Table 3-1: Models Inputs

Input	DLM	DLD	NOR	NPO	Description
T (°K)	X	X	X	X	Temperature
f_{CO_2} (bar)	X	X	X	X	CO_2 fugacity
D (m)		X		X	Pipe diameter
ρ (kg/m^3)				X	Water density
μ (kg/m.s)				X	Water viscosity
V (m/s)		X		X	Fluid velocity
S (Pa)			X		Wall shear stress
pH			X	X	pH

3.3 Parameter Varying CO_2 Corrosion Rate Modeling

Presented in this section is the development of a parameter varying (PV) model predicting CO_2 corrosion rate in metal alloys. The model identification process is performed in three stages. The first stage involves a comparative study among the models previously presented. The model with the lowest residuals (i.e., prediction error)

is selected as the model to be modified. The modification is based on developing a mathematical relationship between the residuals and the solution variables.

3.3.1 Comparative Study of Selected CO_2 Corrosion Models

The dataset used to perform the comparative study is the CO_2 corrosion rate data provided in [66] experiments and [57]. The corrosion rate values in [66] were measured by performing a parametric investigation on the CO_2 corrosion process of a ferritic-pearlitic carbon steel St-52. The experiments were performed on a low-pressure high-flow velocity test loop with a 0.1m internal diameter. The experimental data from [57] involved a parametric investigation of CO_2 corrosion on carbon steel X-65 and covered higher values of pH. This experiment had been performed on a testing flow loop with a 0.015m internal diameter. Both experimental investigations were performed using a water phase flow condensed with CO_2. The water chemistry was strictly controlled and the assumption of no protective film present on the metal surface was considered. Table 3-2 presents a description of the range of experimental conditions.

Table 3-2: Experimental Dataset Description

Temperature (°C)	20 – 90
pH	3.4 - 6
Flow velocity (m/s)	0.1 - 13.0
CO_2 partial pressure (bar)	0.4 – 21.0

Data from these two sets were concatenated into one dataset containing 80 data points that was divided into two groups. The first group, a calibration group of 69 data points, is used for the calibration and the identification process of the functional relationship for the model coefficients necessary to improve prediction accuracy. The second group, a validation group of 11 data points, is used to validate the parameter

varying model coefficients. The three models compared are [55], [52] and [62]. The objective was to select the model presenting the closest prediction results to the measured corrosion rates given in [57, 66].

Presented in Table 3-3 is a summary of the model prediction performance comparison for the recalibrated models. The model presented in [52] has a slightly better accuracy over the other two models. The model developed in [52] has a correlation coefficient R-squared value of 0.54 and a mean-absolute error value of 6.99 as compared to 0.43 and 8.19 for the model in [55] and 0.54 and 7.66 for the NORSOK model [62]. Based on the results of this comparison, the DeWaard-Lotz-Dugstad (DLD) model [52] was selected as a base structure to be modified using PV coefficients.

Table 3-3: Data-Based Models Performances Comparison Results

Model	Mean Absolute Error	R-Squared
DeWaard-Lotz-Milliams (1991)	8.19	0.43
DeWaard-Lotz-Dugstad (1995)	6.99	0.54
NORSOK Standard (2005)	7.66	0.54

3.3.2 Parameter Varying DLD CO_2 Corrosion Rate Model

The DeWaard-Lotz-Dugstad model [52] was originally developed as a parallel resistance model presented in (3-7). This model has been developed by introducing two independent parameters to capture the different factors contributing to the corrosion process. The model was formed in two parts: kinetics related term (3-8) and mass transfer related term (3-9). The kinetics related term in (3-8) is a function of the temperature and the partial pressure of the carbon dioxide defining the electrochemical reaction rate contribution to the corrosion process. The mass transfer term in (3-9)

describes the effect of the mass transfer process on the corrosion rate values. The proposed structure for the PV CO_2 corrosion model is given by

$$\frac{1}{CR_{Recalibrated}} = \frac{1}{CR_r^*} + \frac{1}{CR_m}, \tag{3-10}$$

where $CR_{Recalibrated}$ is the recalibrated corrosion rate, CR_r^* is the modified reaction kinetics dependent term and CR_m is the mass transfer kinetics dependent term.

With previous experimental conditions involving a condensed aqueous environment, the effect of pH was not included on the DeWaard-Lotz-Dugstad model. However, both variables play an important role affecting the electrochemical reactions taking place during the corrosion process. The pH value will enhance, in the presence of favorable conditions, the process of super-saturation of the species, which lead to the formation of protective films. On the other hand, the flow directly affects the species diffusion process between bulk solution and the metal surface [53]. Hence, to make these two parameters explicitly present, it is proposed within this section to mathematically introduce the effects of pH and flow velocity by replacing the constant coefficients in (3-8) with coefficients that are a function of pH and velocity.

3.3.2.1 Parameter Varying Coefficients Identification

Presented is the identification of parameter varying coefficients for (3-8). These modifications will produce the model

$$log_{10}(CR_r^*) = a_1 \times \frac{1}{T} + a_2 \times log_{10}(f_{CO_2}) + a_3, \tag{3-11}$$

in which the coefficients a_1, a_2 and a_3 denote mathematical functions involving solution parameters. The process is comprised of the following steps:

Step 1: Recalibration of the DLD Model: Calibrate the constant coefficient model in (3-11) by concatenating the datasets provided in [57] and [66].

In order to be incorporated into the calibration process, the modified parallel resistance model in (3-10), where the new kinetics related term presented in (3-11) has been integrated to calculate the recalibrated corrosion rate $CR_{Recalibrated}$, can be rewritten as

$$CR_{Recalibrated} = \frac{CR_r^* \times CR_m}{CR_r^* + CR_m}. \tag{3-12}$$

In this form, a nonlinear least squares method can be used to identify the constant coefficients that minimize the prediction errors defined as

$$\min_{a_1,a_2,a_3 \in \mathbb{R}} (CR_{mes} - CR_{Recalibrated}). \tag{3-13}$$

The resulting recalibrated model in (3-8) based on the structure presented in (3-11) is

$$log_{10}(CR_r^*) = 4.65 - \frac{1119}{T} + 0.18 \times log_{10}(f_{CO_2}). \tag{3-14}$$

Combining the recalibrated kinetics term CR_r^* presented in (3-14) and the mass transfer term presented in (3-9), it is possible to calculate the new corrosion rate values CR from (3-12). The predicted corrosion rates CR are presented in Figure 3-1 to illustrate the comparison between the predicted values and the experimental results.

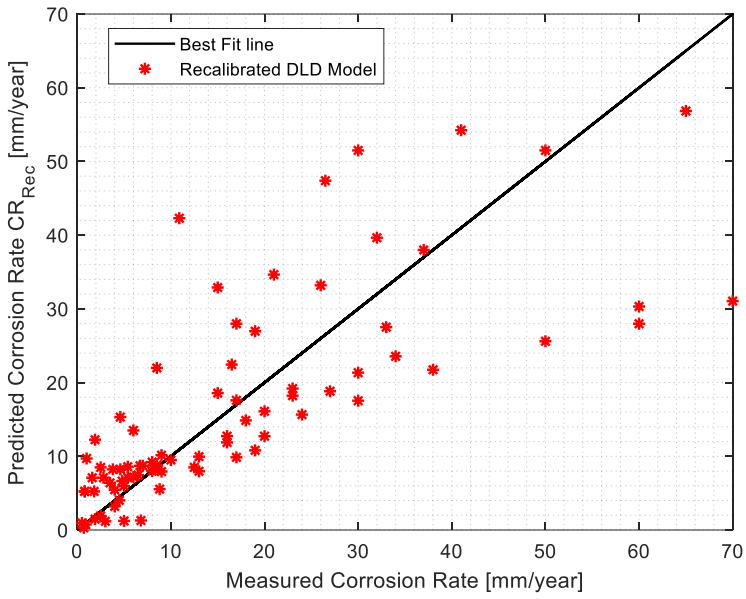

Figure 3-1: Recalibrated DLD Model Results $CR_{Recalibarted}$

Step 2: Parameter Varying Coefficients Identification: Identify and calibrate functions for the coefficients a_1, a_2 and a_3 to minimize estimation residuals.

To be able to perform the parameter varying coefficient identification, a new variable CR_r^{EXP} has been introduced. CR_r^{EXP} represented the kinetics related contribution if we consider that the measured corrosion rate can be written following the same expression in (3-10). Hence, CR_r^{EXP} can be calculated as

$$CR_r^{EXP} = \frac{CR_{mes} \times CR_m}{CR_m - CR_{mes}}. \tag{3-15}$$

Based on the recalibrated kinetics term CR_r^* in (3-14) and the experimental kinetics term CR_r^{EXP} calculated from (3-15), we can define the residual by

$$residual = log_{10}(CR_r^{EXP}) - log_{10}(CR_r^*). \tag{3-16}$$

With the goal of identifying an adequate expression to be included in (3-14), the residuals in (3-16) are plotted against the variables presented in (3-14), namely temperature and carbon dioxide fugacity (Shown in Figure 3-2).

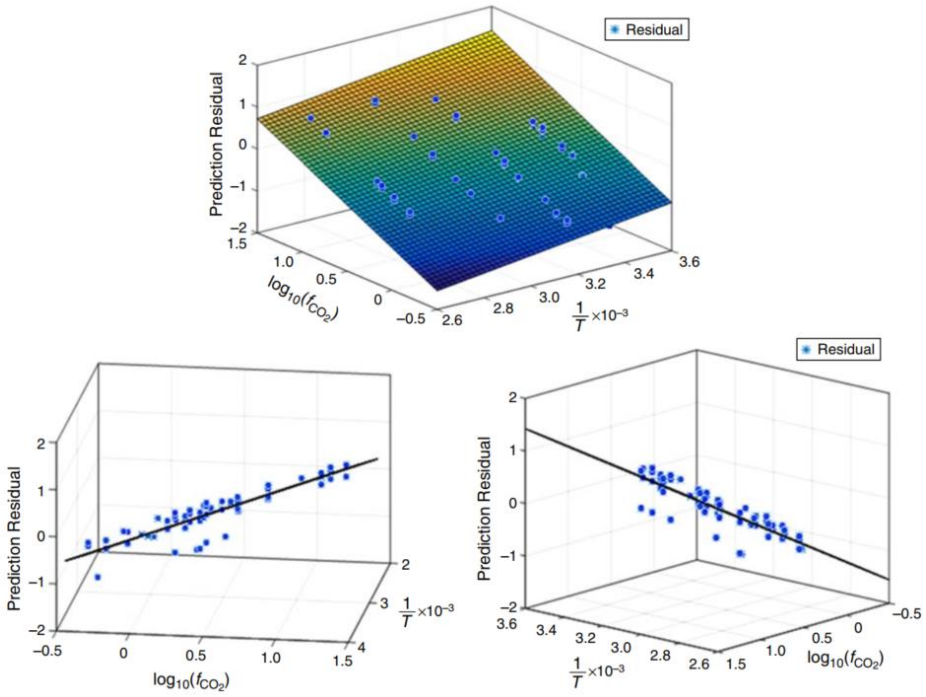

Figure 3-2: Prediction Residuals as a Function of Solution Parameters

Based on the results presented in Figure 3-2, we were able to identify the prediction residuals calculated based on (3-16) as a plane. Therefore, presenting the residual as a correlation that has the same structure as presented in (3-14) would be preferable. Based on this observation, the residual was identified, using linear regression methods, as a parameter-varying model presented by

$$residual = f_1(pH, V_m) \times \frac{1}{T} + f_2(pH, V_m) \times log_{10}(f_{CO_2}) + Bias. \quad (3\text{-}17)$$

The structure of the varying coefficient f_1 and f_2 was identified using the nonlinear optimization process. Based on the results of this process and aiming to have a simple expression, the parameter varying coefficients were identified as

$$f_i(pH, U) = \alpha_1^i + \alpha_2^i \times V_m^{0.5} + \alpha_3^i \times pH^3, \tag{3-18}$$

where the coefficients α_1^i, α_2^i and α_3^i, i = 1,2 are calculated using ordinary least squares estimation. Integrating the residual model in (3-16) with (3-14) gives

$$log_{10}(CR_r^{final}) = log_{10}(CR_r^*) + residual. \tag{3-19}$$

This operation produces the final expression for the activation kinetics CR_r^{final} as

$$\begin{aligned} log_{10}(CR_r^{final}) &= 3.72 - (877.1 - 61.95V_m^{0.5} + 1.57pH^3)\frac{1}{T} \\ &+ (0.98 + 0.008V_m^{0.5} - 0.02pH^3)\, log_{10}(f_{CO_2}). \end{aligned} \tag{3-20}$$

3.3.2.2 Parameter Varying Model Evaluation

The results associated with the parameter varying reaction kinetics term in (3-20) are shown in Figure 3-3. The significant model prediction accuracy offered by (3-20) over the DeWaard-Lotz-Dugstad model [52] can be seen at corrosion rates above 20 mm/yr. It is important to note that the measured corrosion rates at these points occurred under experimental conditions where the pH values are low, and the flow velocity values are high. This observation supports the premise that the variations in corrosion rate driven by these two parameters are needed for accurate corrosion rate predictions.

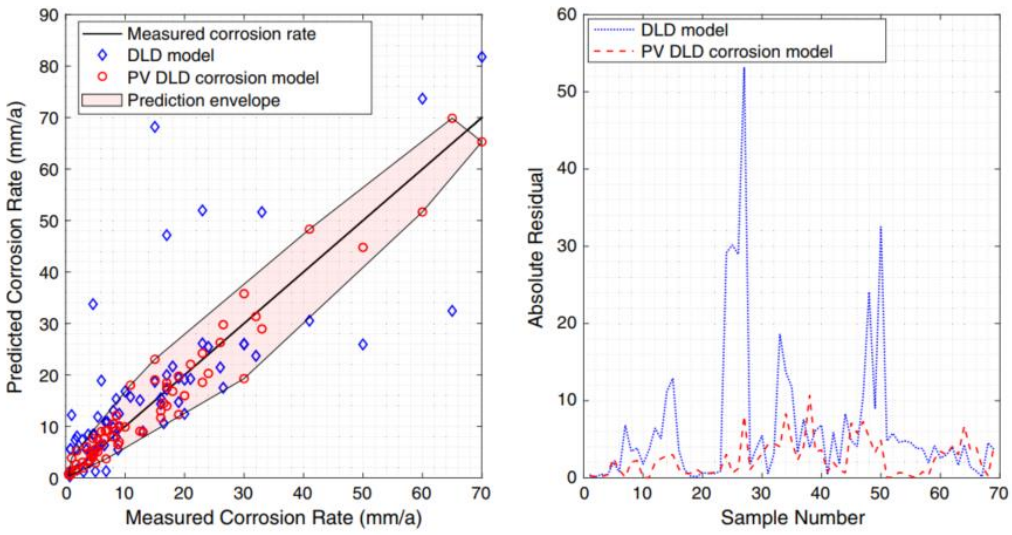

Figure 3-3: PV Corrosion Rate Model Training Results

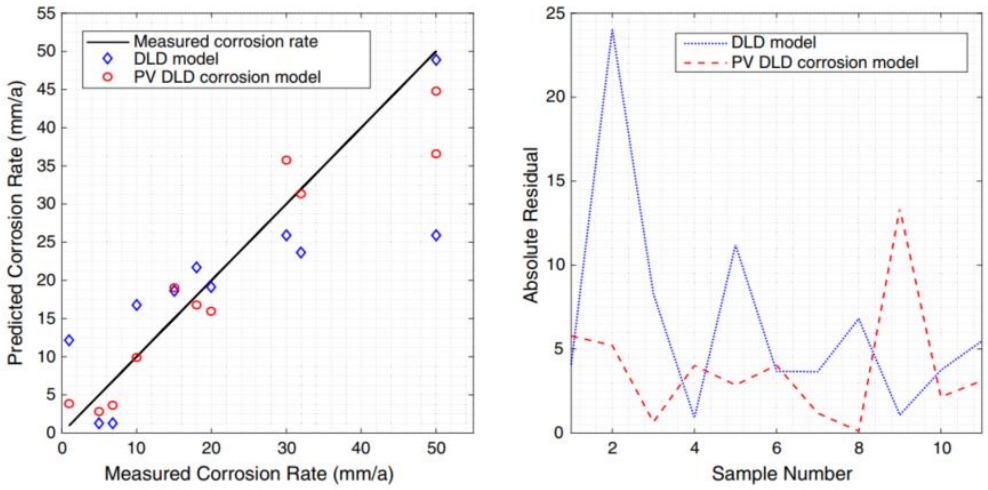

Figure 3-4: PV Corrosion Rate Model Validation Results

Shown in Figure 3-3 and Figure 3-4 is a comparison of the performances of both the new recalibrated model and DeWaard-Lotz-Dugstad model. The present model is predicting more accurate results with a correlation coefficient R-Squared value up to 0.90 compared to 0.54 for the DeWaard-Lotz-Dugstad model [52]. The PV model allows a more complete interpretation of the CO_2 corrosion process by incorporating

the missing variables (pH and flow velocity) to the reaction's kinetics related term of the model. The proposed PV model for CO_2 corrosion prediction has shown very good predictions when compared to other data-based models that presently exist. The prediction results were very close to the experimentally measured corrosion rates and the estimation error was reduced by 80%. This improves accuracy that could be coupled with multiphase flow models to enable precise corrosion rate prediction in oil and gas production and transmission systems.

3.4 Discussion

Data-driven models are mathematical representations of experimental observations developed based on information retrieved from an input-output fidelity (systems) level. This means that mathematical models are not necessarily unique. Thus, predictions outside the dataset input range cannot be inferred nor estimated based on such models. First principles models, on the other hand, can be used for output predictions with a mathematically rigorous quantification of the uncertainty for these predictions.

First principles models, including mechanistic based models, have prediction challenges. Consider the experimental corrosion rates reported in the literature (Table 3-4).

Table 3-4: Experimental Corrosion Rate Uncertainty

T(°C)	P(MPa)	V_m(m/s)	pH	Experimental Corrosion Rate (mm/year)		
				Max Value	Min Value	Average Value
60	0.22	13	3.8	44	32	38
90	0.37	3.1	3.8	17	16	16.5
90	1.4	3.1	3.6	15	6	10.5
90	2.1	3.1	3.5	38	15	26.5

Table 3-4 shows cases where uncertainty is presented in the corrosion rates measured following the experiments performed by [66]. Different corrosion rates values had been recorded for some duplicate testing conditions. Notice the significant differences observed for similar experimental conditions. These differences are mainly due to high temperatures, high velocities and/or low pH, all of which represent favorable conditions enhancing high corrosion rates. For the models presented in this work, the average corrosion rates were used.

To show the effect of the differences among the dataset on the modelling process output, the duplicate testing conditions were eliminated, and three different datasets were constructed: Average corrosion rates for each testing condition, Minimum corrosion rates, and Maximum corrosion rates.

The same calibration process had been performed using each of the three datasets. Shown in Figure 3-5 are the least square linear fits for the prediction results using each of the three datasets mentioned above.

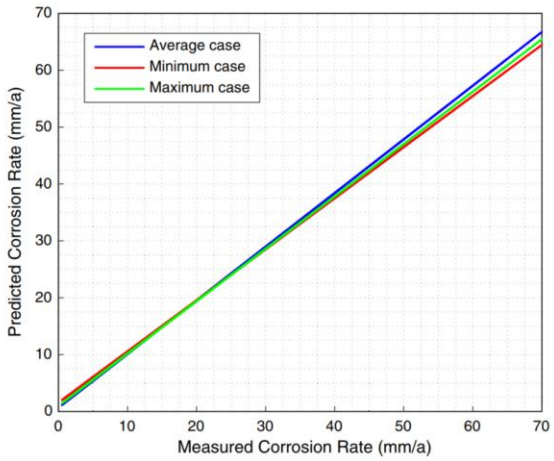

Figure 3-5: Experimental Corrosion Rate Uncertainty Effect on the Prediction Results

Summarized in Table 3-5 are the modelling output for each of the constructed dataset and presents the identified coefficients in (3-11) for each of the cases.

Table 3-5: Calibration Process Output - Uncertainty Effect

Dataset Type	**Calibrated Model**	**Deviation Angle (deg)**
Average	$log_{10}(CR_r^{final}) = 3.72 - (877.1 - 61.95V_m^{0.5} + 1.57pH^3)\frac{1}{T} + (0.98 + 0.008V_m^{0.5} - 0.02pH^3)\, log_{10}(f_{CO_2})$	43.35
Minimum	$log_{10}(CR_r^{final}) = 3.73 - (912.2 - 71.28V_m^{0.5} + 1.46pH^3)\frac{1}{T} + (1.03 - 0.02V_m^{0.5} - 0.018pH^3)\, log_{10}(f_{CO_2})$	41.94
Maximum	$log_{10}(CR_r^{final}) = 3.59 - (826.9 - 61.16V_m^{0.5} + 1.49pH^3)\frac{1}{T} + (0.76 + 0.003V_m^{0.5} - 0.015pH^3)\, log_{10}(f_{CO_2})$	42.65

The results are close, and the accuracy of the final model has not been majorly affected by the uncertainty presented in the original experimental dataset. Using the average corrosion rates for the duplicate testing conditions gave the closest prediction to the measured values, which supports the choice of the average corrosion rate value for each of the duplicate experimental conditions. Although this does not eliminate the fact that there is a need to perform a design-of-experiments enabling independent validation of the model along with a quantification of the uncertainty to ensure robust accuracy from the model.

Now consider the case of the CO_2 corrosion process in the presence of scale formation on the surface of the metal, a case not studied here. The increase of total pressure will lead to an increase of the CO_2 partial pressure that typically results in an increase of the corrosion rate. However, according to the available experimental data in [67], for the case of high pressures the recorded corrosion rates tend to stabilize between

5 and 20 mm/year. This observation might be explained by the fact that for some favorable conditions, when high temperature, high pH and high-pressure values are present, super-saturation of bicarbonate and carbonate ion are higher due to their increasing concentrations. This in turn accelerates the carbonate precipitation to create a protective film that reduces the tendency for CO_2 corrosion to occur. Taking into considerations the effect of the scale formation will improve the corrosion rate prediction and enhance the utility of the model during the design and dimensioning process of the transmission infrastructure.

Internal pitting corrosion is also one of the most influencing factors in the degradation and failure of oil and gas production pipelines [68]. It consists of a loss of metal at discrete areas due to localized attacks. This focused corrosion causes penetration of the pipe wall by pits where the protective film breakdown usually occurs. The corrosion propagation to the surrounding areas and could lead to different failures (e.g, leaks, burst or rupture). The main challenge then is to track these localized attacks and predict corrosion occurrence. Such knowledge will offer the possibility to understand the risk of failure of the corroded pipeline and act properly to manage its remaining strength.

Another important factor to consider is an experimental study involving high pressures beyond the 0.3 to 22 bar [66]. Higher internal pipe pressures associated with production systems will cause an increase in the pipe hoop stresses. These stresses will be especially concentrated at the pipe inner wall and pit locations, perhaps enhancing corrosion rates. It is unclear how high pressures will influence corrosion in the absence

of surface pits. Such tests are difficult to perform and would require experienced testing personnel.

3.5 Data-Based CO_2 Corrosion Rate Models Recalibration

The original DeWaard, Lotz and Milliams (DLM) model [63] is presented by

$$log_{10}(CR) = 5.8 - \frac{1710}{T} + 0.67 \times log_{10}(P_{CO_2}). \quad (3\text{-}21)$$

Based on the presented expression in (3-21), the recalibration is based on the structure given as

$$log_{10}(CR) = a_1 + \frac{a_2}{T} + a_3 \times log_{10}(P_{CO_2}). \quad (3\text{-}22)$$

The recalibration process result is given by (3-23) and this is achieved using the Least Square Method to identify the coefficients a_1, a_2 and a_3

$$log_{10}(CR) = 3.07 - \frac{738.4}{T} + 0.54 \times log_{10}(P_{CO_2}). \quad (3\text{-}23)$$

Shown in Figure 3-6 are the results of the recalibrated DLM model in (3-23) compared to the original model in (3-21) and the actual measured corrosion rates taken from [66] and [57].

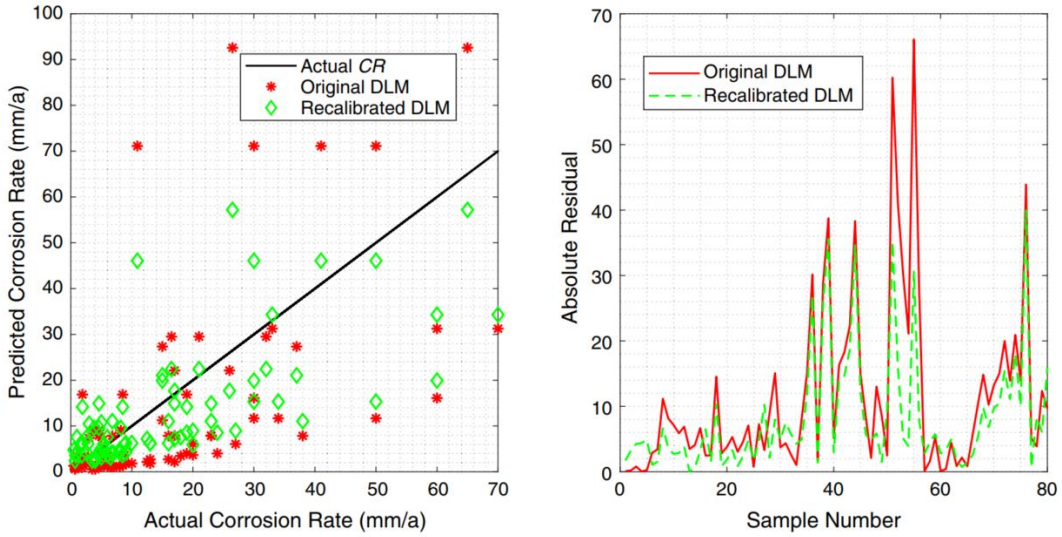

Figure 3-6: DLM Model Recalibration Results

Another data-based CO_2 corrosion rate model is presented by the NORSOK model. The original NORSOK model [62] is presented by

$$CR = K_t \times f_{CO_2}^{0.62} \times \left(\frac{S}{19}\right)^{0.146+0.0324\times log_{10}(f_{CO_2})} \times f(pH)_t. \tag{3-24}$$

Based on the presented expression in (3-24), the recalibration is based on the structure given by

$$CR = K_t \times f_{CO_2}^{a_1} \times \left(\frac{S}{19}\right)^{a_2+a_3\times log_{10}(f_{CO_2})} \times f(pH)_t. \tag{3-25}$$

The recalibration process result is given by (3-26) and this is achieved using a Non-linear Least Square optimization method to reduce the prediction error and identify the coefficients a_1, a_2 and a_3

$$CR = K_t \times f_{CO_2}^{0.59} \times \left(\frac{S}{19}\right)^{1.94+2.04\times log_{10}(f_{CO_2})} \times f(pH)_t. \tag{3-26}$$

Shown in Figure 3-7 are the results of the recalibrated NORSOK model in (3-26) compared to the original model in (3-24) and the actual measured corrosion rates taken from [66] and [57].

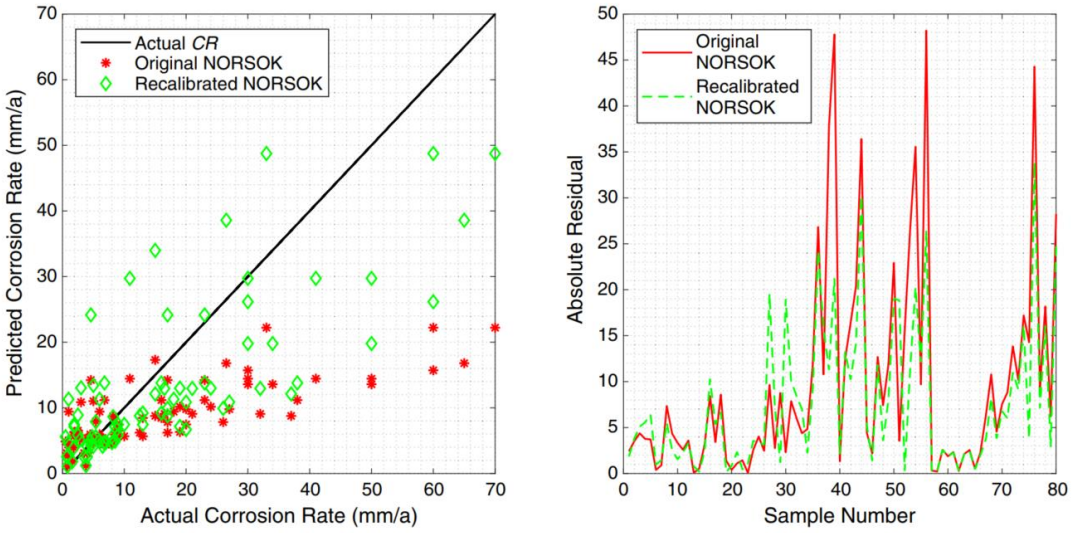

Figure 3-7: NORSOK Model Recalibration Results

3.6 Subsea Pipelines and Jumpers Sizing Based on Corrosion Analysis

Multiphase flow characteristics significantly affect the corrosion process of the steel pipelines in the oil industry. Presented in this section is a simulated case study for the model-based design of subsea architecture based on predicted corrosion rates. The oil and gas production from four different wells is grouped through a subsea manifold, which feeds the riser through a long production pipeline (Figure 3-8). The properties of gas and liquid phases, operating conditions and pipeline design parameters, namely the jumper and production pipeline diameters, are captured in Table 3-6.

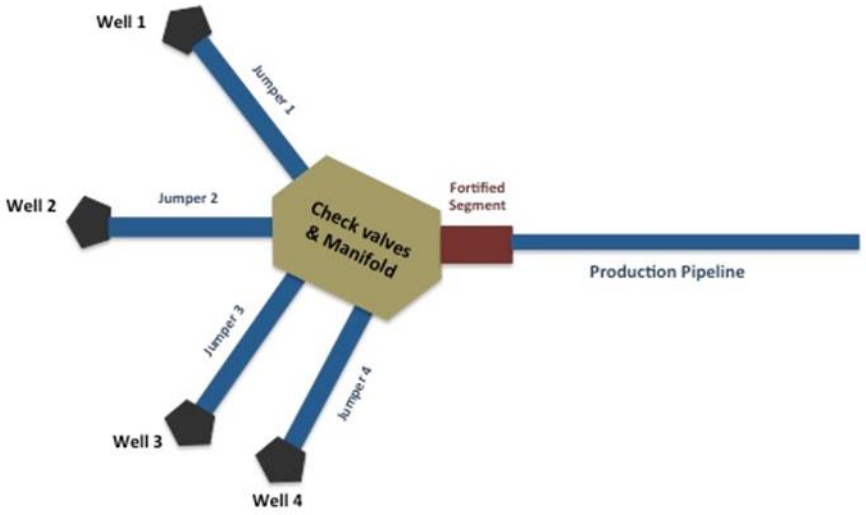

Figure 3-8: Schematic of a Subsea Manifold and Wells Connection

A digital twin is developed to mimic the steady state and dynamic behavior of the real subsea architecture. A physics-based model is derived for each subsea component, which is modeled using first principles. The models are then brought together and implemented in a MATLAB simulation environment. Next, the subsea architecture digital twin is integrated with the steady-state multiphase pattern to estimate the flow properties in the four jumpers and the production pipeline given the various scenarios. Finally, the results are used to estimate corrosion rate based on the proposed corrosion model. The proposed workflow is summarized in Figure 3-9.

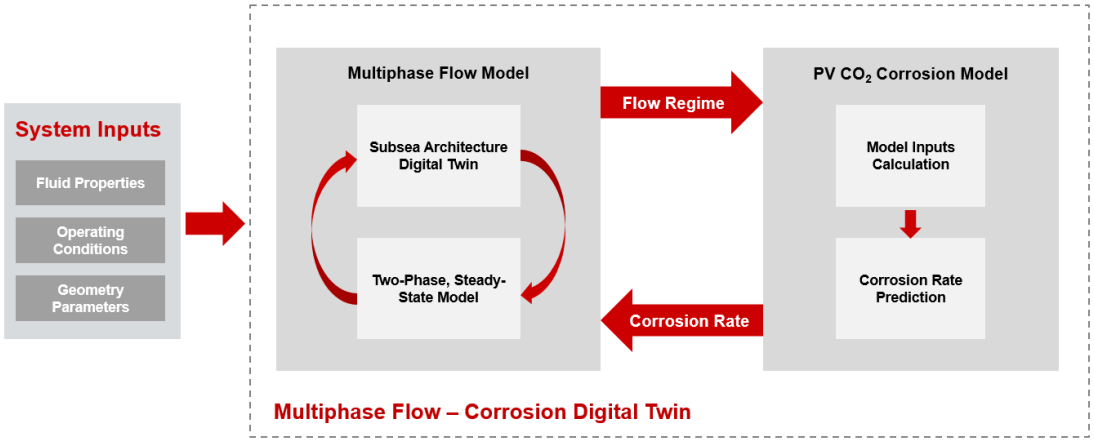

Figure 3-9: Multiphase Flow - Corrosion Rate Digital Twin

Table 3-6: Case Study Simulation Parameters

Operating Conditions	System inlet pressure	5E+07	Pa
	System outlet pressure	1.2E+05	Pa
Pipeline Sizing	Jumper length	50	m
	Production pipeline	10000	m
	Jumper diameter range	0.1-0.125	m
	Production pipeline diameter range	0.23-0.28	m
Fluid Properties	Liquid density	900	kg/m^3
	Liquid absolute viscosity	1.5E-03	Ns/m^2
	Liquid bulk modulus	1E+09	Pa
	Gas density	240	kg/m^3
	Gas absolute viscosity	1E-05	Ns/m^2
	Gas volume fraction	1-50	%

The subsea architecture digital twin is simulated for different pipeline sizing scenarios. For each simulated case, the liquid-gas two-phase steady-state model estimates the liquid and gas flow rates. The resulting liquid velocity serves as input to the proposed PV model to predict the corresponding corrosion rate. Illustrated in Figure 3-10 are the predicted corrosion rates of the four jumpers and the production pipeline for 1 percent gas-volume-fraction two-phase flow.

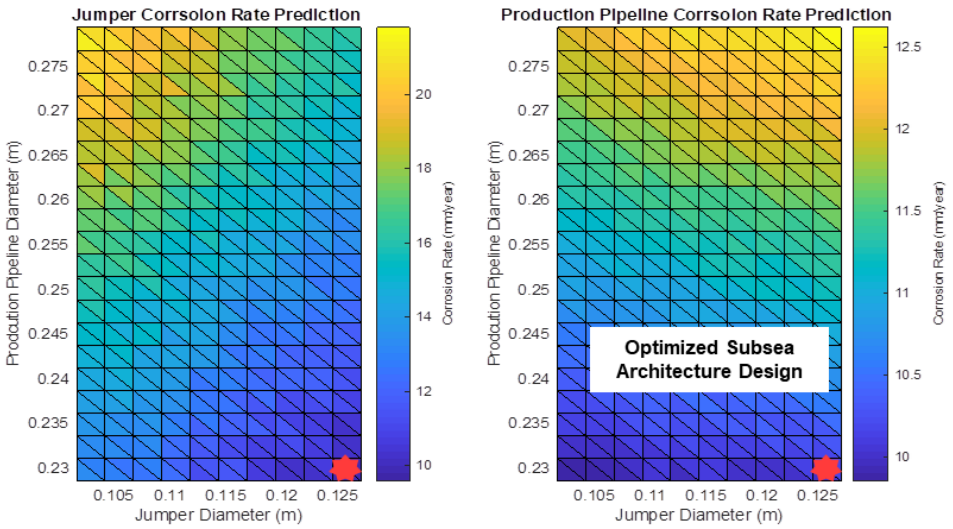

Figure 3-10: Pipeline and Jumper Corrosion Rate Prediction (GVF = 1%)

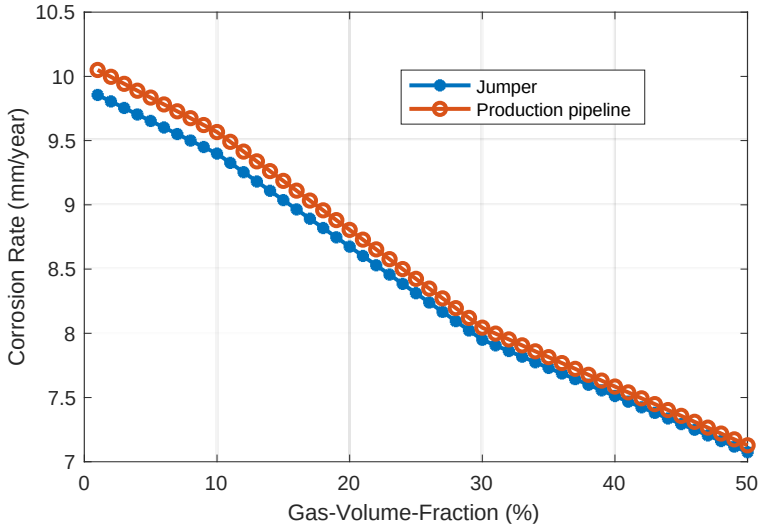

Figure 3-11: Relationship between GVF and Corrosion Rate

Results suggest that the corrosion rate in jumpers can be reduced by increasing jumper diameter and decreasing production pipeline diameter, whereas production pipeline corrosion rate can be reduced by decreasing both jumper and production

pipeline diameters. To optimize the subsea architecture based on minimizing the average corrosion rate of both lines, the optimal diameters are found to be 0.125 m and 0.23 m for the jumpers and the production pipeline, respectively. An investigation of the effect of the production fluid gas-volume-fraction on the system corrosion rate is also conducted. Presented in Figure 3-11 is the relationship between the gas-volume-fraction and the corrosion rate of the optimized subsea architecture lines. It can be concluded that corrosion rates can be mitigated by an increase in the gas-volume-fraction in the production fluid.

3.7 Conclusion

Numerous CO_2 corrosion models are available in the literature and have been used by industrial partners to perform corrosion rate prediction during the process of hydrocarbons production and transmission. However, the differences between these models will always bring up the issue of accuracy of the models [69]. In this study, a comparison of some of the existing CO_2 corrosion prediction models has been conducted using a common testing conditions to highlight the differences presented via their models structures as well as the required inputs required for each of the models. Performance benchmarking had been conducted to assess the most appropriate model to be used as a foundation in developing a newly data-driven model for CO_2 corrosion prediction, compared to the ones used in this study.

A "Parameter Varying" (PV) model is developed based on newly introduced model coefficients where the fluid factors influencing corrosion rates are nonlinear correlation between the pH and the flow velocity. The PV coefficients were not derived from

physics, instead it demonstrates a data driven approach based on a system identification methodology. A key aspect is its modularity that lends itself to isolated corrections derived from additional experimental and scientific studies. The proposed parameter varying CO_2 corrosion rate model is based on (3-8) developed in [52]. The parameter varying coefficients were identified by determining the functional relationship between flow parameters of velocity and pH to the residual generated between experimental data and (3-8). Significant improvements in CO_2 corrosion rate modelling were achieved. The resulting model produced an R-Squared value of 0.9 in comparison to 0.54 associated with (3-8). The maximum residual of the proposed model is 12 mm/year based on the validation dataset whereas the model in (3-8) is 24 mm/year.

Demonstrated through this investigation is an avenue for the development of an adaptive model, which if constructed using data analytics, will enable the descriptive, predictive, diagnostic, and prescriptive analytics (digital twin) that provides value-add to the oil and gas industry. This will be ensured by including more complex phenomena encountered in practical applications, such as the effect of the pipe steel composition and texture, effect of inhibitors, and modelling of localized attacks namely pitting corrosion.

4 MODEL-BASED SIMULATION APPROACH FOR PRE-FEED STUDIES FOR SUBSEA FIELD ARCHITECTURES DEVELOPMENT

4.1 Introduction

Presented is an integrated multi-physics model to autonomously perform a subsea field architecture pre-FEED study, which identifies the family of solutions satisfying pre-specified multi-objectives. From these identified solutions, subject matter experts can select those satisfying qualitative constants not captured in the pre-FEED investigation for a deep-dive analysis. Beyond its pre-FEED study utility, the proposed methodology provides a mechanism by which Artificial Intelligence algorithms can be deployed as self-learning routines to deal with the subsea production physics and design. The model enables real-time production system health monitoring via self-adaptation thereby producing estimates of fluid properties along the different nodes of the network. The proposed subsea production system model integrates multi-phase flow, heat, wax appearance, pipeline erosion, pipeline corrosion and slugging flow within the pipelines into one multi-physics model. The interactions among the sub-models are captured and analyzed as part of the pre-FEED study. The parametric uncertainties associated with the fluid properties such as gas volume fraction (GVF), density and viscosity play a key role in the pre-FEED as the robustness of the subsea systems and connections can be quantified. For the value of the pre-FEED study to be meaningful, the proposed model must include the effects that the seabed topology and obstacles have on the multi-phase flow regime. Without a loss of generality, the multi-objective function used to illustrate the model utility within an automated design process focuses on minimizing the pressure

differential along the network, and equipment and flow lines installation cost simultaneously.

This chapter is organized as follows. First, the multi-physics sub-models constituting a digital twin of a subsea production system are presented. A variety of models are developed to capture the different multi-physics aspect present within a fluid transmission system. Precisely, a steady state multiphase flow for pressure differential prediction as well as a thermal model are presented. Reduced order models and criterions are listed enabling a deep analysis of the overall system integrity and flow assurance issues. Both corrosion and erosion evaluation criterion have been presented as well as a wax deposition threshold. In addition, a thorough description of the overall well clustering process has been illustrated discussing all issues related to the limitations within the choice of cluster manifolds. Next, the overall optimization process is presented. Detailed representation of the objective functions and how they are evaluated along the subsea system for all the nodes is introduced. This section is extended by providing pseudocodes describing the hybrid optimization approach used such us the global scatter search process and the local gradient-based solver including the Dijkstra algorithm. Finally, some illustrative examples demonstrating the optimization abilities of the proposed autonomous solution and the different scenarios that can be deployed are presented. A deeper analysis is provided to demonstrate the utility of the presented solution as a testing platform for different analysis and scenarios, which makes it a decision support tool offering a fast yet efficient guidance for users during the design phase.

4.2 Subsea Field Digital-Twin for Autonomous Pre-FEED Design

In this section, a digital multi-physics representation of a subsea production system is developed. The adopted structure of the studied subsea production system is presented as the connection between wells, manifolds, and the platform. The development begins with a description of the multi-physics models required to digitally represent a subsea production system. In addition, those models capturing pipeline integrity assessment are provided. Next, a clustering solution that facilitates specific grouping of wells and manifolds is detailed. Such a feature allows for the customization of a subsea field architecture for practical considerations such as managing the number of connections, optimizing the size of manifolds as well as enabling future tiebacks extension. This section concludes with a mathematical description of the seabed topology.

4.2.1 Multi-physics Modeling of Subsea Production Subsystems

Presented herein are the primary subsystem models utilized to digitally represent a subsea production system. The organization of these sections begin with a steady state multiphase flow model that estimates the pressure differential, volumetric flow rate, and flow regime [23]. This flow model is followed by a heat transfer model that predicts the multiphase flow temperature differential along the pipeline. The coupling between the heat transfer and flow characteristics is addressed using an adaptation routine to update the fluid properties along pipelines.

4.2.1.1 Steady-State Multiphase Flow Modeling

The feature influencing facility specifications are the production fluids flowing within the network from the reservoir to the topside terminal. Two standard

classifications of flow are considered: single phase and multiphase flow. The latter one is the common general approach into representing the hydraulic component of a subsea production system since most of the flowing fluids in the oil and gas industry are presented as multiphase flows. The simultaneous presence of different phases leads to the observation of various fluid behaviors changing with the different phases' distribution. Hence, gaining knowledge and understanding of these complicated flowing conditions has great significance to analyze and study the variety of complex phenomena that occurs within a piping system as well as evaluating the integrity and the robustness of the overall subsea system. Quantifying the behavior of the flowing fluid will determine the decisions impacting the design and the production stage of a subsea field. In addition, model uncertainties in estimating the fluid dynamics are important factors influencing both the credibility of the simulation and the optimization of the overall network.

The goal is to directly incorporate the impact of flowing geometries (horizontal, inclined, and vertical) imposed by the topology of the seabed. Multiple multiphase flow correlations are available to develop these models. In this manuscript, the Beggs and Brill correlation [23] is chosen for assessing the pressure differential of the flowing fluid within all the subsea field architecture connections for different inclinations Figure 4-1 .This correlation is adopted to simulate the overall hydraulic part of the subsea network. It is noted that the modularity of the proposed digital subsea production system facilitates the use of alternative multiphase flow correlations.

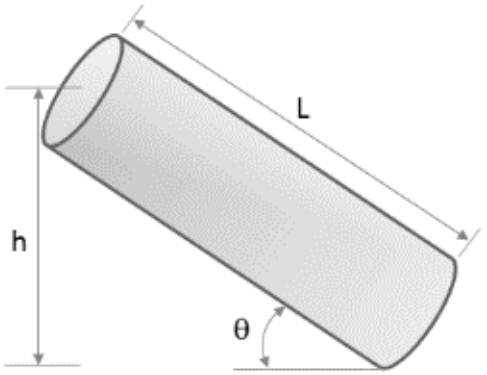

Figure 4-1: Inclined Pipeline

Given a pipeline with an inclination θ, as presented in [70], the total pressure differential can be presented by three different components: pressure differential due to elevation change, pressure differential occurring due to friction losses and pressure differential result of kinetic energy or convective acceleration. The latter component is generally equal to zero for the case of constant area pipelines where no change in velocity is present. Hence, for the hydraulic calculations in this study, the pressure differential expression presented by the Beggs and Brill correlation is adopted, given by

$$\Delta P = \Delta P_f + \Delta P_{HH}, \tag{4-1}$$

where ΔP_f is the pressure differential resulting from the friction losses and ΔP_{HH} is the hydrostatic pressure change (due to elevation changes). Once determining the flow regime within the pipeline, this correlation is used to calculate the liquid holdup E_L from which equivalent fluid properties are determined. An equivalent density of the flowing mixture ρmixture is calculated as

$$\rho_{mixture} = \rho_L E_L + \rho_G (1 - E_L), \tag{4-2}$$

and an equivalent mixture viscosity $\mu_{mixture}$ given by

$$\mu_{mixture} = \mu_L E_L + \mu_G(1 - E_L). \tag{4-3}$$

The hydrostatic pressure differential ΔP_{HH} can be obtained as a function of the liquid holdup E_L and the mixture density by

$$\Delta P_{HH} = \frac{\rho_{mixture} g L}{g_c} sin(\theta), \tag{4-4}$$

where L is the pipeline length, g is the gravitational constant and g_c is a gravitational conversion factor.

The pressure differential ΔP_f associated with the friction loss along the pipeline is determined based on the calculation of the no-slip density ρ_{NS}. This latter property is calculated with the constraint that both phases (liquid and gas) are moving at the same in situ velocity, thus giving as

$$\rho_{NS} = \rho_L C_L + \rho_G(1 - C_L), \tag{4-5}$$

where C_L is the no-slip liquid volume fraction defined as

$$C_L = \frac{V_{SL}}{V_{mixture}}. \tag{4-6}$$

In this case, V_{SL} is the superficial liquid velocity, and $V_{mixture}$ is the mixture velocity. The friction factor f_{tp} is based on the Beggs and Brill friction factor correlation for two phase flow [23]. The corresponding friction pressure differential is written as

$$\Delta P_f = \frac{2 f_{tp} V_{mixture}^2 \rho_{NS} L}{g_c D}. \tag{4-7}$$

4.2.1.2 Heat Transfer Modeling of Multiphase Flow in Pipelines

To assess the thermal aspect of a flowing fluid within a pipeline, a reduced-order two-phase flow thermal model presented in [71] is applied. The thermal information is necessary to determine the temperature gradient along a pipeline. Specifically, the temperature distribution profile along a pipeline give information concerning possible hydrates wax occurrence. Also, this information is important for selecting the insulation layer (thermal conductivity and layers thickness). In addition, having a two-phase-flow thermal model coupled with a two-phase-flow model exploits the interaction between the hydraulic and thermal sub-models to address the sensitivity of the fluid properties to the variation of the operating conditions along the pipelines.

Following a similar development used for the multiphase flow model, the following thermal model estimates equivalent fluid thermal properties producing an overall heat-transfer coefficient of the two-phase flow for different patterns. This coefficient depends on both the liquid holdup and pressure differential estimated by the fluid model. Several assumptions are considered when developing the proposed thermal model:

- Hydraulic and thermal properties of both liquid and gas phases are varying with respect to pressure, volume, and temperature.
- Heat flow is from the inner to the surrounding fluid.
- There is no mass transfer occurring between phases.
- Frictional heat generation caused by the fluid is negligible.
- Enthalpy of mixing is negligible,

- Energy exchange due to chemical reactions occurring within the pipeline is negligible.

The steady-state output temperature of the fluid at the end of a pipeline is expressed in [71] as

$$T_{out} = (T_{in} - T_{ambient})\, exp\left[\frac{-U \times \pi \times ID}{\dot{m} \times C_p} x\right] + T_{ambient}, \tag{4-8}$$

where $\dot{m}$ is the fluid mass flow rate, C_p is the fluid specific heat capacity and U is the overall heat-transfer coefficient within the pipeline given as

$$U^{-1} = \underbrace{ID \times \sum_{i=1}^{n+1}\left[\frac{ln\left(\frac{ID_{i+1}}{ID_i}\right)}{2k_{cond_i}^{material}}\right]}_{Conduction} + \underbrace{\frac{1}{h_{tp}} + \frac{1}{h_0 \times \left(\frac{OD}{ID}\right)}}_{Convection}, \tag{4-9}$$

where $k_{cond_i}^{material}$ is the corresponding material conductivity and h_0 is the external convection heat transfer coefficient.

The main challenge for two-phase flow is to estimate the two-phase convection heat transfer coefficient, h_{tp}. This coefficient is a function of the flow characteristics, hydraulic and thermal properties of the fluid as well as the flow pattern present within the pipeline. Thus, the model in [71] presents a detailed method to estimate the fluid convection heat transfer coefficient by taking into account all these listed factors.

4.2.1.3 Adaptive Coupling of the Flow and Heat Transfer Models

To improve the robustness of the fluid hydraulic and thermal properties estimation along the pipeline, a self-adapting process that tracks the changes of the fluid operating temperature and pressure, and updates the fluid properties respectively is employed (Figure 4-2).

The proposed solution is based on the implementation of a lookup table to update both hydraulic and thermal properties considering the changes of the in-line pressure and temperature. The lookup table is created based on a database presented as pressure/volume/temperature (PVT) file. The selected database is generated in advance based on the fluid mixture and composition at the reservoir level using the PVTsim software. Hence, this database can be given by the user depending on the property of the reservoir or fluid in question.

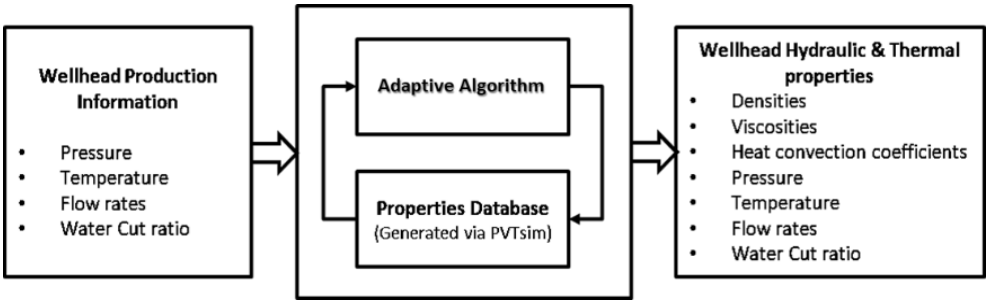

Figure 4-2: Fluid Properties Update Block Scheme

Table 4-1: Updated Fluid Properties – Self-Adapting Block

Updated Variable	Description	Unit
ρ_L	Liquid Phase Density	kg/m^3
ρ_G	Gas Phase Density	kg/m^3
μ_L	Liquid Phase Viscosity	Pa.s
μ_G	Gas Phase Viscosity	Pa.s
Cp_L	Liquid Phase Specific Heat Capacity	J/(kg.C)
Cp_G	Gas Phase Specific Heat Capacity	J/(kg.C)
K_L	Liquid Phase Heat Conductivity	W/(m.C)
K_G	Gas Phase Heat Conductivity	W/(m.C)

The updated fluid properties during this process are summarized in Table 4-1. By incorporating these self-adaptive features, a broader range of studies is achieved. Specifically, more accurate quantification of the fluid properties along the different segments of a pipeline is realized. Hence track changes of the fluid regime is enabled

along with the possible occurrence of flow assurance issues. In addition, the self-adaptive process is implemented during the optimization process to consider the effect of changes of the pressure and temperature at each of the subsea system nodes.

4.2.2 Pipeline Degradation Processes Modeling

During the design phase of a subsea field architecture, several issues are addressed to produce solutions that avoid unrealistic connections schemes. Thus, incorporating different optimization constraints is needed. In the following section, several constraints are introduced to impose different design requirements such as structural, mechanical, thermal, and hydraulic considerations.

4.2.2.1 Pipeline Erosion Modeling

One of the important factors during the design of a subsea system is the rate of erosion. Such phenomenon can lead to maintenance consequences regarding the system integrity and longevity. Interior erosion is contingent upon the nature of the flowing fluid as well as the hydraulic characteristics of the mixture, specifically the fluid mean velocity. Incorporating this constraint in the optimization and pipeline sizing process of the subsea field element is paramount.

A widely deployed solution to address erosion within a subsea pipeline is the API 14E standard requirement for pipeline design and sizing, where under specific input conditions a maximum erosional velocity is specified for the mixture mean velocity. This limit is defined in the API 14E standard [72] as

$$V_{erosion} = \frac{C}{\sqrt{\rho_{mixture}}}. \tag{4-10}$$

To minimize the erosion within the pipeline, the mixture mean velocity must be less than the erosional velocity threshold. A constraint is developed given the erosional ratio Eratio and defined as

$$E_{ratio} = \frac{V_{mixture}}{V_{erosion}} < 1, \tag{4-11}$$

where C is the API 14E erosion factor, $V_{erosion}$ is the erosional velocity, $V_{mixture}$ is the mixture mean velocity and $\rho_{mixture}$ is the mixture equivalent density.

4.2.2.2 Pipeline Corrosion Modeling

In addition to erosion, corrosion is also considered as a concern that has an impact on the reliability and the service life of a subsea production system. Having an accurate estimation of the corrosion rate within the optimization process facilitate material specifications and sizing of the elements. The model derived in [73] quantifies the corrosion rate within the subsea network pipelines, jumpers and riser. The corrosion rate model is a data-driven model presented as a parallel resistance model given as

$$\frac{1}{CR} = \frac{1}{CR_{act}} + \frac{1}{CR_{Mass}},$$

$$log_{10}(CR_{act}) = 3.72 - (877.1 - 61.95V_{mixture}^{0.5} + 1.57pH^3)\frac{1}{T}$$
$$+(0.98 + 0.008V_{mixture}^{0.5} - 0.02pH^3)\, log_{10}(f_{CO_2}), \tag{4-12}$$

and

$$CR_{Mass} = 2.45\frac{V_{mixture}^{0.8}}{D^{0.2}} f_{CO_2}.$$

In this model, both pH and CO_2 fugacity are considered to estimate the corrosion rate CR as a function of two different corrosion rate quantities, namely CR_{act} representing the contribution of the activation reaction kinetics and CR_{Mass} representing

the contribution from the mass-transfer kinetics due to the mixture velocity. Knowing the lifespan of the pipeline, a penetration depth t_p is determined as

$$t_p = CR \times lifespan. \tag{4-13}$$

To ensure an acceptable design, a maximum corrosion allowance t_e is chosen so that

$$t_p < t_e. \tag{4-14}$$

Thus the pipeline minimum wall thickness t is determined according to the ANSI/ASME standard B31.1 [74] by the following expression

$$t = t_e + t_{th} + \left[\frac{P \times OD}{2(S_p \times E + P \times Y)}\right]\left[\frac{100}{100 - T_{ol}}\right], \tag{4-15}$$

where t_{th} is the thread or groove depth, P is the allowable internal pressure in the pipeline, OD is the outer diameter of the pipeline, S_p is the allowable stress for the pipeline, E is the longitudinal weld-joint factor, Y is the derating factor and T_{ol} is the manufacturer allowable percent tolerance.

4.2.2.3 Pipeline Wax Appearance Modeling

Another factor impacting the structural integrity of a pipeline is the appearance of hydrates wax at the internal surface of the pipeline. This has significant effects on the fluid transportation through the flow line by reducing the flow rate of the mixture due to a plugging of the pipeline. The wax deposition process occurs when the temperature of the medium falls below a threshold temperature known as the wax appearance temperature (*WAT*) [75]. A well-designed pipeline reduces/avoids the possibility of wax deposition within the system. This is achieved by optimally choosing the pipeline size

and the insulation layer properties so that the flowing mixture temperature stays above the *WAT*, namely

$$T > WAT. \tag{4-16}$$

The flowing mixture temperature T is going to be presented as the mixture temperature at each node of the subsea field layout following the discretization process presented in the next section. To evaluate the constraint requirement presented in (4-16) during the optimization process, the thermal model previously presented is used to calculate the temperature along the different connection in the subsea field.

4.2.3 Subsea Wells Clustering

The objective of this investigation is to determine an optimal pipeline connection scheme offering the shortest pipeline length to reduce the CAPEX of the architecture. However, this routing must minimize the pressure differential ensuring that the maximum production is achievable within the system. During this process, a number of constraints is imposed, namely flow assurance and structural stability criterions. Specifically, maintaining measures like wax appearance temperature, erosional velocity and corrosion maximum allowance within acceptable ranges.

The production fluids are flowing from the wellheads, merge at the manifolds and flow back to the riser base to arrive at the topside platform. The overall system is presented as a set of spatial nodes interconnected by pipelines. Each node is identified by three coordinates (*x, y, z*), representing the planar coordinates (*x* and *y*) and the elevation above the seabed *z*. Letting *n* denote the number of wells, each well is presented as a node given by $W_i = (x_{W_i}, y_{W_i}, z_{W_i})$, where *i=1:n*. Similarly, if

considering m manifolds, then each one is presented by $M_j = (x_{M_j}, y_{M_j}, z_{M_j})$, where *j=1:m.*

In a subsea field, a good practice has been reducing the number of connections between wells and platform. Especially when in the case of a large-scale oil and gas field, where many subsea wells are present. This makes the connection of all the wells to a one manifold inadequate and even if it is possible it will require a large size manifold. Hence, deploying smaller size manifolds instead is more practical. To achieve this goal, grouping the wells into small number of assemblies is one approach in a field where many scattered wells are present.

4.2.3.1 Subsea Cluster Manifold

A cluster manifold is a widely used equipment within the subsea industry, usually deployed to reduce the number of tiebacks connected to the topside terminal [76]. The main reason to deploy such a structure is the flexibility to group and segregate any set of wells. It offers the ability to present a set of wells as one production entity (Figure 4-3).

In addition, using such an approach is advantageous in the sense of reducing the overall equipment cost as well as extending the field by connecting additional scheduled tiebacks. Also, the cluster manifold plays an important role in increasing the production efficiency of the subsea system [77].

This equipment is used to guide the production enhancement process by presenting a gathering point for the boosting injected products (water, gas, and chemicals) that are distributed to all the subsea wells to which it is connected. Hence, this offer the

accessibility to enhance the reservoir pressure, control the hydrate formation and improve the hydraulic performances of the overall subsea system. Yet, this does not eliminate the fact that large-scale equipment comes with several limitations such as the complexity and inflexibility during the installation process as well as safety matters during production operations. The manifold cluster type employed depends on the number of wells to be connected as well as the field development schedule which requires a certain number of reserved slots for future wells extension. Each manifold normally accommodates between 4 to 10 connection slots [76].

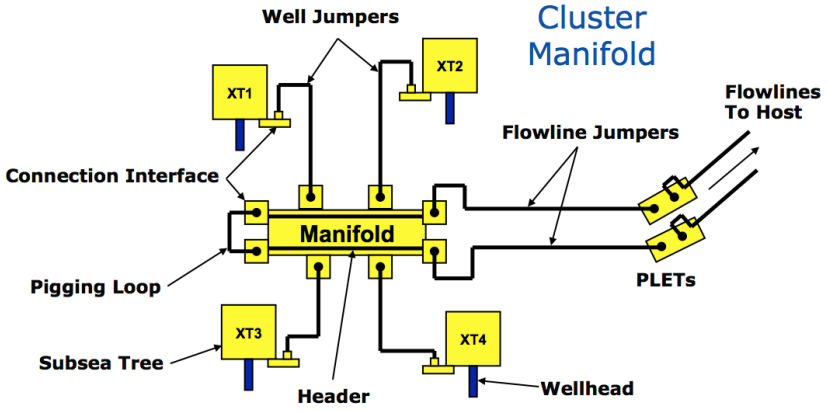

Figure 4-3: Cluster Manifold Configuration[78]

4.2.3.2 Subsea Wells Clustering Process

To group a set of wells into one entity based on the distance between them, a geometric clustering algorithm is adopted. Specifically, a *k-means* algorithm is used to divide the scattered wells into groups based on the Euclidean distance between wells given as

$$dist(W_i, W_j) = \left(\left(x_{W_i} - x_{W_j}\right)^2 + \left(y_{W_i} - y_{W_j}\right)^2 + \left(z_{W_i} - z_{W_j}\right)^2\right)^{0.5}. \quad (4\text{-}17)$$

Note that given the *k-means* algorithm limitations, there are no constraints that can be imposed regarding the size of each cluster. However, only few types of cluster manifolds are available depending on the number of connection slots (4, 6, 8 and 10 slots). Hence, the size of the well groups will directly depend on the type of cluster manifold installed. To overcome this limitation, a modified version of the *k-means* clustering algorithm is implemented [79]. This method offers the possibility to define the size of the well groups based on the cluster manifolds used. In this work, changes are proposed to the original k-means algorithm, so a user can incorporate the preferred size for each cluster separately. To apply this method, each of the cluster sizes is specified (Figure 4-4).

In the case of not knowing this information a-priori, the proposed subsea field architecture design algorithm will determine the required sizes for each cluster by considering the optimal number and type of cluster manifolds required to connect all wells as well as take into considerations future scheduled tiebacks.

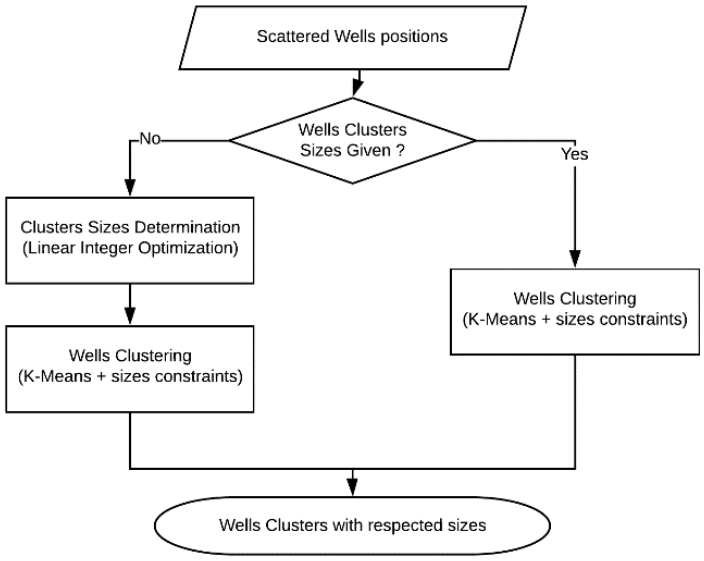

Figure 4-4: Subsea Wells Clustering Process

These manifolds are selected among the existing types, which translates into the combination of cluster manifolds allowing the connection of all the wells with minimum equipment cost. The sizes of the possible clusters are determined by solving the following optimization problem

$$\min_{Nbr_{manifolds}} COST_{manifolds},\ s.t \begin{cases} Nbr_{manifolds}: Integers \\ \sum_{k=1}^{4} Nbr_{manifolds}(k) \times Nbr_{slot}(k) \ \geq n' \end{cases} \quad (4\text{-}18)$$

where $COST_{manifolds}$ is the vector containing the cost of the different manifold types as listed in (Bai and Bai 2018), $Nbr_{manifolds}$ is the vector containing the number of manifolds used from each type, Nbr_{slot} is a vector listing the number of slots for each manifold type ($Nbr_{slot} = (4,6,8,10)$) and n is the number of the subsea wells within the field.

4.2.4 Seabed Topology Approximation

The seabed is introduced as a 3D profile to incorporate both elevation changes and topographic obstacles. Since an actual seabed cannot be represented as a continuous surface function, a discrete representation is used. The seabed is discretized at the nodes by their *x* and *y* coordinates and elevation *z*. In this case, these nodes are used as a gridded space during the optimization process. If this information is not available, the seabed profile will be approximated using a surface function to emulate the elevations. One such surface function is the cubic B-spline interpolation given as

$$z(x,y) = \sum_{k} {z_k}^0 . exp\left(-\left(\frac{|x - x_c|}{u_k}\right)^{p_k} - \left(\frac{|y - y_c|}{v_k}\right)^{q_k}\right), \tag{4-19}$$

where x_c, y_c, u_k, v_k, p_k and q_k are fitting parameters. In this development, the seabed topographic profile to be studied is illustrated in (Figure 4-5).

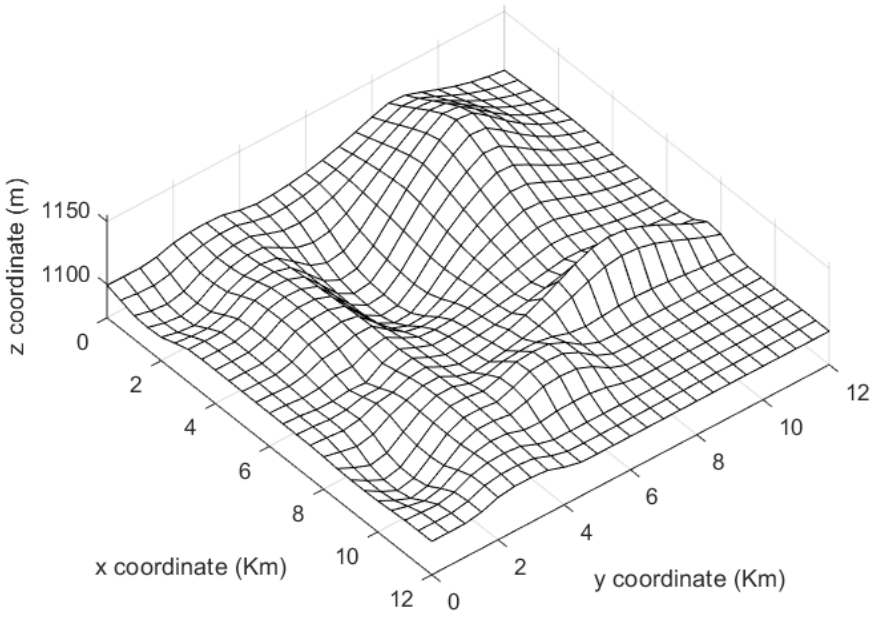

Figure 4-5: Example of a Discrete Representation of a Seabed

4.3 Mathematical Formulation of the Pre-FEED Design Algorithm

The optimal field layout is identified by maximizing the production (minimizing the pressure differential) while minimizing the cost. The first objective function is adopted based on the importance of considering the hydraulic properties of the flowing fluid, especially in the case of multi-phase flow. Precisely, in the case of a 3D seabed, pipelines can be passing through uphills and downhills. Hence, a lot of energy is lost and not regained through these elevation changes. Therefore, minimizing the pressure drop along the piping scheme is crucial in order to avoid these losses and maintain a connection plan that tends to avoid as much as possible any important elevation variation especially valleys considered as liquids traps [80, 81]. The latter objective is mainly dependent on the pipelines routing scheme and pipelines sizes (inner diameters) that directly influence the specified flow assurance constraints as well as the overall cost of the subsea production system. Hence, the optimization problem in this study can be presented as a multiobjective optimization where the goal is to find the optimal design that assure the minimum possible cost while considering having the least amount of overall pressure differential (maximizing the production rates) along the subsea system in order to respond to the issues illustrated before.

This optimization problem of the subsea layout subject to the flow assurance and hydraulic constraints is presented as follows

$$\min_{\substack{Design \\ Variables}} \{\alpha \times \Delta P_T + (1-\alpha) \times COST_T\}, \tag{4-20}$$

where ΔP_T is the overall pressure differential along the subsea network, $COST_T$ is the overall cost of the manifolds and flow lines, α $(0 \leq \alpha \leq 1)$ is the weighting factor (for the multi-objective optimization) and the design variables are the manifolds positions and the pipelines routing and sizing. The reason to use a weighting factor is to represent the multi-objective optimization problem as a multi-criteria decision-making process. Hence, the possibility of providing a solution that can help making optimal decisions requiring tradeoffs between two objectives (in our case the overall pressure differential and the overall cost).

Since the proposed automated subsea field architecture methodology involves a multi-objective function, the optimization process operates on a comparison among subsea system optimization constraints. Such a comparison is probably ill posed-since each constraint has different units leading to differing orders of magnitude. Therefore, it is necessary to transform each term in the multiple objective function such that all have similar orders of magnitude. One approach is to normalize the individual objective functions by dividing each term by the magnitude 10^k or by their respective absolute function values at the initial design [82]. In this case, the initial design of the subsea field architecture is determined based on the initial design variables fed to the optimization process. Specifically, the initial design is presented as the initial positions of the manifolds, straights connections between the wells and their associated manifold as well as pre-selected values for the pipeline's inner diameters and thickness. The new normalized objective function is obtained as

$$\min_{\substack{Design \\ Variables}} \left\{ \alpha \times \frac{\Delta P_T}{\left|\Delta P_{T,ini}\right|} + (1-\alpha) \frac{COST_T}{\left|COST_{T,ini}\right|} \right\}, \tag{4-21}$$

where $\Delta P_{T,ini}$ and $COST_{T,ini}$ are respectively the pressure differential and the total cost of an initial design. In this description, ΔP_T is the overall total pressure differential within the subsea system defined as

$$\Delta P_T = \sum_{i=1}^{n_c} \Delta P_i, \tag{4-22}$$

where ΔP_i is the total pressure differential of the i^{th} wells set (pressure differential between the wells and the riser base or platform) and n_c is the number of wells groups (result of the clustering step). Hence, for the well set i with a cluster manifold M_i connected to m_i wells and the platform, ΔP_i is given as

$$\Delta P_i = \Delta P_{M_i}^{Platform} + \sum_{j=1}^{m_i} \Delta P_{W_{i,j}}^{M_i}, \tag{4-23}$$

where $\Delta P_{M_i}^{Platform}$ is the pressure differential between the manifold M_i and the riser base or platform and $\Delta P_{W_{i,j}}^{M_i}$ is the pressure differential between a well $W_{i,j}$ in the ith well set and the corresponding manifold M_i. To determine the optimal pipeline routing between all the facilities, the subsea seabed is gridded into vertices and edges. Hence, any connection is segmented into small portions passing from node to node within the gridded space. In this case, the pressure differential between any two elements (well-manifold, manifold-platform) is discretized based on the mesh used to grid the field as well as the number of segments chosen. Discretizing the connections between a well $W_{i,j}$ in the i^{th} wells set and the corresponding manifold M_i divided into $n_{W_{i,j}}^{M_i}$ segment, the pressure differential $\Delta P_{W_{i,j}}^{M_i}$ is calculated as

$$\Delta P_{W_{i,j}}^{M_i} = \sum_{k=1}^{n_{W_{i,j}}^{M_i}} \Delta P_{N_k}^{N_{k+1}}, \tag{4-24}$$

where $\Delta P_{N_k}^{N_{k+1}}$ is the pressure differential between two consecutives nodes. Also, the connection between the manifold M_i and the platform is divided into $n_{M_i}^{Platform}$ segments, the pressure differential along that connection is obtained as

$$\Delta P_{M_i}^{Platform} = \sum_{k=1}^{n_{M_i}^{Platform}} \Delta P_{N_k}^{N_{k+1}}. \tag{4-25}$$

The additional term in the objective function to minimize is the total cost of the subsea network. The total cost is divided into pipelines cost and manifolds cost

$$COST_T = COST_{pipelines} + COST_{Manifolds}, \tag{4-26}$$

where $COST_{Manifolds}$ is the cost of the installed cluster manifolds and $COST_{pipelines}$ is the cost of all the installed pipelines given as

$$COST_{Manifolds} = \sum_{i=1}^{n_c} COST_{M_i} \tag{4-27}$$

and

$$COST_{pipelines} = \sum_{i=1}^{n_c} COST_i, \tag{4-28}$$

where $COST_i$ is the total cost of the pipelines within the i^{th} wells set added to the cost of the connection between the corresponding cluster manifold M_i and the platform giving by

$$COST_i = COST_{M_i}^{Platform} + \sum_{j=1}^{m_i} COST_{W_{i,j}}^{M_i}. \tag{4-29}$$

Using a similar discretizing process, the pipeline cost between the j^{th} well $W_{i,j}$ and the corresponding cluster manifold M_i is determined by

$$COST_{W_{i,j}}^{M_i} = \sum_{k=1}^{n_{W_{i,j}}^{M_i}} COST_{N_k}^{N_{k+1}} \tag{4-30}$$

and the cost of the connection relating the cluster manifold M_i to the platform is calculated by

$$COST_{M_i}^{Platform} = \sum_{k=1}^{n_{M_i}^{Platform}} COST_{N_k}^{N_{k+1}}. \tag{4-31}$$

Both costs for the manifolds as well as the pipelines are calculated based on the information listed in [83]. A manifold M_i cost is estimated as

$$COST_{M_i} = f_0 \times f_1 \times f_2 \times f_3 + C_{corr}. \tag{4-32}$$

where $COST_{M_i}$ is the cost of manifold, f_0 is the basic cost of a manifold, f_1 is the tree type cost factor, f_2 is the pressure rating cost factor, f_3 is the bore size cost factor and C_{corr} is a correction cost. For the pipeline, the cost of a segment between two nodes N_k and N_{k+1} of a length L_k is given as

$$COST_{N_k}^{N_{k+1}} = f_t \times f_s \times C_0 \times L_k + C_{misc}, \tag{4-33}$$

where f_t is the flowline type cost factor, f_s is the flowline size cost factor, C_0 is a base cost and C_{misc} is the coating cost.

A necessary additional operation evaluated during the optimization process is the calculation of the temperature at each node. This is necessary because evaluating

the changes of both pressure and temperature at each point of the grid is needed. The updated pressure and temperature are used to adapt the hydraulic and the thermal properties of the fluid. These properties are deemed indispensable to evaluate the different sub-models at the next node.

Assuming that both the pressure P_k and the temperature T_k are calculated at a specific node N_k in one of the connections, the fluid properties are updated by interpolating a predefined database to determine the properties based on the values of P_k and T_k (Figure 4-2). These properties are then identified for the next node N_{k+1}. The pressure differential $\Delta P_{N_k}^{N_{k+1}}$ is calculated to determine the pressure P_{k+1} and the temperature T_{k+1} defined as

$$P_{k+1} = P_k - \Delta P_{N_k}^{N_{k+1}} \tag{4-34}$$

and

$$T_{k+1} = (T_k - T_{ambient})\, exp\left[\frac{-U_k \times \pi \times ID}{\dot{m}_k \times C_{p,k}} \times L_k\right] + T_{ambient}, \tag{4-35}$$

where U_k is the overall heat transfer coefficient at the pipeline segment $N_k - N_{k+1}$, $C_{p,k}$ is the specific heat capacity of the fluid updated at the node N_k and $\dot{m}_k$ is the mass flow rate at the same node. This process is evaluated for all the nodes that constitute a specific connection between two entities within the subsea field.

Using the discretization process described above, the pressure and temperature values at each node of overall subsea layout can be determined. However, to be able to assess the pressure and temperature values at all the nodes constituting the whole subsea system, a crucial task is needed to be fulfilled, precisely, determining the pressure and temperature values at the level of the manifolds. This can be associated with certain

limitation since each manifold is connected to several wells and each connection can result in different values for pressure and temperature. To overcome this issue, an additional constraint has been considered. This constraint is deployed to make sure that the different pressure values resulting from the different connections in one manifold are the same. For the case of the temperature, the cluster manifold has been considered as a multiple input single output system. Hence, the temperature at the manifold is defined as the mixture temperature of all the fluids flowing from the different wells connected to this manifold. For example, having a manifold *M* connected to *m* wells (w_i , $i = 1{:}\,m$), for each connection between a well w_i and the manifold *M*, the temperature of the fluid flowing from w_i to *M* at the manifold level is given as . The final fluid mixture temperature at the manifold (T_M) is then determined as follows:

$$T_M = \frac{\sum_{i=1}^{m} \dot{m}_M^i C_{p,M}^i T_M^i}{\sum_{i=1}^{m} \dot{m}_M^i C_{p,M}^i}, \tag{4-36}$$

where $\dot{m}_M^i$ and $C_{p,M}^i$ are respectively the mass flow rate and the specific heat capacity of the fluid flowing from w_i to *M* at the manifold level.

In a subsea field, finding the optimal routing map to connect the different facilities is paramount. One choice is to select a straight line between two entities. However, this connection can be impossible or non-optimal due to the presence of topographic obstacles and undesirable regions necessary to avoid. To incorporate this requirement, a path finding algorithm is used. The well-known Dijkstra algorithm is deployed [84]. This algorithm has been used to solve the problems of pipelines routing within oil and gas production and gathering systems [80].

With the subsea field represented as a set of connected nodes, the optimal path between two points within this grid is found by evaluating the possible paths that produce the minimum cost. The cost of a path is the cumulative cost necessary to pass from one node to another. To use the Dijkstra algorithm, a connection matrix $\boldsymbol{B}$ and a cost/weight matrix $\boldsymbol{W}$ is used. The former matrix defines the connection scheme within the grid. Each node is connected to the eight surrounding neighbor nodes, and the connection matrix can be defined as

$$\begin{aligned} &\boldsymbol{B}(l,m) = 1, \qquad if \quad N_l \ and \ N_m \ \ are \ adjacent \\ &\boldsymbol{B}(l,m) = 0, \qquad if \quad N_l \ and \ N_m \ \ are \ not \ adjacent. \end{aligned} \tag{4-37}$$

The latter matrix is defining the weight or the cost of passing from one node to the other. In the case of present obstacle within the field, a vector of the nodes related to the obstacles is provided by the user to denote the border of this restriction. Then, during the path search process, the Dijkstra algorithm is adapted so that at each segment connecting two of these nodes the weight is set as infinity (∞) to emphasize on the fact that these regions are undesirable, hence, the Dijkstra algorithm avoids them. Then, employing the rule of eight neighbor nodes, the cost matrix, defined based on the objective function, is given as

$$\begin{aligned} &\boldsymbol{W}(l,m) = w(l,m), \qquad if \quad \boldsymbol{B}(l,m) = 1 \\ &\boldsymbol{W}(l,m) = \infty, \qquad if \quad \boldsymbol{B}(l,m) = 0, \end{aligned} \tag{4-38}$$

where $w(l,m)$ is the objective function evaluated between the node N_l and N_m.

However, the fluid properties in each node are depending on the variation of both pressure and temperature. This will affect the calculation of the weight between two nodes N_k and N_{k+1}. Precisely, the weight will be depending on the variation at the

level of the initial node. Hence, the problem becomes a varying weight short path search. To overcome this issue, the variation of the weights when applying the Dijkstra algorithm are taken into account [85].

Two type of connections are present, wellhead-manifold and manifold-riser base connection. Hence, starting from an inlet node, the Dijkstra algorithm evaluates all the candidate nodes and estimates the minimum cumulative cost until reaching the ending or the output node. The Dijkstra algorithm has been used only to find the optimal path between each of the subsea wells within a cluster and the corresponding manifolds while minimizing the pressure differential and costs. However, to be able to fulfill this objective, the definition of the manifold's locations and the pipelines inner diameters is required to be fixed in advance. Therefore, an integration of the optimal path search algorithm within a gradient-based local solver search routine will help search for the optimal locations of manifolds and pipelines sizes, and in the same time guarantees that for each of the optimization candidates solutions, the optimal connection scheme is determined. Hence, because of this integrated process, optimal manifolds locations as well as optimal pipelines sizes are determined along with the optimal connection scheme.

In the other hand, since the convexity of the problem (local or global minimum) is unknown, a hybrid process is adopted to ensure that the proposed methods generate a solution as close as possible to the global minimum. This hybrid method is based on a global search algorithm to find global optima. This is achieved by combining a scatter search algorithm to generate trial or candidate starting points to be fed to a gradient-based local non-linear problem solver [86]. Both the scatter search process as well as

the local solver optimization routine including the integration of the Dijkstra Algorithm for the optimal path search objective are presented as follows,

Algorithm 1: *Global Scatter Search Algorithm*

Inputs: *Initial solution x_0, Number of trial points, Solution Boundaries, Optimization Problem, Constraints*

Output: *Global Optimal Solution*

Initialization:

- *Read problem parameters;*
- *Generate Trial Points population;*
- *Initialize Global Solution Vector;*

First Local Solver Run:

- *Run Local Solver for Initial Solution $x_{0;}$*

Stage 1: Distance and Merit Criterion*

- *Evaluate Objectives and constraints at trial solutions;*
- *Compute Penalty functions for trial solutions;*
- *Select Best Points from Trial Solutions;*
- *Run Local Solver for best point from trail solutions;*
- *Set Distance and Merit criterion **;*

Stage 2: Main Iterative Loop

- *Evaluate objective and constraints at trial solutions (except selected before);*
- *Check merit and distance criterion;*
- *Run Local Solver for trial solution;*
- *Update Global Solution Vector;*

Final Stage: *Select best solution from Global Solutions Vector;*

The distance and merit criterion* are set to ensure the quality of the starting point selected from the trial points population. Precisely, as discussed in [86], the distance's criteria is implemented to guarantee that the proposed starting points are far from any previously found local solution. The main objective of this method is to prevent the local solver from starting within the same basin of attraction of any previously determined local optimum for more than once. In the other hand, the merit criterion is presented to guarantee the quality of the chosen starting points used by the local solver. Specifically, it ensures that the starting point have a penalty function value less than the penalty function threshold defined by the best candidate point from Stage 1 of Algorithm 1 (In this case the penalty function is determined based on the evaluation of the objective functions at the specific starting point and adding a weighted function expressing the possibility of constraints violation).

Algorithm 2: *Local Minimum Search Algorithm*

Inputs: *Initial solution x_0, wells clusters, Solution Boundaries, Optimization Problem, Constraints*

Output: *Local Optimal Solution (manifolds positions, pipelines inner diameters, piping path)*

Initialization:

- *Read problem parameters;*
- *Initialize Local Solution;*

Optimization Process:

a) Generate Potential Solution;

b) Extract Manifolds proposed positions;

c) Extract Pipelines proposed sizes (Inner diameters);

d) Objective Function Evaluation

Total_Objective_fcn=0;
While (i<= Number of wells clusters)
Do {
Cluster_Objective_fcn=0;
For ($W_{i,j}$ in Cluster i)
Do {
Search for Optimal Path between $W_{i,j}$ and M_i; ***(Dijkstra Algorithm)***
Calculate Objective Function for path between $W_{i,j}$ and M_i : Objective_fcn($W_{i,j}$, M_i);
Cluster_Objective_fcn= Cluster_Objective_fcn+ Objective_fcn($W_{i,j}$, M_i);
} END DO
Calculate Objective Function between M_i and Platform Base: Objective_fcn(M_i , Platform base);
Cluster_Objective_fcn= Cluster_Objective_fcn+ Objective_fcn(M_i , Platform base);
Total_Objective_fcn = Total_Objective_fcn +Cluster_Objective_fcn;
} END DO

e) Evaluate Constraints;

f) Iterate from a to f until local minimum found that satisfies the constraints;

Final Stage: *Generate Local optimal solution (manifolds positions, pipelines inner diameters, piping path)*

The proposed approach is a model-based methodology where the solution is based on several coupled multi-physics sub-models presenting a digital illustration of a physical system, a subsea production system. An overall flowchart of the model-based design process is presented in Figure 4-6. The proposed flowchart is illustrating the coupling between the different sub-models along with their integration as a model-based simulator within the optimization process to solve for the optimal subsea field architecture design with respect to the pre-discussed constraints.

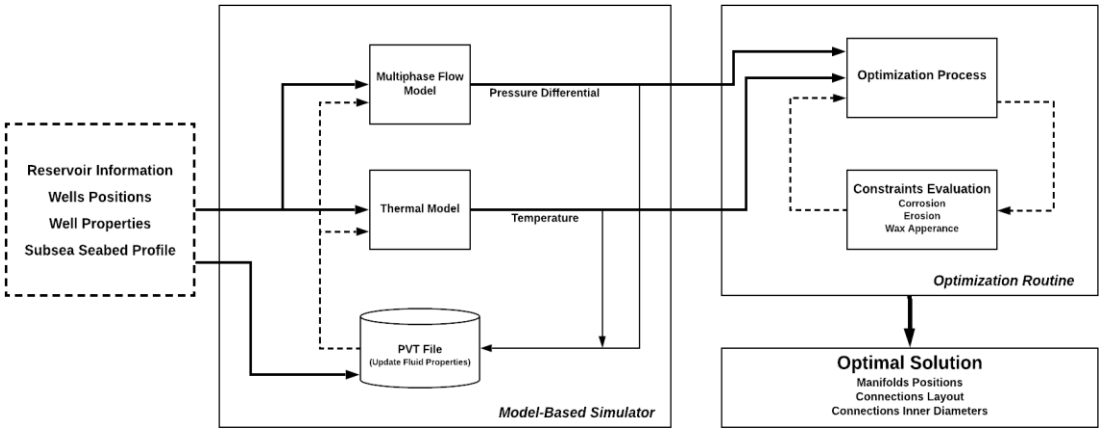

Figure 4-6: Model-Based Design Optimization Process

4.4 Model-Based Subsea Field Architecture Pre-FEED Design

4.4.1 Optimization Problem Inputs and Assumptions

A case study is provided herein for a subsea field containing 16 wells distributed throughout a seabed with the topology given in Figure 4-7.

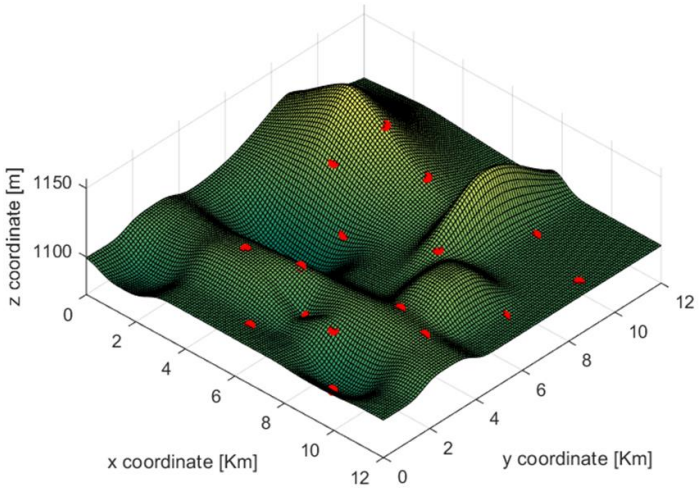

Figure 4-7: Seabed Topology and Subsea Wells Distribution

The information concerning the different wells is summarized in Table 4-2. Operating information include well pressure, well temperature, liquid volumetric flowrate Q_L and the gas volumetric flowrate Q_G as well as the positions of the different wells within the subsea field.

Table 4-2: Wells Operating Information and Positions

Well #	**Pressure (Pa)**	**Temperature (°C)**	Q_L **(m^3/s)**	Q_G **(m^3/s)**	x **(km)**	y **(km)**	z **(m)**
1	5965208	39.25	0.01	1.69	3.89	8.75	1141.41
2	6019608	37.06	0.01	1.63	3.21	7.25	1124.03
3	5669423	36.38	0.03	3.46	5.56	8.75	1120.30
4	6048015	33.26	0.03	3.49	4.5	6.32	1094.02
5	6043809	35.88	0.03	3.12	3.89	2.73	1114.94
6	5594064	35.37	0.03	3.37	5.56	3.33	1112.65
7	5952798	39.68	0.02	2.82	9.03	9.75	1101.83
8	5535527	38.79	0.03	3.41	8	6.67	1114.02
9	5890193	38.06	0.03	3	11.5	9	1100.30
10	5732166	37.24	0.02	1.78	11.09	6.25	1100.67
11	5905293	32.25	0.02	2.01	6.69	2.38	1097.77
12	5541319	32.78	0.03	3.17	5.83	0.83	1098.54
13	5899088	34.54	0.03	3.44	9.17	3.75	1113.42
14	5534838	35.51	0.02	2.23	8.05	2.08	1104.74
15	5938043	38.36	0.02	1.82	10.55	3.33	1112.04
16	5785945	35.56	0.02	2.8	9.17	0.83	1085.13

The presented information above is obtained by performing a simulation using PIPESIM Steady-State Multiphase Flow Simulator based on the reservoir properties presented in Table 4-3.

To simplify the overall system, many assumptions have been considered in this study. For starter, the subsea field architecture is defined to be constituted of subsea wells, cluster manifolds and a riser base. All the locations of the different subsea wells as well as the location of the riser base are fixed and fed as input to the overall system. In addition, all the connections are considered as rigid pipelines. The optimal pipelines connection is going to be determined as the results of the Dijkstra optimization problem

and each of the pipeline segments length is depending on the gridding process. In this case the subsea field is gridded into 100 meters' segments.

Table 4-3: Reservoir and Fluid Data

Parameter	Unit	Value
Downhole Pressure	psia	3200
Productivity Index of the reservoir	stb/d/psi	20
Reservoir Temperature	°F	120
Oil API	-	19
Seabed Temperature	°F	40
Saturation Pressure	psia	2800
Live oil viscosity at downhole P/T	cP	14
Solution GOR	scf/stb	340
Solution GLR	scf/stb	650
Dead Oil viscosity @ 104 °F	cP	130
Sulphur Content	%	0.75
Wax content	%	3
Wax appearance Temperature	°F	70
Pour point	°F	-20
Asphaltene content	%	2

4.4.2 Optimization Results

In this specific case, the wells grouping is set in prior: four well sets where in each one four wells are connected to one cluster manifold (Figure 4-8). An example of the optimization process is performed with a weighting factor α set equal to 0.5, meaning the same importance is assigned to both objective functions (pressure differential and cost). Initially, the locations of the manifolds are given as the geometric mean of the locations of the associated wells. Optimal locations of the manifolds will be determined during the optimization process.

Given this grouping option, the optimization process is evaluated to determine the optimal routing scheme as well as manifolds optimal locations for each well set and the size of the pipeline for each connection that minimizes the overall cost and pressure differential. This optimization example is performed provided additional pipeline and

insulation properties such as thickness and thermal conductivity introduced in Table 4-4.

Given this grouping option, the optimization process is evaluated to determine the optimal routing scheme as well as manifolds optimal locations for each well set and the size of the pipeline for each connection that minimizes the overall cost and pressure differential. This optimization example is performed provided additional pipeline and insulation properties such as thickness and thermal conductivity introduced in Table 3.

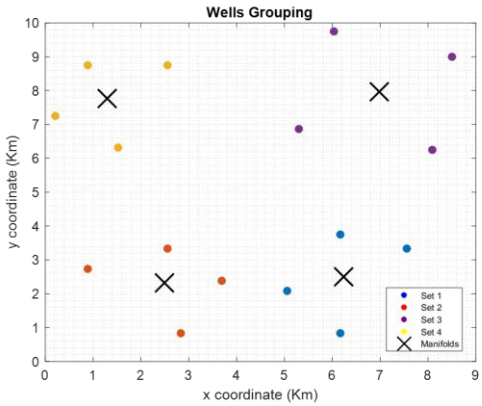

Figure 4-8: Subsea Wells Clustering Process Results

Table 4-4: Pipeline and Insulation Properties

Parameter	Unit	Value
Pipeline wall thickness	m	0.01
Pipeline wall thermal conductivity	$W.C^{-1}.m^{-1}$	50
Insulation Layer thickness	m	0.01
Insulation layer thermal conductivity	$W.C^{-1}.m^{-1}$	0.5

Based on the information listed in Table 4-2, Table 4-3 and Table 4-4, the identified optimal layout is shown in Figure 4-9.

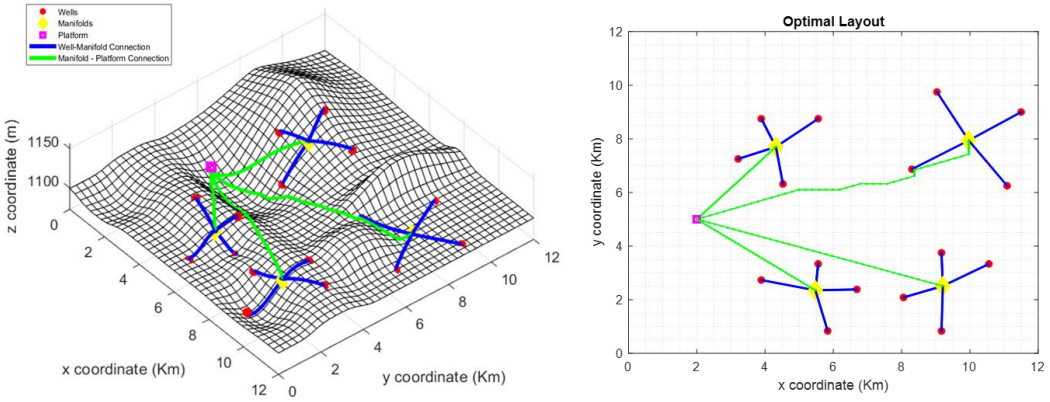

Figure 4-9: Subsea Optimal Layout ({4-4-4-4} Grouping, $\boldsymbol{\alpha}$ = 0.5)

The optimization process is a constrained problem. The presented constraints are mainly related to the pipeline structural integrity issues. Precisely, the optimization process is performed under the following conditions:

- A maximum mixture velocity is allowed: defined by setting a threshold for the erosional velocity within all connections.
- The corrosion rate along the connections must be less than a maximum allowance value (chosen as 3 mm/year).
- The temperature along the subsea field layout must stay above a wax appearance temperature (set as 10 °C).

The evaluated constraints at all the nodes of the subsea field layout are summarized. Presented in Figure 4-10 are the evaluated constraints (erosion and corrosion).

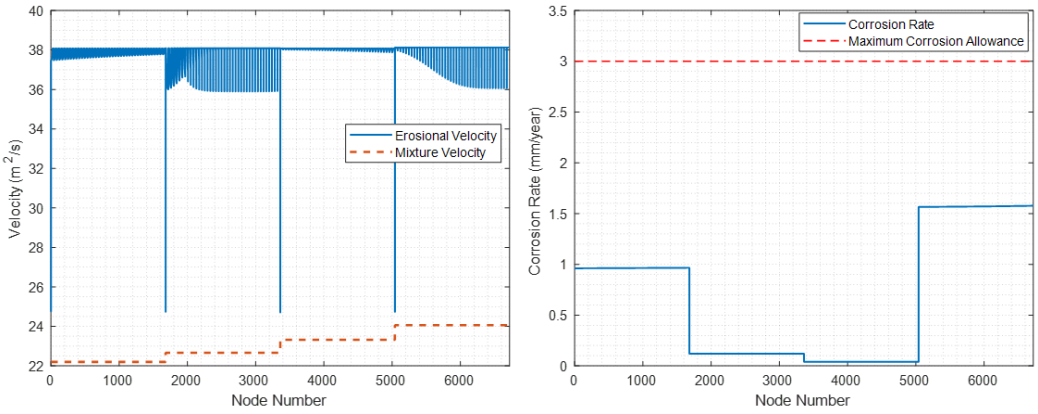

Figure 4-10: Erosion and Corrosion Constraints Evaluation

As shown, along all the connections, the erosion constraint is satisfied since the mixture velocity is always below the erosional velocity threshold. Hence, the aim of minimizing the possibility of having erosional issue is achieved. In the other hand, the optimal solution of the subsea field architecture presents an overall predicted corrosion rate that is below the maximum allowance threshold.

Knowing this information can also be useful to deploy a tracking system within each pipeline connection. This will allow the creation a corrosion and erosion profile along the connection which helps detect the corrosion hot spots along the pipelines as well as be used as a feedback information to control the inhibitors injection process.

4.4.3 Insulation Analysis

Another analysis scenario is performed using the proposed subsea field configuration. The effect of changing the type of pipeline insulation as well as the layer thickness is investigated. Using pipeline insulation is essential specially to reduce the risks of having solid precipitation and deposits within the flow lines. Applying the

thermal insulation on the outer surface of the pipelines ensures that the temperature of crude oil above the critical threshold wax appearance temperature (*WAT*). A sensitivity analysis is performed where several insulation configurations are compared and both the total volume as well as the cost of the insulation are determined by optimizing the overall subsea system for each case. The different type of insulation materials used during this analysis are shown in Table 4-5. In this table, the properties of each type are listed, the density of each material, the thermal conduction coefficient as well as the unit cost for each type [87].

Table 4-5: Insulation Layer Properties

Insulation material	**Density (kg/m^3)**	**Thermal Conductivity (W/(C.m))**	**Unit Price (USD/kg)**
Syntactic Polypropylene	890	0.16	2.8
Rubber	1300	0.28	1
Syntactic Epoxy	850	0.13	4.15
Polypropylene	900	0.22	1.7

Based on the provided properties, the optimization is performed for each type of insulation. For each case, three values for the insulation layer thickness are used: 0.01, 0.05 and 0.1 m. Both volume and cost of the insulation are determined after the optimization. The results are summarized in Figure 4-11 and Figure 4-12.

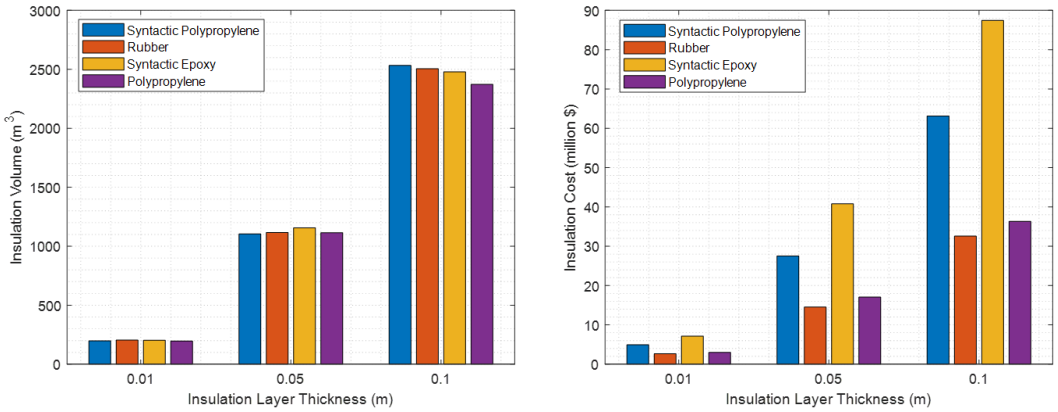

Figure 4-11: Insulation Analysis - Results (Volume and Cost)

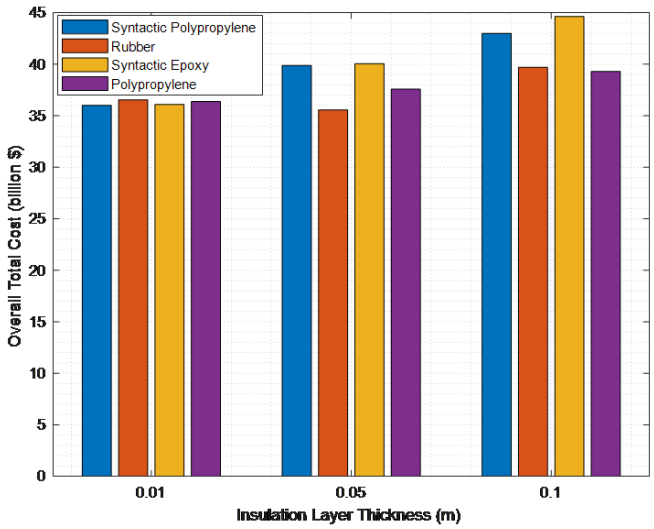

Figure 4-12: Overall Total Cost - Variation of Insulation Type and Thickness

As shown in Figure 4-11 and Figure 4-12, the impact of changing the insulation configuration on the overall cost of the insulation is assessed. Using this automated design methodology, an extensive study can be iteratively performed in which different scenarios and thermal insulation strategies are tested. Additional investigations can also be accomplished by including the search for an optimal insulation layer thickness based

on the material properties within the overall architecture optimization process. The corresponding results offer a family of optimized solutions that can be evaluated based on ease of maintenance, installation and overall cost while addressing flow assurance issue that can be present during the life stages of the subsea field.

4.4.4 Weighting Factor Variation Analysis

Since the study in this work is a multi-objective optimization problem, many solutions can be obtained. The resulting number of solutions is contingent upon the optimization objective function and its weighting factors. Based on the overall problem described in (4-21), the optimized objective functions evaluated with respect to the variation of the weighting factor α are presented in Figure 4-13.

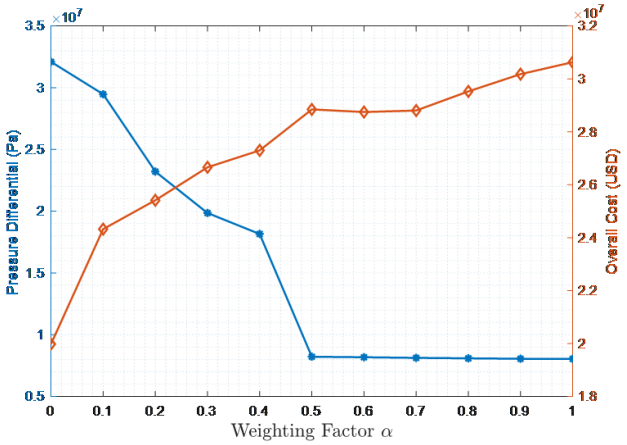

Figure 4-13: Weighting Factor Variation - Objective Functions Evaluation

The pressure differential function is decreasing for the range of weighting factor α up to 0.5. However, for α greater than 0.5, no major pressure differential variation is seen, while the overall cost continuous to increase as α increases. Hence, in this case a weighting factor that balances production flow and cost produced is $\alpha = 0.5$. However,

based on the user interests and the issues studied, different weighting factors can be used to give priority to one objective function over the other. This is helpful in the case where different financial scenarios are analyzed or that alternative measures are considered for dealing with the integrity and productivity issues within the field. In this case, the optimization methodology can be extended to incorporate these measures within the calculation process to give insights about their performance and efficiency.

4.4.5 Clustering Scenarios Analysis

The grouping of wells is either defined as an input by the user using standard types of cluster manifold (number of slots is equal to 4, 6, 8 or 10) or automatically determined by the proposed approach based on the result of the optimization presented in (4-18). The results of the optimization problem given different grouping scenarios are presented in Figure 4-14 to Figure 4-16.

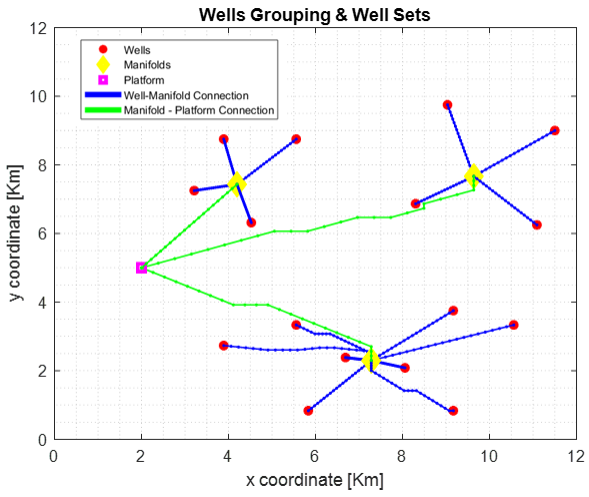

Figure 4-14: Optimal Subsea Layout - Case 1 {4-4-8}

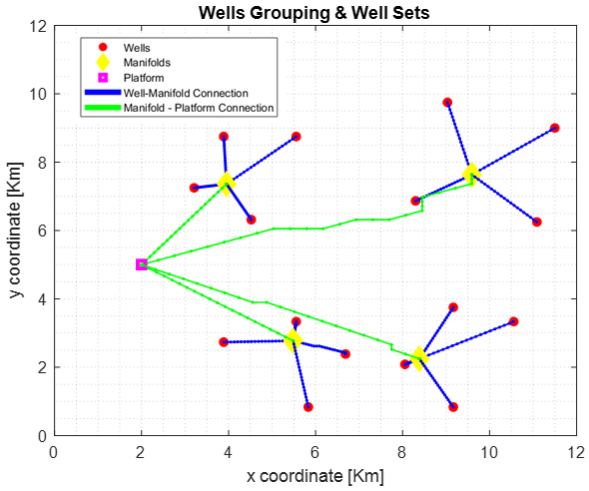

Figure 4-15: Optimal Subsea Layout - Case 2 {4-4-4-4}

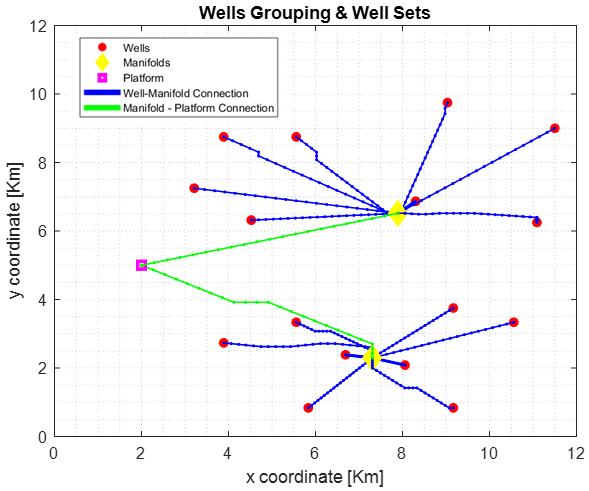

Figure 4-16: Optimal Subsea Layout - Case 3 {8-8}

As shown, three scenarios are evaluated: Case 1 {4-4-8} combination, Case 2 {4-4-4-4} combination and Case 3 with an {8-8} combination. The case with {8-8} grouping is the result of performing the integer optimization described in (4-18). Both other cases are user defined grouping configurations. In order to give an idea about the evaluated values of both objective functions (overall pressure differential and overall

cost) as well as the initial design chosen for each optimization scenario, the results of the optimization and the evaluated non-normalized objectives functions are presented. For each of the clustering scenarios presented above and considering the same importance for both functions ($\alpha = 0.5$), the results are summarized in Table 4-6.

Table 4-6: Grouping Analysis - Non-Normalized Objective Functions

{4-4-4-4} Case				{4-4-8} Case				{8-8} Case			
Attribute		Initial Design	Optimal Solution	Attribute		Initial Design	Optimal Solution	Attribute		Initial Design	Optimal Solution
Man #1	x	4.2944	4.3494	Man #1	x	7.3611	7.3304	Man #1	x	7.1375	7.2871
	y	7.7667	7.5995		y	1.9333	1.8663		y	7.8667	2.4405
	z	1125.2834	1122.0794		z	1104.1334	1103.4540		z	1118.2438	1104.6393
Man #2	x	9.9806	9.9460	Man #2	x	9.9806	9.9640	Man #2	x	7.3639	6.7688
	y	7.9667	7.8957		y	7.9667	7.9280		y	2.4104	7.3162
	z	1100.9774	1101.0265		z	1100.9774	1100.9998		z	1105.2019	1107.7621
Man #3	x	9.2361	9.1528	Man #3	x	5.8306	5.9307	Connections Inner Diameters (m)	1	0.381	0.4064
	y	2.5	2.5368		y	5.3271	5.3770		2	0.381	0.4064
	z	1108.34	1109.0605		z	1095.1514	1096.3910		3	0.381	0.4064
Man #4	x	5.4917	5.4257	Connections Inner Diameters (m)	1	0.381	0.4064		4	0.381	0.4064
	y	2.3208	2.3877		2	0.381	0.4064		5	0.381	0.4064
	z	1107.0813	1107.7728		3	0.381	0.4064		6	0.381	0.4064
Connections Inner Diameters (m)	1	0.381	0.4064		4	0.381	0.508		7	0.381	0.4064
	2	0.381	0.3048		5	0.381	0.256		8	0.381	0.508
	3	0.381	0.3048		6	0.381	0.4064		9	0.381	0.3048
	4	0.381	0.4064		7	0.381	0.4064		10	0.381	0.4064
	5	0.381	0.256		8	0.381	0.4064		11	0.381	0.4064
	6	0.381	0.4064		9	0.381	0.4064		12	0.381	0.4064
	7	0.381	0.4064		10	0.381	0.256		13	0.381	0.508
	8	0.381	0.4064		11	0.381	0.4064		14	0.381	0.4064
	9	0.381	0.4064		12	0.381	0.4064		15	0.381	0.4064
	10	0.381	0.256		13	0.381	0.4064		16	0.381	0.4064
	11	0.381	0.4064		14	0.381	0.508		17	0.381	0.4064
	12	0.381	0.4064		15	0.381	0.4064		18	0.381	0.3048
	13	0.381	0.4064		16	0.381	0.4064				
	14	0.381	0.508		17	0.381	0.4064				
	15	0.381	0.256		18	0.381	0.508				
	16	0.381	0.4064		19	0.381	0.256				
	17	0.381	0.4064								
	18	0.381	0.3048								
	19	0.381	0.508								
	20	0.381	0.256								
Pressure Differential (Pa)			1.568.E+7	Pressure Differential (Pa)			1.70E+07	Pressure Differential (Pa)			1.26E+07
Overall Cost (USD)			2.29E+07	Overall Cost (USD)			2.58E+07	Overall Cost (USD)			1.93E+07
Total Objective Function			1.93E+07	Total Objective Function			2.14E+07	Total Objective Function			1.59E+07

This kind of analysis identifies the possibility to evaluate different grouping scenarios. Hence, the feasibility is evaluated as well as the effectiveness of each scenario

based on the desired clustering protocols, and the types of available manifolds. This is beneficial especially if certain number of constraints are present which limit the options during the design process.

As shown in Table 4-6, having different grouping scenarios can largely affect the evaluation of both objective functions. For example, a grouping case of {8-8} presents less costs and pressure differential values compared to the others. This is illustrated mainly by the fact that the number of piping connections and cluster manifolds in this case is reduced. However, this comes at expense the fact that the larger the size of a cluster manifold, the harder its installation can be. In addition, several issues can occur, especially if this manifold is being used for gas injection into wells or is hosting a pigging device.

4.5 Conclusion

An integrated model-based method is developed using a digital subsea system representation for the design and the optimization of a subsea field architecture. The main objective is to present a reliable and engineering efficient methodology that can be used by experts during the design phase of subsea fields. This methodology is engineering efficient in terms of having an automated process that can offer a wide range of results and present an environment that can automatically simulate, test and analyze different types of design scenarios subject to diverse optimization objectives.

The integrated model-based methodology is developed by coupling different reduced-order, physics-based models. Precisely, several models are deployed, namely, a multiphase flow model coupled with a thermal model to capture the hydraulic and

thermal behavior of a steady state multiphase flow within pipelines network. Both hydraulic and thermal models are coupled via a properties adaptive block, assuring an estimation of the hydraulic and thermal properties of the fluid as a function of the operating conditions (temperature and pressure). Different constraints are introduced to cope with flow assurance challenges. The overall network is designed and optimized by considering erosion, corrosion, and wax appearance limitations. Being a system-based environment, the developed platform offers the possibility to include extra constraints depending on the studied problem as well as the user preferences.

Using the derived models and constraints, the optimization process is defined as a multi-objective optimization problem where both pressure differential and cost are desired to be as minimal. This is illustrated by the search for the optimal design fulfilling these requirements, meaning the optimal pipelines routing scheme, pipelines sizes as well as the manifolds placement. This is achieved via an integrated optimization process where the Dijkstra algorithm is coupled with a multi-start algorithm for global optimization.

Several sensitivity analyses are performed in this development. They include the effect of wells grouping in the case of a large subsea field as well as the effect of different weighting scenarios within the multi-objective optimization problem. This is introduced to illustrate the capabilities of the developed platform and to demonstrate its potential as a solution that can be extended to cover additional aspects that can be faced during the design, optimization and the development of a subsea field.

5 CONCLUSIONS AND FUTURE WORK

5.1 Conclusions

Proposed in this dissertation is a model-based optimization methodology for subsea field pre-FEED studies. The presented approach is introduced as a modular process where multi-physics sub-models have been developed and integrated to determine an optimal design of subsea field connecting scheme under production and flow assurance constraints. The main advantage of the presented methodology is the deployment of reduced-order and data-driven models allowing quasi-instantaneous results applicable for tasks where cheap computational efforts are required, such us systems design and optimization, real-time health monitoring and condition-based maintenance of subsea equipment.

As mentioned, pipelines are considered as the main element constituting a subsea system. Hence, understanding the dynamics of multiphase flow within pipelines with reduced computational time yet good accuracy is crucial within the subsea industry compartments. In chapter 2, a low-dimensional multiphase flow model in horizontal pipelines has been experimentally evaluated. The transient response of the low-D model for the case of air-water two-phase flow mixtures has been compared against experimental dataset, collected from the National University of Singapore Multiphase Flow Loop for different GVF levels and flow regimes that can be encountered in the oil and gas production.

The studied reduced-order two-phase flow model is developed following three major steps. A mechanistic steady-state multiphase flow model is used as a first step to determine the fluid steady-state flowing conditions such as flow pattern, liquid holdup

and pressure drop. Then, these estimations are used to approximate equivalent fluid properties to present the two-phase flow as one single-phase equivalent fluid. These equivalent properties are fed to a modal approximation of the dissipative distributed-parameter model.

To give more insights about the performance of the low-D multiphase flow analytical model, a comparison with results from OLGA Dynamic Multiphase Flow Simulator, a widely used simulation package in the industry, has been introduced. The Low-D model pressure predictions and the OLGA simulations were compared to the measured transient pressure for different GVF levels. As detailed in chapter 2, both models have showed good prediction agreement with the experimental data with less than 5% mean absolute percent error. However, an accuracy-simulation time tradeoff is suggested depending on the required accuracy and available computational power. Precisely, the effect of the number of modes on the low-D model has been analyzed. As shown in chapter 2, increasing the model order (number of modes) results in an improved accuracy however will require a longer computation time.

In the other hand, the analysis of the single-phase flow experimental dataset established the existence of entrained or entrapped air in the system due to the action of the water pump. It has been shown that the presence of entrained air in the pipeline results in a significantly lower speed of sound of the fluid leading to a considerable increase in the pipeline damping and a decrease in the natural frequency.

In chapter 3, one of the main issues in the oil and gas industry has been studied. Precisely, a new “Parameter Varying” (PV) carbon dioxide corrosion rate model in oil and gas pipeline has been developed. To develop this model, a comparison of some of

the existing CO_2 corrosion prediction models highlighting the differences between their structures as well as the required inputs required has been conducted allowing a good benchmarking to assess the most appropriate model to be used as a foundation in developing the newly data-driven model for CO_2 corrosion prediction.

The proposed CO_2 corrosion rate model is based on newly introduced parameter varying coefficients where the fluid factors influencing corrosion rates are nonlinear correlation between the pH and the flow velocity. These introduced coefficients were not derived from physics, instead the results of a data driven approach based on a system identification methodology. A key aspect is its modularity that lends itself to isolated corrections derived from additional experimental and scientific studies. The proposed parameter varying CO_2 corrosion rate model is based on (3-8) developed in [52]. The parameter varying coefficients were identified by determining the functional relationship between flow parameters of velocity and pH to the residual generated between experimental data and (3-8). Significant improvements in CO_2 corrosion rate modelling were achieved. The resulting model produced an R-Squared value of 0.9 in comparison to 0.54 associated with (3-8). The maximum residual of the proposed model is 12 mm/year based on the validation dataset whereas the model in (3-8) is 24 mm/year.

In chapter 4, An integrated model-based method has been developed using a digital subsea system representation for the design and the optimization of a subsea field architecture. The main objective is to present a reliable and engineering efficient methodology that can be used by experts during the design phase of subsea fields. This methodology is engineering efficient in terms of having an automated process that can offer a wide range of results and present an environment that can automatically simulate,

test, and analyze different types of design scenarios subject to diverse optimization objectives.

The integrated model-based methodology is developed by incorporating the multiphase flow modeling approach presented in chapter 2 and the newly developed data-driven CO_2 corrosion rate model developed in chapter 3 as well as several other reduced-order, physics-based models describing different aspects of a subsea production system. Precisely, the multiphase flow model described in chapter 2 has been coupled with a thermal model to capture the hydraulic and thermal behavior of a steady state multiphase flow within pipelines network. To highlight the interdependence of both hydraulic and thermal behavior of a mixture flowing within a pipeline and their effect on the fluid properties, both these models have been coupled via a properties adaptive block, assuring an estimation of the hydraulic and thermal properties of the fluid as a function of the operating conditions (temperature and pressure). In addition to carbon dioxide corrosion, different constraints are introduced to cope with flow assurance challenges. The overall subsea field network is designed and optimized by considering erosion, corrosion, and wax appearance limitations as well as seabed topology and elevation variations.

Integrating the derived models and constraints, the optimization process is defined as a multi-objective optimization problem where both pressure differential and cost are desired to be as minimal. The main objective is then defined by finding the optimal design fulfilling all the listed requirements, meaning the optimal pipelines routing scheme, pipelines sizes as well as the manifolds placement. This is achieved by

incorporating the Dijkstra algorithm within a multi-start algorithm routine for global optimization.

To illustrate the capabilities of the proposed methodology, several sensitivity analyses are performed, including wells grouping scenarios in the case of a large subsea field and their effect on the overall optimization results as well as the effect of different weighting scenarios within the multi-objective optimization problem. In addition, the effect of varying the pipeline insulation properties for different configuration has been investigated to demonstrate the potential to use the proposed approach as a fast testing platform for thermal and insulation analysis.

Overall, the proposed model-based optimization approach can be deployed as a fast testing environment offering the ability for the subsea engineer during the pre-FEED study phase to test, analyze and investigate a variety of connecting scenarios or having a fast optimal layout scheme guess that can be the basis for more elaborated and well detailed studies. In addition, with the modularity characteristic that it offers, this approach is giving the user a lot of flexibility to integrate different models as seen appropriate depending on the task requirements and necessities.

5.2 Future Work

Considering the modularity of the presented optimization approach, different sub-models can be added or changed depending of the user preferences. In other terms, extensive studies can be performed to incorporate additional modules describing other aspects and phenomena that can interfere with the subsea field layout determination. Precisely, the presented methodology is based on the integration of reduced-order

physics-based models, this characteristics enable the amelioration of the overall system accuracy and computation time based on the evaluation and the recalibration of the existing sub-models based on experimental investigation as well as in field collected data. Such capacity offers the users the ability to broaden the range of the applicability of the presented approach to cover almost every aspect or issue that can occur during the overall life cycle of the subsea production system.

As a feasible future step, more investigation can be performed to ameliorate the presented CO_2 corrosion rate prediction model aiming at evaluating the effect of the fluid properties, pressure, and temperature variations on the model's accuracy under a wide range of operating conditions. This will be ensured by including more complex phenomena encountered in practical applications, such as the effect of the pipe steel composition and texture, effect of inhibitors, and modelling of localized attacks namely pitting corrosion. Since the development of such an adaptive model has been constructed using data analytics, such amelioration will enable the descriptive, predictive, diagnostic, and prescriptive analytics (digital twin) that provides value-add to the oil and gas industry.

Such study can also be extended to enhance the accuracy of the proposed multiphase flow model presented in chapter 2. Precisely, the collection of additional that covers more flow patterns and fluid properties as well as the variation of the geometry configuration can be helpful to highlight other issue existing in a subsea production system and can be interfering in the next steps of the development of a subsea field such us slugging. Hence, the addition of a slug-tracking module is also suggested for the Low-D model to simulate the hydrodynamic slugging conditions and

exploit such information during the design phase to ameliorate the output result of the optimization process.

In the other hand, by taking into account the level of accuracy and the advantage of computational requirements regarding the OLGA dynamic multiphase flow simulator, the application of the multiphase flow model presented in chapter 2 can be extended to perform extra real-time tasks varying from production monitoring, pressure and flow rate forecasting along pipelines, instantaneous flow pattern tracking as well as coupling with flow assurance models for pipelines integrity management analysis.

However, the main extension that can be incorporated within this work as a future amelioration is having a platform that enables the simulation of the whole subsea system from the reservoir to the terminals, which represents a big asset for the oil and gas industry. In this matter, the proposed methodology can provide the needed information. In addition, more elaborated analysis can be provided to cover more aspects related to the subsea system simulations namely the sea state uncertainties such as environment temperature, overburden pressure, and delivery flow. However, this can be enhanced by including a drilling simulation and optimization module. This will be the complementary of the present work, allowing to cover all the subsea system departments (upstream, midstream, and downstream).

REFERENCES

[1] BP, "Statistical Review of World Energy 2020," Retrieved 17 February 2021.

[2] C. CORPORATION, "Ofshore Oil and Gas Development," 2017.

[3] Y. Redutskiy, "Integration of oilfield planning problems: infrastructure design, development planning and production scheduling," *Journal of Petroleum Science and Engineering,* vol. 158, pp. 585-602, 2017.

[4] R. Iyer, I. Grossmann, S. Vasantharajan, and A. Cullick, "Optimal planning and scheduling of offshore oil field infrastructure investment and operations," *Industrial & Engineering Chemistry Research,* vol. 37, pp. 1380-1397, 1998.

[5] M. Carvalho and J. Pinto, "An MILP model and solution technique for the planning of infrastructure in offshore oilfields," *Journal of Petroleum Science and Engineering,* vol. 51, pp. 97-110, 2006.

[6] V. Gupta and I. E. Grossmann, "An efficient multiperiod MINLP model for optimal planning of offshore oil and gas field infrastructure," *Industrial & Engineering Chemistry Research,* vol. 51, pp. 6823-6840, 2012.

[7] O. F. M. El-Mahdy, M. E. H. Ahmed, and S. Metwalli, "Computer aided optimization of natural gas pipe networks using genetic algorithm," *Applied Soft Computing,* vol. 10, pp. 1141-1150, 2010.

[8] S. Sanaye and J. Mahmoudimehr, "Optimal design of a natural gas transmission network layout," *Chemical Engineering Research and Design,* vol. 91, pp. 2465-2476, 2013.

[9] H. Zhang, Y. Liang, J. Ma, C. Qian, and X. Yan, "An MILP method for optimal offshore oilfield gathering system," *Ocean Engineering*, vol. 141, pp. 25-34, 2017.

[10] A. Kabirian and M. R. Hemmati, "A strategic planning model for natural gas transmission networks," *Energy policy*, vol. 35, pp. 5656-5670, 2007.

[11] H. Üster and Ş. Dilaveroğlu, "Optimization for design and operation of natural gas transmission networks," *Applied Energy*, vol. 133, pp. 56-69, 2014.

[12] M. Mikolajková, C. Haikarainen, H. Saxén, and F. Pettersson, "Optimization of a natural gas distribution network with potential future extensions," *Energy*, vol. 125, pp. 848-859, 2017.

[13] H. Rodrigues, B. Prata, and T. Bonates, "Integrated optimization model for location and sizing of offshore platforms and location of oil wells," *Journal of Petroleum Science and Engineering*, vol. 145, pp. 734-741, 2016.

[14] Y. Wang, M. Duan, M. Xu, D. Wang, and W. Feng, "A mathematical model for subsea wells partition in the layout of cluster manifolds," *Applied Ocean Research*, vol. 36, pp. 26-35, 2012.

[15] Y. Wang, M. Duan, J. Feng, D. Mao, M. Xu, and S. F. Estefen, "Modeling for the optimization of layout scenarios of cluster manifolds with pipeline end manifolds," *Applied Ocean Research*, vol. 46, pp. 94-103, 2014.

[16] C. Hong, Y. Wang, J. Yang, Y. M. Berbert, M. I. Lourenço, and S. F. Estefen, "Subsea production layout: design and cost," in *ASME 2017 36th International Conference on Ocean, Offshore and Arctic Engineering*, 2017.

[17] V. R. Rosa, E. Camponogara, and V. J. M. Ferreira Filho, "Design optimization of oilfield subsea infrastructures with manifold placement and pipeline layout," *Computers & Chemical Engineering*, vol. 108, pp. 163-178, 2018.

[18] H. Meisingset, J. Hove, and G. Olsen, "Optimization of pipeline routes," in *The Fourteenth International Offshore and Polar Engineering Conference*, 2004.

[19] I. N. Vieira, C. H. Albrecht, B. S. L. P. de Lima, B. P. Jacob, D. M. Rocha, and C. de Oliveira Cardoso, "Towards a computational tool for the synthesis and optimization of submarine pipeline routes," in *The Twentieth International Offshore and Polar Engineering Conference*, 2010.

[20] J. S. Baioco, C. H. Albrech, B. P. Jacob, and D. M. Rocha, "Multi-Objective Optimization of Submarine Pipeline Routes Considering On-Bottom Stability, VIV-Induced Fatigueand Multiphase Flow," in *The Twenty-fifth International Ocean and Polar Engineering Conference*, 2015.

[21] D. M. Rocha, C. d. O. Cardoso, R. G. Borges, J. S. Baioco, C. H. Albrecht, and B. P. Jacob, "Optimization of submarine pipeline routes considering slope stability," in *Offshore Technology Conference*, 2015.

[22] A. Meziou, M. Chaari, M. Franchek, R. Borji, K. Grigoriadis, and R. Tafreshi, "Low-dimensional modeling of transient two-phase flow in pipelines," *Journal of Dynamic Systems, Measurement, and Control*, vol. 138, p. 101008, 2016.

[23] D. H. Beggs and J. P. Brill, "A study of two-phase flow in inclined pipes," *Journal of Petroleum technology*, vol. 25, pp. 607-617, 1973.

[24] N. Petalas and K. Aziz, "A mechanistic model for multiphase flow in pipes," *Journal of Canadian Petroleum Technology*, vol. 39, 2000.

[25] N. Petalas, and Aziz, K., "Stanford Multiphase Flow Database - User's Manual, Version 0.2," *Petroleum Engineering Department, Stanford University.*

[26] K. H. Bendiksen, D. Maines, R. Moe, and S. Nuland, "The dynamic two-fluid model OLGA: Theory and application," *SPE production engineering*, vol. 6, pp. 171-180, 1991.

[27] A. R. Hagedorn and K. E. Brown, "Experimental study of pressure gradients occurring during continuous two-phase flow in small-diameter vertical conduits," *Journal of Petroleum Technology*, vol. 17, pp. 475-484, 1965.

[28] Y. Taitel and A. E. Dukler, "A model for predicting flow regime transitions in horizontal and near horizontal gas-liquid flow," *AIChE journal*, vol. 22, pp. 47-55, 1976.

[29] D. Barnea, "A unified model for predicting flow-pattern transitions for the whole range of pipe inclinations," *International Journal of Multiphase Flow*, vol. 13, pp. 1-12, 1987.

[30] J. Xiao, O. Shonham, and J. Brill, "A comprehensive mechanistic model for two-phase flow in pipelines," in *SPE Annual Technical Conference and Exhibition*, 1990.

[31] A. Ansari, N. Sylvester, O. Shoham, and J. Brill, "A comprehensive mechanistic model for upward two-phase flow in wellbores," in *SPE annual technical conference and exhibition*, 1990.

[32] K. Moore and W. Rettig, "RELAP4: A computer program for transient thermal-hydraulic analysis," Aerojet Nuclear Co., Idaho Falls, Idaho (USA)1973.

[33] A. Fisher, D. Reid, M. Z. Tan, and G. Galloway, "Extending the Boundries of Casing Drilling," in *IADC/SPE Asia Pacific Drilling Technology Conference and Exhibition*, 2004.

[34] T. J. Danielson, K. M. Bansal, R. Hansen, and E. Leporcher, "LEDA: the next multiphase flow performance simulator," in *12th International Conference on Multiphase Production Technology*, 2005.

[35] K. Bendiksen, I. Brandt, P. Fuchs, H. Linga, D. Malnes, and R. Moe, "Two-phase flow research at SINTEF and IFE: some experimental results and a demonstration of the dynamic two-phase flow simulator OLGA," in *Offshore Northern Seas Conference, Stavanger*, 1986.

[36] www.swri.org, "SwRI."

[37] www.utulsa.edu, "University of Tulsa."

[38] www.cranfield.ac.uk, "Multiphase flow facility at Cranfield University,."

[39] M. King, C. Hale, C. Lawrence, and G. Hewitt, "Characteristics of flowrate transients in slug flow," *International journal of multiphase flow*, vol. 24, pp. 825-854, 1998.

[40] R. P. Sutton, R. L. Christiansen, T. K. Skinner, and B. L. Wilson, "Investigation of Gas Carryover With a Downward Liquid Flow," in *SPE Annual Technical Conference and Exhibition*, 2006.

[41] https://www.researchgate.net/lab/Wai-Lam-Loh-Lab-Multiphase-Flow-Loop-Wai-Lam-Loh, "NUS Multiphase Flow Loop."

[42] F. T. Brown, "The transient response of fluid lines," 1962.

[43] M. E. Franke, A. J. Malanowski, and P. Martin, "Effects of temperature, end-conditions, flow, and branching on the frequency response of pneumatic lines," 1972.

[44] D. N. Johnston, "Numerical modelling of unsteady turbulent flow in tubes, including the effects of roughness and large changes in Reynolds number," *Proceedings of the Institution of Mechanical Engineers, Part C: Journal of Mechanical Engineering Science,* vol. 225, pp. 1874-1885, 2011.

[45] R. Oldenburger and R. Goodson, "Simplification of hydraulic line dynamics by use of infinite products," 1964.

[46] C.-Y. Hsue and D. A. Hullender, "Modal approximations for the fluid dynamics of hydraulic and pneumatic transmission lines," in *IN: Fluid transmission line dynamics 1983; Proceedings of the Winter Annual Meeting, Boston, MA, November 13-18, 1983 (A84-22296 08-34). New York, American Society of Mechanical Engineers, 1983, p. 51-77. Research sponsored by the University of Texas.*, 1983, pp. 51-77.

[47] W. L. Loh, V. Hernandez-Perez, N. D. Tam, T. T. Wan, Z. Yuqiao, and V. K. Premanadhan, "Experimental study of the effect of pressure and gas density on the transition from stratified to slug flow in a horizontal pipe," *International Journal of Multiphase Flow,* vol. 85, pp. 196-208, 2016.

[48] E. Wylie, "Streeter, Fluid Transients," ed: McGraw-Hill, 1978.

[49] J. A. Fox, *Hydraulic Analysis of Unsteady Flow in Pipe*: Macmillan International Higher Education, 1977.

[50] C. Sarica, H.-Q. Zhang, and R. J. Wilkens, "Sensitivity of slug flow mechanistic models on slug length," *Journal of energy resources technology,* vol. 133, 2011.

[51] ASME, "B31.8S : Managing System Integrity of Gas Pipelines," ed: American Society of Mechanical Engineers 2016.

[52] C. DeWaard, U. Lotz, and A. Dugstad, "Influence of Liquid Flow Velocity on CO_2 Corrosion: A Semi-Empirical Model," in *CORROSION-NATIONAL ASSOCIATION OF CORROSION ENGINEERS ANNUAL CONFERENCE-*, 1995.

[53] S. Nešić, "Key issues related to modelling of internal corrosion of oil and gas pipelines–A review," *Corrosion science,* vol. 49, pp. 4308-4338, 2007.

[54] L. G. Gray, B. G. Anderson, M. J. Danysh, and P. R. Tremaine, "Effect of pH and temperature on the mechanism of carbon steel corrosion by aqueous carbon dioxide," *Corrosion/90, paper,* vol. 40, 1990.

[55] C. De Waard, U. Lotz, and D. Milliams, "Predictive model for CO_2 corrosion engineering in wet natural gas pipelines," *Corrosion,* vol. 47, pp. 976-985, 1991.

[56] M. Nordsveen, S. Nešic, R. Nyborg, and A. Stangeland, "A mechanistic model for carbon dioxide corrosion of mild steel in the presence of protective iron carbonate films—part 1: theory and verification," *Corrosion,* vol. 59, pp. 443-456, 2003.

[57] S. Nesic, J. Postlethwaite, and S. Olsen, "An electrochemical model for prediction of corrosion of mild steel in aqueous carbon dioxide solutions," *Corrosion,* vol. 52, pp. 280-294, 1996.

[58] S. Turgoose, R. Cottis, and K. Lawson, "Modeling of electrode processes and surface chemistry in carbon dioxide containing solutions," in *Computer Modeling in Corrosion*, ed: ASTM International, 1992.

[59] B. Pots, "Mechanistic models for the prediction of CO_2 corrosion rates under multi-phase flow conditions," NACE International, Houston, TX (United States)1995.

[60] D. Davies and G. Burstein, "The effects of bicarbonate on the corrosion and passivation of iron," *Corrosion*, vol. 36, pp. 416-422, 1980.

[61] S. Nesic, M. Nordsveen, and A. Stangel, "A Mechanistic Model for C02 Corrosion with Protective Iron Carbonate Films," 2001.

[62] N. Standard, "CO2 Corrosion rate calculation model," *Majorstural, Norway: Norwegian Technological Standards Institute Oscarsgt*, vol. 20, 2005.

[63] C. De Waard and D. Milliams, "Carbonic acid corrosion of steel," *Corrosion*, vol. 31, pp. 177-181, 1975.

[64] J. O. M. Bockris and D. Koch, "Comparative rates of the electrolytic evolution of hydrogen and deuterium on iron, tungsten and platinum," *The Journal of Physical Chemistry*, vol. 65, pp. 1941-1948, 1961.

[65] C. DeWaard and D. Williams, "Prediction of carbonic acid corrosion in natural gas pipelines," *Ind. Finish. Surf. Coatings*, vol. 28, pp. 24-26, 1976.

[66] A. Dugstad, L. Lunde, and K. Videm, "Parametric study of CO_2 corrosion of carbon steel," NACE International, Houston, TX (United States)1994.

[67] Y. Zhang, K. Gao, G. Schmitt, and R. Hausler, "Modeling steel corrosion under supercritical CO_2 conditions," *Materials and Corrosion,* vol. 64, pp. 478-485, 2013.

[68] S. Papavinasam, R. W. Revie, W. I. Friesen, A. Doiron, and T. Panneerselvan, "Review of models to predict internal pitting corrosion of oil and gas pipelines," *Corrosion Reviews,* vol. 24, pp. 173-230, 2006.

[69] NACE, "NACE Technical Committee Report 21413-SG: "Prediction of Internal Corrosion in Oilfield Systems from System Conditions"," Technical Committee Report2017.

[70] H. D. Beggs, "Production optimization using nodal analysis," 1991.

[71] A. Meziou, Z. Khan, T. Wassar, M. A. Franchek, R. Tafreshi, and K. Grigoriadis, "Dynamic Modeling of Two-Phase Gas/Liquid Flow in Pipelines," *SPE Journal,* 2019.

[72] A. P. Institute., "API RP 14E. Recommended practice for design and installation of offshore production platform piping systems," 1991.

[73] H. Mnasri, T. Wassar, M. A. Franchek, and E. E. Marotta, "Data-Driven Modeling of Carbon Dioxide Corrosion for Integrity Management Application," *SPE Production & Operations,* 2019.

[74] ASME, "Power Piping B31.1," *ASME,* p. 380, 2018 2018.

[75] Z. Huang, H. S. Lee, M. Senra, and H. Scott Fogler, "A fundamental model of wax deposition in subsea oil pipelines," *AIChE Journal,* vol. 57, pp. 2955-2964, 2011.

[76] P. T. Mason and J. L. Upchurch, "Seastar: subsea cluster manifold system design and installation," in *Offshore Technology Conference*, 1996.

[77] S. Homer, J. Chitwood, T. Childers, and A. Verrett, "Deepwater Templates and Cluster Well Manifolds: Is There a Single Correct Approach?," in *Offshore Technology Conference*, 1993.

[78] http://www.subseapedia.org/w/index.php?title=File:Cluster_Manifold.png, "Subsea Cluster Manifold."

[79] N. Ganganath, C.-T. Cheng, and K. T. Chi, "Data clustering with cluster size constraints using a modified k-means algorithm," in *2014 International Conference on Cyber-Enabled Distributed Computing and Knowledge Discovery*, 2014, pp. 158-161.

[80] J. Xiao, A. Al-Muraikhi, and A. M. Qahtani, "Automated route finding for production flowlines to minimize liquid inventory and pressure loss," in *SPE Annual Technical Conference and Exhibition*, 2006.

[81] J. Zhou, G. Liang, T. Deng, and J. Gong, "Route optimization of pipeline in gas-liquid two-phase flow based on genetic algorithm," *International Journal of Chemical Engineering*, vol. 2017, 2017.

[82] O. Grodzevich and O. Romanko, "Normalization and other topics in multi-objective optimization," 2006.

[83] Y. Bai and Q. Bai, *Subsea engineering handbook*: Gulf Professional Publishing, 2018.

[84] E. W. Dijkstra, "A note on two problems in connexion with graphs," *Numerische mathematik*, vol. 1, pp. 269-271, 1959.

[85] E. Pyrga, F. Schulz, D. Wagner, and C. Zaroliagis, "Efficient models for timetable information in public transportation systems," *Journal of Experimental Algorithmics (JEA)*, vol. 12, pp. 1-39, 2008.

[86] Z. Ugray, L. Lasdon, J. Plummer, F. Glover, J. Kelly, and R. Martí, "Scatter search and local NLP solvers: A multistart framework for global optimization," *INFORMS Journal on Computing*, vol. 19, pp. 328-340, 2007.

[87] J. Yang, M. I. Lourenço, and S. F. Estefen, "Thermal insulation of subsea pipelines for different materials," *International Journal of Pressure Vessels and Piping*, vol. 168, pp. 100-109, 2018.